Spring 5-15-2019

Electronic Transport Behavior of Adatom- and Nanoparticle-Decorated Graphene

Jamie Anne Elias
Washington University in St. Louis

WASHINGTON UNIVERSITY IN ST.LOUIS

Department of Physics

Dissertation Examination Committee:
Erik Henriksen, Chair
Sophia Hayes
Kenneth Kelton
Zohar Nussinov
Li Yang

Electronic Transport Behavior of Adatom- and Nanoparticle-Decorated Graphene

by

Jamie Anne Elias

A dissertation presented to
The Graduate School
of Washington University in
partial fulfillment of the
requirements for the degree
of Doctor of Philosophy

May 2019
St. Louis, Missouri

Contents

List of Figures

List of Tables

Acknowledgements

In one way or another, many people are involved in the attainment of a PhD. First and foremost, credit must go to the One who gave me the ability and the opportunity. I have more than this to be eternally grateful for.

At Washington University, I must give credit to several people for helping me grow professionally. In particular and especially, my thesis advisor Dr. Erik Henriksen, who took a chance on this student and patiently developed her into a reasonable physicist. I could only hope to replicate his enthusiasm, creativity, and unwavering support in my own life and career. Others who've had a hand in my education include but are not limited to: Dr. Ken Kelton, Dr. Zohar Nussinov, Dr. Mairin Hynes, and Dr. Mark Conradi.

The faculty, staff, and students of the Institute of Materials Science and Engineering for collaborating and discussing new ideas. The Physics Department machine shop staff have never failed to guide me through projects. In particular, my retired friend, Tony Biondo always helped with whatever design I was working on. But, even more, he kept me well-rounded with our lunchtime discussions of literature, food, and history. Alison Verbeck, who gave me a safe place to go and a friend to talk to when I needed someone with whom to think, question, or commiserate. Beth Gartin, who kept my head out of the clouds and Merita Haxia who supported my role as a teaching assistant.

I also thank my peers whom I spent daily time: Boyi Zhou, Jordan Russell, Nero Zhou, Yashika Kapoor, and Jesse Balgley. These are the people who teamed up with me to tackle

the everyday nuisances of experimental work. Then there are the undergraduates who contributed to my project: Joshua Cohen, Jordan Pack, Patrick Chao, Zack Weinstein, Devon Berwick, and Hector Morales-Rosado. Another peer to whom I owe gratitude: Janie Hoorman for timely Christian fellowship and help surviving some of those graduate courses.

Finally, outside of Washington University, I extend my thanks to several others. I must thank my husband, who followed me here with love and support despite the hold it has put on his own career. My Dad, who's encouragement to study and excel in science followed me through this undertaking. My Mom, my best friend who moved halfway across the country to be nearby. My siblings, Susan Daust and Josh Pelno; our bond is stronger than blood. My toughest and sweetest prayer warrior, Nana; you're beautiful on the inside and outside. To my Aunt Jody and Uncle Rob Schroeder (and cousins Bethany, Nathaniel, and Harmony); even as a child, I looked up to you as my role models. Brandi Stocum, my best buddy at home who knows me better than most and loves me anyway.

Last, but not least: I'd like to thank my mentors: Dr. Ken Podolak, Dr. Glenn Myer, Dr. Michael Walters, Dr. James Armstrong, Dr. Margaret Morrow, Dr. Ann Tracy, and Professor Bodenrader at SUNY Plattsburgh for giving me the foundation and confidence to pursue physics. Others include: my Aunt Judi who has encouraged me by paving her own path of success in authorship, my in-laws who treat me like one of their own, Ben and Carrie LeVasseur as well as Ann and Chris Laska for friendship and support during troubling times, and our friends at Turnpike Wesleyan.

Altogether, you are a varied and extraordinary group of people. None of this would have been possible had you not been a part of my life.

Jamie Anne Elias

Washington University in St. Louis

May 2019

ABSTRACT OF THE DISSERTATION

Electronic Transport Behavior of Adatom- and Nanoparticle-Decorated Graphene

by

Jamie Anne Elias

Doctor of Philosophy in Physics

Washington University in St. Louis, 2019

Professor Erik Henriksen, Chair

To induce a non-negligible spin-orbit coupling in monolayer graphene, for the purposes of realizing the Kane-Mele Hamiltonian, transition metal adatoms have been deposited in dilute amounts by thermal evaporation in situ while holding the device temperature near 4K. Electronic transport studies including measurements such as gate voltage dependent conductivity and mobility, weak localization, high field magnetoresistance (Shubnikov de Haas oscillations), quantum Hall, and nonlocal voltage were performed at low temperature before and after sequential evaporations. Studies of tungsten adatoms are consistent with literature regarding other metal adatoms on graphene but were unsuccessful in producing a spin-orbit signature, at least partially due to lithography residue inhibiting the adatoms' ability to dope the graphene. Osmium adatoms on graphene behave differently from other adatoms in several ways. While all other measured adatoms donate electrons to graphene, osmium is observed to donate holes to graphene. In addition, tungsten and other adatoms directly affect the scattering potentials by causing a dominant Coulomb-like potential from isolated point charges. Osmium, on the other hand, does not obey this simple model. Separately, a claim was made in a recent study of Bi_2Te_3 nanoparticles on graphene showing tantalizing evidence of quantization in resistance coinciding with predictions for edge channel conduction. Our attempts to reproduce these observations have not been successful so far.

Chapter 1

Introduction

1.1 Brief overview of graphene

Much discussion in the mid 1900s [1] about monolayer graphene, a single-atomic layer of hexagonally arranged carbon atoms, predicated its experimental realization in 2004 [2]. This realization was largely thought to be impossible due to predictions that 2D materials would be thermodynamically unstable as a consequence of the Mermin-Wagner theorem [3, 4]. However, because graphene is unique electronically, thermodynamically, and mechanically, it has become of interest to a wide variety of fields: physics, chemistry, engineering to name a few, for an equivalently wide variety of applications: probing topological materials, nanosensors, energy storage etc. Indeed, since 2004, the yearly number of publications involving graphene have increased with striking rapidity; there were around 150 graphene publications for 2004 versus over 15,500 graphene articles published in 2014. By 2014, the total accumulation of research articles about graphene had reached nearly 50,000 articles [5].

A large subset of these publications are concerned with the highly unique electronic properties, in particular the band structure, of graphene. In contrast to modern semiconductors, the low energy dispersion relation of graphene is linear in momentum rather than

parabolic. This linearity is analogous to a system of relativistic, massless Dirac fermions. In addition, unlike other semiconductors, the band structure of graphene features a meeting of the valence and conduction bands at the degenerate Dirac point, which defines graphene as a semi-metal rather than a semiconductor. Other exciting electronic properties of graphene include: the observation is that of a photoconductivity transition between the Dirac point and high carrier density [6], the high carrier mobility, and the presence of finite minimum conductivity despite the absence of carriers at the Dirac point [7]. This non-zero conductivity is likely due to the random distribution of charged impurities in graphene [8] which results in electron-hole puddles [9, 10]. Even as the average concentration of charge carriers tends toward zero, networks of these puddles may result in some remnant conduction [11, 12].

1.2 Potential to control graphene electronic structure

The electronic behavior of graphene can be altered in a variety of ways dependent on the desired property. This has the effect of making graphene a promising base material for many applications. For example, ultraviolet radiation has been used to tune the work function at graphene/semiconductor interfaces [13]. Other examples of tuning the electronic behavior of graphene include tuning the plasmonic phase velocity to investigate the graphene electron Fermi liquid for nonlocal responses [14] and tuning the band structure of graphene moiré superlattices by controlling the interlayer separation of graphene heterostructures with hydrostatic pressure [15].

In this work, we search for routes to tune the electronic structure and behavior of graphene by decorating the graphene surface with adatoms and nanoparticles. By adding these materials to the surface of graphene, we seek to induce a larger spin-orbit coupling to graphene and open a significant band gap.

1.3 Similar Experimental Works

1.3.1 Other adatoms on graphene

Similar motivations have led a variety of experimental studies of graphene with metallic adatoms. For small coverage percentages of indium, the adatoms are found to electron dope the graphene and rapidly decrease the mobility. The indium adatoms act as long-range Coulomb scattering centers and increase the charge density inhomogeneity. Neither weak localization measurements nor nonlocal voltage measurements show evidence for inherited spin-orbit coupling [16, 17]. Similar results in magnesium, an atom like carbon with negligible spin-orbit coupling further demonstrates the lack of spin-orbit inheritance from indium adatoms [16]. Calcium also electron dopes graphene but does not match theoretical predictions for the minimum conductivity under such conditions [18]. In addition, lithium and potassium adatoms have been shown to electron dope and decrease the mobility of graphene while forming clusters even at cryogenic temperatures. However, these clusters still behave as charged impurity scattering centers [7, 19, 20].

Comparable measurements were also made with titanium, iron, and platinum adatoms on monolayer graphene. These materials also electron dope the graphene and decrease the mobility. These adatoms are shown to form clusters on the graphene surface at room temperature. However, for these materials the adatoms cause scattering inconsistent with standard $1/r$ Coulomb scattering [21]. Interestingly, iridium forms clusters at low temperature, of about 100 adatoms, and is shown to electron dope with an efficiency of about $1e$ per cluster. For large coverage, charged impurity scattering is also inadequate for describing iridium adatom behavior [22, 23].

Of particular interest is the behaviour of gold adatoms on graphene because in addition to having a large spin-orbit coupling, gold is also used to fabricate contacts onto the graphene surface. Gold adatom behavior is similar to indium adatoms. Gold atoms electron dope

the graphene and decrease the mobility, scattering like isolated charged impurities. If the device is warmed to room temperature, then the gold diffuses across the surface and forms clusters. These cluster are less efficient dopants than isolated gold adatoms. In addition, gold adatoms are shown to be useful for the tuning of neutral valley currents [24, 25].

Interestingly, graphene grown by copper based CVD has been shown to inherit a spin-orbit coupling 3 times stronger than that of exfoliated graphene devices which is measured by an enhancement to the nonlocal voltage signal measured in Hall bar devices. This increase seems to be due to the presence of copper nanoparticles left behind after the copper etching process. However, similar results were acquired for devices with gold nanoparticles on epitaxial graphene as well [26]. Average particle sizes for both gold and copper were around 30-40 nm, in contrast to isolated adatoms which are much smaller. This indicates that each nanoparticle is comprised of several gold or copper atoms, giving them a larger number of protons. As discussed in Chapter 2, materials with a larger number of protons will have a larger spin-orbit coupling. This is likely why copper and gold nanoparticles induce spin-orbit coupling to graphene while single-particle adatoms of gold have been unsuccessful in similar endeavors.

1.3.2 Graphene heterostructures

Other techniques presented to induce a spin-orbit coupling to graphene are: creating heterostructures involving spin-orbit materials or placing graphene onto substrates with large spin-orbit coupling terms.

For example, experimental evidence has been shown that in heterostructures of graphene and few-layer WS_2, the graphene inherits spin-orbit coupling, dominantly of the Rashba type, from the WS_2 which leads to quantum spin Hall behavior even up to room temperature [27]. This Rashba type spin-orbit coupling is easily seen in the weak antilocalization corrections to the conductivity [28–30]. In addition, heterostructures of graphene with MoS_2 or WSe_2

causes acquisition of Rashba type spin-orbit coupling with strong electron-hole symmetry in the graphene [31] and anisotropic spin relaxation times evolving from a strong valley-Zeeman spin-orbit coupling, where the spins are coupled to the valley degree of freedom [32]. Furthermore, evidence of a spin-orbit coupling being induced to bilayer graphene by proximity to WSe_2 has also been shown [33].

In addition, graphene on substrates with large spin-orbit coupling, such as WS_2, have been shown to induce a large spin-orbit coupling to the graphene. This is shown in robust weak antilocalization in the device and spin relaxation times smaller than those in pristine graphene [28]. In fact, graphene on transition metal dichalcogenides as substrates, including WS_2, MoS_2, and WSe_2 are incredibly versatile with spin-orbit splittings induced that are about 100 times larger than inherent to pristine graphene. Furthermore, this inducement holds up for a variety of mobilities, graphene thicknesses, and for both electrons and holes. In addition to Rashba type spin-orbit signatures shown via weak antilocalization, spin-valley signatures are also shown in a beating resonance in the Shubnikov de Haas oscillations [34, 35].

1.4 Outline

In this work, we experimentally probe the effect of two types of adatoms, tungsten and osmium, in addition to one type of nanoparticle, Bi_2Te_3, on the electronic properties of graphene. Overall, the effect of tungsten adatoms on graphene are strikingly consistent with other metallic adatoms, despite the devices having not been cleaned of fabrication residues. On the other hand, osmium adatoms on graphene behave differently from other metallic adatoms in such a way as to challenge the simple models employed for describing the scattering mechanisms. Overall, neither adatom was conclusively proven to induce a *large* spin-orbit coupling to graphene but osmium-decorated graphene displayed anomalous

behavior in comparison to other adatoms and deviations from usual magnetoresistance in graphene calls for further exploration. In addition, preliminary observations reported here for Bi_2Te_3 nanoparticles do not reproduce intriguing results seen in another study.

We organize this discussion as follows: we begin with the general electronic structure of graphene, followed by the electronic structure when decorated with metallic adatoms in Chapter 2. The behavior of electrons in graphene within a magnetic field are discussed in a description of the quantum Hall effect, Shubnikov de Haas oscillations at large field, and weak localization corrections to the resistance at low field. In Chapter 3, we discuss the effects of tungsten adatoms in dilute quantity on graphene. In Chapter 4, the effects of osmium adatoms on graphene are examined in three different types of devices. In Chapter 5, we report preliminary measurements on Bi_2Te_3 nanoparticles on a monolayer graphene device. Finally we conclude with a brief discussion toward the applicability of this work beyond tungsten and osmium. Appendices are included to more thoroughly examine the: fabrication procedures used to create graphene devices (A), a comparative analysis of graphene cleaning procedures using AFM surface roughness measurements (B), and preliminary observations of lithium adatoms (C).

Chapter 2

Graphene and Decorated-Graphene Theory

2.1 Introduction

Graphene is an allotrope of carbon arranged in a honeycomb lattice of only carbon atoms in a single plane. This makes it different from the other forms of carbon because it is two-dimensional (2D). In addition, due to its unique electrical and mechanical properties, it has become largely studied both theoretically and experimentally. In this chapter, we will discuss the unique electronic properties that graphene lends to the field of materials science and their application to the following chapters.

2.2 Graphene electronic properties

2.2.1 Lattice structure

A single layer of monolayer graphene is the building block for other 2D and quasi-2D materials such a bilayer graphene and bulk graphite. Each monolayer is a honeycomb lattice

of carbon atoms in a single plane. Because the honeycomb lattice is not a Bravais lattice, it is equivalently taken to be two triangular sublattices, often referred to as sublattices A and B. This lattice is shown in Figure 2.1 with blue and red representing carbon atoms on the two sublattices.

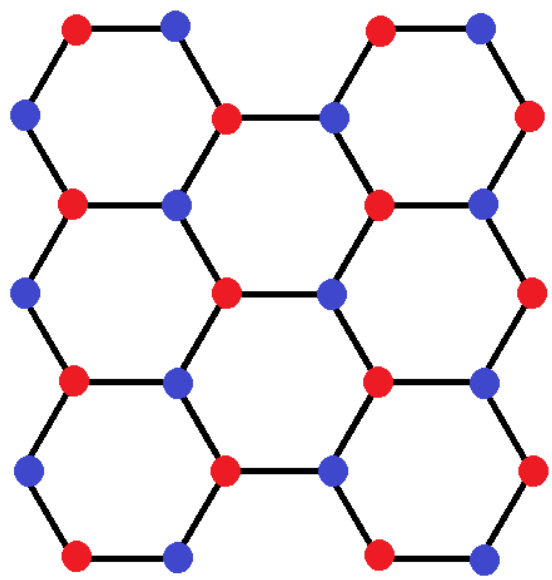

Figure 2.1: A top-down view of the honeycomb lattice of graphene with the A and B sublattices shown in blue and red.

The electronic structure of a base carbon atom is: $(1s)^2(2s)^2(2p)^4$. In solids, the 1s electrons are inert while the 2s and 2p electrons of each atom may hybridize. In the case of carbon, there are multiple hybridization options. However, in order to form a honeycomb lattice, the hybridization occurring is the combination of an s-orbital with the p_x and p_y orbitals to form three sp^2 orbitals arranged at 120° which forms three covalent σ bonds [36]. The remaining p_z orbital is in the plane perpendicular to the plane of the sp^2 hybrid orbitals and forms a delocalized π bond [37].

We define the lattice as follows: an infinite, free-standing, and flat sheet of graphene with periodic boundary conditions such that the Bravais lattice is chosen where the lattice

vectors are a_1 and a_2 and the nearest neighbor vectors of a chosen carbon atom are d_1, d_2, and d_3. Here we take lattice vectors:

$$\vec{a_1} = \frac{3a}{2}\vec{x} + \frac{\sqrt{3}a}{2}\vec{y}, \qquad \vec{a_2} = \frac{3a}{2}\vec{x} - \frac{\sqrt{3}a}{2}\vec{y}. \tag{2.1}$$

And the nearest neighbor vectors are:

$$\vec{d_1} = \frac{a}{2}\vec{x} + \frac{\sqrt{3}a}{2}\vec{y}, \qquad \vec{d_2} = \frac{a}{2}\vec{x} - \frac{\sqrt{3}a}{2}\vec{y}, \qquad \vec{d_3} = -a\vec{x}, \tag{2.2}$$

where a is the length of the carbon-carbon bond [38]. These vectors are included as labeled light-blue arrows in the lattice diagram of Figure 2.2.

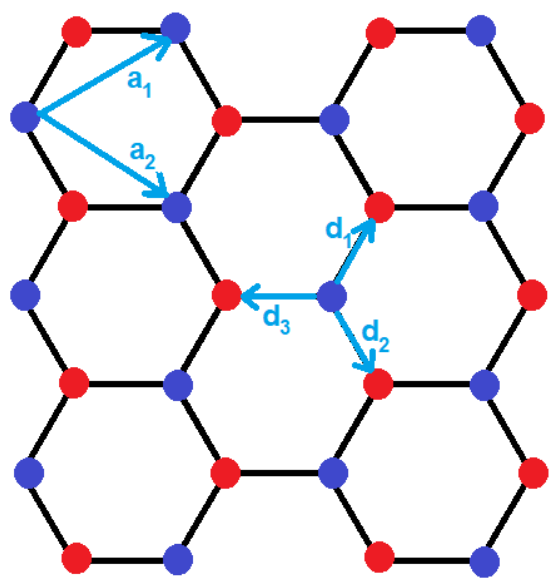

Figure 2.2: The honeycomb lattice with Bravais lattice vectors and nearest neighbor vectors.

The first Brillouin zone of a honeycomb lattice, found by intersecting the middle of the reciprocal lattice vectors [39], turns out to be another honeycomb lattice, but rotated by 90°. A diagram is shown in Figure 2.3 with the black honeycomb shape representing the

bonds between six carbon atoms in blue and orange (for the A and B sublattices). The first Brillouin zone is outlined in green and labeled FBZ. It is found by drawing connecting lines between the three carbon atoms of each sublattice, as shown in light orange. It is easy to see that for a honeycomb lattice, the lattice is only uniquely described by two points. All other points on the lattice can be found by translations of those two points. For this reason, we can see that only two points of the FBZ will be unique as well. These are typically called K and K', as shown in Figure 2.3.

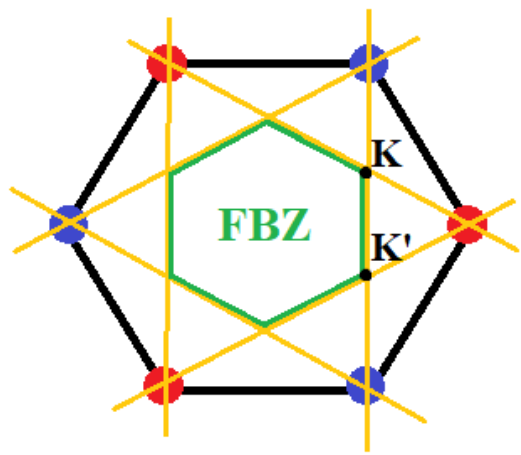

Figure 2.3: The first Brillouin zone (FBZ) of the graphene honeycomb lattice extracted by drawing connecting lines to each pair of atoms in the two sublattices. These lines are shown in orange. The FBZ is identified by a dark green outline and dark green label. The two symmetry points are shown in black dots labeled K and K'.

The reciprocal space symmetry points K and K', hereafter called the Dirac points, are defined by the vectors:

$$\vec{K} = \frac{2\pi}{3a}\vec{x} + \frac{2\pi}{3\sqrt{3}a}\vec{y}, \qquad \vec{K'} = \frac{2\pi}{3a}\vec{x} - \frac{2\pi}{3\sqrt{3}a}\vec{y}. \tag{2.3}$$

where a is again the carbon-to-carbon bond length of about 1.42 Å [38].

2.2.2 Graphene band structure: the tight-binding model

Hamiltonian of pristine graphene

Before graphene was experimentally realized, Wallace theoretically derived the band structure of graphite and its monolayer building blocks [1]. A brief subset of other resources for this derivation can be found in References [40–43]. We rather closely follow the derivation of Sir Anthony Leggett at University of Waterloo in his 2010 lecture series on quantum information processing [38].

In the tight binding model for the electronic band structure, we choose to limit hopping to only nearest neighbors (rather than next nearest and so on) for simplicity. The extension to next-nearest neighbors will be shown later in this section. The only orbitals relevant to this derivation are the π orbitals because they are left empty by the bonding processes of the other electrons. Then, the nearest-neighbor tight binding Hamiltonian equation is:

$$\hat{H}_g = -t \sum_{ij=nn} \sum_{\sigma} a^{\dagger}_{i\sigma} b_{j\sigma} + b^{\dagger}_{j\sigma} a_{i\sigma} \tag{2.4}$$

where t is the matrix element corresponding to the nearest neighbor hopping. This typically scales the derived energy band and is believed to be around 2.8 eV [40]. In addition, $a^{\dagger}_{i\sigma}$ is the creation operator for creating an electron with spin σ on site i of sublattice A and $a_{i\sigma}$ is the complementary annihilation operator. Similarly, $b^{\dagger}_{j\sigma}$ ($b_{j\sigma}$) is the creation (annihilation) operator for site j on sublattice B. We will choose a specific point in the lattice, any point on either sublattice will do, to label $\vec{R}^0_i$. For convenience, we choose the blue (sublattice A) point from which all three nearest neighbor vectors are labeled as $\vec{R}^0_i$. Then each of the nearest neighbor vectors $\vec{d_1}$, $\vec{d_2}$, $\vec{d_3}$ points to a carbon atom on the opposite sublattice nearest the chosen atom.

If we ignore the spin index, then the eigenfunctions of Eq. 2.4 are of the Bloch form such that:

$$\alpha_{\vec{k}} = \sum_j e^{i\vec{k}\cdot\vec{R}_j^0} a_j^\dagger e^{-i\vec{k}\cdot\frac{\vec{d_1}}{2}} \tag{2.5}$$

$$\beta_{\vec{k}} = \sum_j e^{i\vec{k}\cdot\vec{R}_j^0} b_j^\dagger e^{i\vec{k}\cdot\frac{\vec{d_1}}{2}}. \tag{2.6}$$

Then, each $a_j^\dagger$ or $b_j^\dagger$ creates an electron on unit cell j on the corresponding A or B sublattice.

The momentum-space representation for the Hamiltonian can be written in matrix form, with only off-diagonal elements:

$$\hat{H}_{\vec{k}} = -t \sum_{l=1}^{3} \begin{pmatrix} 0 & e^{i\vec{k}\cdot\vec{d_l}} \\ e^{-i\vec{k}\cdot\vec{d_l}} & 0 \end{pmatrix} \tag{2.7}$$

where each matrix element can be named and defined:

$$\Delta_{\vec{k}} \equiv -t \sum_{l=1}^{3} e^{i\vec{k}\cdot\vec{d_l}} \tag{2.8}$$

so that:

$$\hat{H}_{\vec{k}} = \begin{pmatrix} 0 & \Delta_{\vec{k}} \\ \Delta_{\vec{k}}^* & 0 \end{pmatrix}. \tag{2.9}$$

Substituting in the nearest neighbor vectors shown in Eq. 2.2, this simplifies to the same off-diagonal matrix with elements:

$$\Delta_{\vec{k}} = -te^{-ik_x a}[1 + 2e^{i(3k_x a/2)} \cos\left(\frac{\sqrt{3}k_y a}{2}\right)], \tag{2.10}$$

which gives the energy eigenvalues:

$$E_{\vec{k}} = \pm t\sqrt{1 + 4\cos\left(\frac{3k_x a}{2}\right)\cos\left(\frac{\sqrt{3}k_y a}{2}\right) + 4\cos^2\left(\frac{\sqrt{3}k_y a}{2}\right)}. \tag{2.11}$$

In this equation, the positive and negative energies are symmetric about $E_{\vec{k}} = 0$, as seen in Figure 2.4. The positive energy equation corresponds to the π band while the negative energy equation corresponds to the π^* band [40], which we now call the conduction and valence bands.

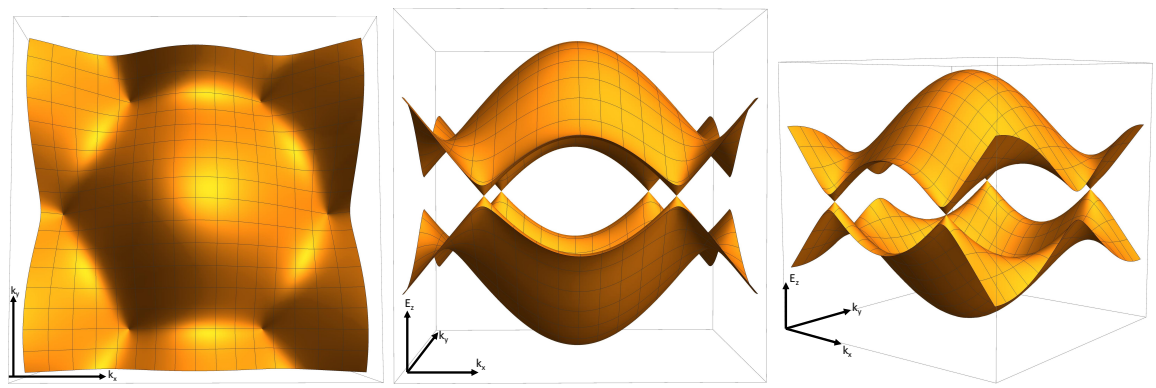

(a) (b) (c)

Figure 2.4: Three views of the energy of graphene versus momentum in a nearest-neighbor formalism.

The next step is to determine if there are any solutions for which the energy eigenvalues equal zero within the first Brillouin zone. The conditions that must be met for $E_{\vec{k}} = 0$ are either:

$$\frac{3k_x a}{2} = 2n\pi, \qquad \cos\frac{\sqrt{3}k_y a}{2} = -\frac{1}{2} \tag{2.12}$$

or:

$$\frac{3k_x a}{2} = (2n+1)\pi, \qquad \cos\frac{\sqrt{3}k_y a}{2} = \frac{1}{2}. \tag{2.13}$$

However, when $n = 0$, only Eq. 2.13 remains within the first Brillouin zone. In fact, when $n = 0$, Eq. 2.13 is exactly satisfied at the Dirac points K and K'. These linear bands form conical surfaces in the conduction band and inverted conical surfaces in the valence band that touch at each Dirac point. The nearly hour-glass shape that results from these surfaces at low energy are called valleys. In the low energy limit, we define the momentum near a Dirac point by:

$$\vec{q} \equiv \vec{k} - \vec{K}, \qquad |\vec{q}| \ll |\vec{K}|. \tag{2.14}$$

Then, the Hamiltonian matrix elements, $\Delta_{\vec{k}}$, are:

$$\Delta(\vec{q}) = -\frac{3ta}{2} e^{-iK_x a}(iq_x - q_y), \tag{2.15}$$

$$\Delta^*(\vec{q}) = -\frac{3ta}{2} e^{-iK_x a}(-iq_x - q_y) \tag{2.16}$$

Because it does not affect the physical results, we may then factor out and remove the imaginary component $-ie^{-iK_x a}$, such that:

$$\Delta(\vec{q}) = \frac{3ta}{2}(q_x + iq_y)[1 + \mathcal{O}(q/K)^2], \tag{2.17}$$

$$\Delta^*(\vec{q}) = \frac{3ta}{2}(q_x - iq_y)[1 + \mathcal{O}(q/K)^2]. \tag{2.18}$$

Then we define:

$$v_F \equiv \frac{3ta}{2\hbar} \approx 10^6 m/s, \tag{2.19}$$

which we call the Fermi velocity and nicely simplifies $\Delta(\vec{q})$ and $\Delta^*(\vec{q})$ to:

$$\Delta(\vec{q}) = \hbar v_F(q_x + iq_y)[1 + \mathcal{O}(q/K)^2], \tag{2.20}$$

$$\Delta^*(\vec{q}) = \hbar v_F(q_x - iq_y)[1 + \mathcal{O}(q/K)^2]. \tag{2.21}$$

Ignoring higher order corrections, we can rewrite the Hamiltonian:

$$\hat{H}_{\vec{k}} = \hbar v_F \begin{pmatrix} 0 & q_x + iq_y \\ q_x - iq_y & 0 \end{pmatrix}, \tag{2.22}$$

and we can see that the graphene Hamiltonian is also a function of the Pauli matrices:

$$\hat{H}_g = \hbar v_F(\hat{\sigma} \cdot \vec{q}), \tag{2.23}$$

with energy eigenvalues given by:

$$E(q) = \pm \hbar v_F |q|. \tag{2.24}$$

This means that the energies are only dependent on the magnitude of the momentum $\vec{q}$ and not on the direction. Another interesting note, is that this low-energy dispersion is *linear* in momentum - which is more obvious in Figure 2.5 - rather than parabolic as it would be for the vast majority of semiconducting materials. In addition, with graphene, the Fermi velocity is dependent only on the hopping parameter and lattice constant, and *not* on the energy.

Because the energy is symmetric around $E_{\vec{k}} = 0$ and $E_{\vec{k}} = 0$ is applicable at exactly the two Dirac points only, to half-fill the energy bands, the density of states at the Fermi energy must be 0. Pristine graphene, then, should have an electron of each spin on each atom such

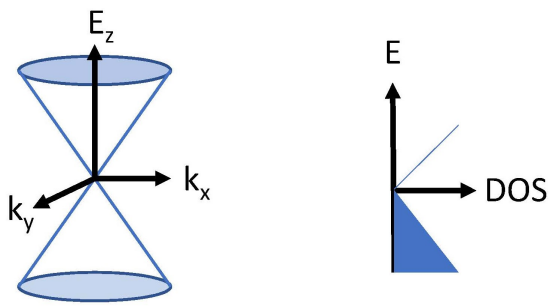

Figure 2.5: The low-energy dispersion relation for graphene is linear and the two bands meet at each Dirac point. The DOS is shown on the right; with the Fermi level meeting at $E = 0$, the valence band is full and the conduction band is empty.

that the total band is half-filled (or the valence band is perfectly filled while the conduction band is empty) and the Fermi energy lies at exactly the contact point $E_{\vec{k}} = 0$. This means that pristine graphene is a perfect semi-metal, rather than a metal or semiconductor. This distinction is shown in Figure 2.6 with the conduction band of a material shown in red and the valence band shown in blue. A metal typically has a reasonably large overlap between these bands, a semi-metal has either a small overlap or a single point (possibly degenerate) where the bands meet. A semiconductor, on the other hand, has an energy gap that separates the bands. This gap is typically small enough that it is possible to tune the Fermi level to be in either band which is when conduction occurs. Insulators have large energy gaps between the bands and as such are either difficult or impossible to tune the Fermi level such that conduction could occur.

The dispersion relationship shown in Eq. 2.24 is of the same form as for ultra-relativistic carriers quantum mechanically described by the 2D Dirac equation:

$$-iv_F\vec{\sigma} \cdot \nabla\Psi(\vec{r}) = E\Psi(\vec{r}) \tag{2.25}$$

This indicates that carriers in graphene may be described as so-called massless Dirac fermions [40].

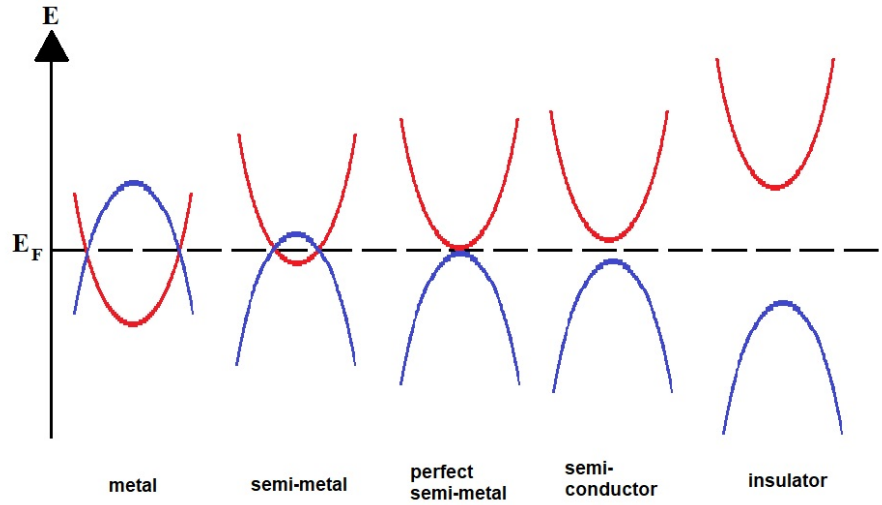

Figure 2.6: Typical low-energy band structure of various material types. The conduction band is shown in red and the valence band is shown in blue.

Finally, in order to properly discuss the final energy band solution for graphene, we must also extend our derivation beyond nearest neighbors. Indeed, if we include next-nearest neighbors as well, we acquire a Hamiltonian:

$$\hat{H}_g = -t \sum_{ij=nn,\sigma} (a^\dagger_{i\sigma} b_{j\sigma} + b^\dagger_{j\sigma} a_{i\sigma}) - t' \sum_{ij=nnn,\sigma} (a^\dagger_{i\sigma} a_{j\sigma} + b^\dagger_{i\sigma} b_{j\sigma} + a^\dagger_{j\sigma} a_{i\sigma} + b^\dagger_{j\sigma} b_{i\sigma}) \tag{2.26}$$

where t' is the next-nearest neighbor hopping parameter [40]. Because of the shape of the honeycomb lattice, we know that next-nearest neighbor hopping occurs between atoms on the same sublattice rather than on different sublattices, as for nearest neighbor hopping. The value for t' is approximated based on *ab initio* calculations to be $0.02t \leq t' \leq 0.2t$ [44], and experimentally shown to be $t' \approx 0.036t \approx 0.1eV$ [45]. If we now solve for the energy eigenvalues of this systems, we obtain:

$$E(\vec{k}) = \pm t\sqrt{3 + f(\vec{k})} - t' f(\vec{k}) \tag{2.27}$$

$$f(\vec{k}) = 2\cos(\sqrt{3}k_y a) + 4\cos(\frac{\sqrt{3}k_y a}{2})\cos(\frac{3k_x a}{2}) \tag{2.28}$$

which still simplifies to Eq. 2.24 in the low-energy limit [1, 40]. In Figure 2.7, we show the dispersion relationship for three values of t': $0.02t$, $0.1\ eV$, and $-0.2t$, where $t = 2.8\ eV$ and the values for t' are from (a) the smallest, (b) the experimental, and (c) the largest estimates given in [40].

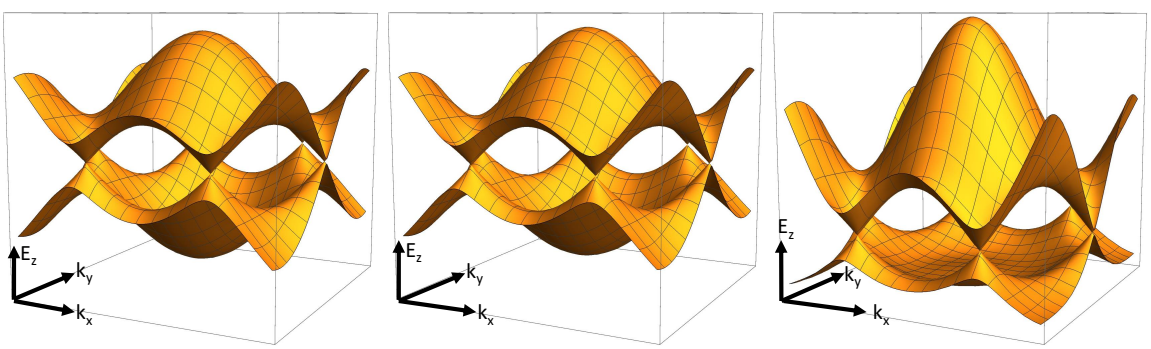

(a) $t' = 0.02t$ (b) $t' = 0.1eV$ (c) $t' = -0.2t$

Figure 2.7: The dispersion relation of energy versus momentum for (a) the range minimum for t' (b) the experimental estimation of t', and (c) the range maximum of graphene. We assumed $t = 2.8\ eV$.

Spin-orbit coupling

Because graphene has a negligible spin-orbit coupling intrinsically, we would like to induce a more substantial spin-orbit coupling by depositing adatoms onto the graphene surface in pursuit of realization of the Kane-Mele Hamiltonian. As such, the adatoms we will focus on are those with a large inherent spin-orbit coupling. Spin-orbit coupling is the physical effect of an interaction between the orbital angular momentum and the spin angular momentum. It is a relativistic effect and occurs for electromagnetic bound states. In such states, the

motion of an electron within its orbital causes a magnetic component to the orbital Coulomb potential and the spin is acted upon by the force resulting from that magnetic field.

The energy of a spin-orbit interaction (Δ_{SO}) is known to be related to the number of protons (Z) in the atom's nucleus, the orbital radii (r which may be approximated by the nth Bohr radius r_B), and the spin and orbital angular momenta ($\hat{S}$ and $\hat{L}$) [46] via:

$$\Delta_{SO} \propto \frac{Z}{r^3}\hat{L} \cdot \hat{S}, \tag{2.29}$$

then after replacing r with the Bohr radius r_B:

$$\Delta_{SO} \propto \frac{Z^4}{n^6}\hat{L} \cdot \hat{S}. \tag{2.30}$$

For spin-half charge carriers such as electrons, this becomes:

$$\Delta_{SO} \propto (\frac{Z^2}{n^3})(\frac{j(j+1) - l(l+1) - 3/4}{l(l+1)(2l+1)}). \tag{2.31}$$

This equations indicates that the spin-orbit coupling of individual atoms is highly dependent on their number of protons in the nucleus. In this way, we naively assign the following rule-of-thumb: the larger the atom, the more spin-orbit coupling it may induce upon a graphene sheet. For this reason, we focus on larger Z adatoms such as tungsten and osmium.

Adatom-decorated graphene

In order to account for the spin-orbit coupling interactions present on graphene with adatoms that have large spin-orbit coupling, we need to include more than the standard nearest-neighbor or next-nearest-neighbor terms in the Hamiltonian. Instead, we will follow Kane & Mele [47, 48] which shows that the spin-orbit interaction can be included as both a mirror-symmetric and a non-mirror-symmetric interaction in addition to the standard

nearest-neighbor Hamiltonian. In this discussion, the notation for the graphene Hamiltonian is as follows:

$$\hat{H}_g = -i\hbar v_F \psi^\dagger (\sigma_x \tau_z \partial_x + \sigma_y \partial_y)\psi, \tag{2.32}$$

with v_F as the Fermi velocity, σ_z representing states on the A or B sublattices, τ_z representing states at the Dirac points, and ψ solutions to the low-energy electronic wavefunctions. This is the effective mass Hamiltonian for graphene assuming only nearest-neighbor interactions with the same energy eigenvalues, Eq. 2.24. In this formulation, when ignoring spin, then the degeneracy at $\vec{q} = 0$ is protected by symmetry. Then, terms that are proportional to a staggered sublattice potential (σ_z or $\sigma_z\tau_z$) could be used to open a band gap. By including a term $\sigma_z\tau_z s_z$, where s_z accounts for the electron spin, a band gap should open while respecting all graphene symmetries including mirror symmetry about the plane. This type of spin-orbit coupling, often called intrinsic spin-orbit coupling, (as opposed to an asymmetric, or Rashba, coupling that does not respect mirror symmetry about the plane) can be represented by the Hamiltonian:

$$\hat{H}_{SO,I} = \lambda_{SO} \psi^\dagger (\sigma_z \tau_z s_z)\psi, \tag{2.33}$$

with eigen-energies:

$$E(\vec{q}) = \pm\sqrt{(\hbar v_F q)^2 + {\lambda_{SO}}^2}, \tag{2.34}$$

which leads to an energy gap of $2\lambda_{SO}$ [48].

On the other hand, if mirror symmetry is not preserved, such as by the introduction of a perpendicular electric field or by the presence of a substrate beneath the graphene, then another spin term must be included as well. This is the Rashba spin-orbit interaction and can be represented by the Hamiltonian:

$$\hat{H}_{SO,R} = \lambda_R \psi^\dagger (\sigma_x \tau_z s_y - \sigma_y s_x)\psi \tag{2.35}$$

Furthermore, if the Rashba spin-orbit term is larger than the intrinsic spin-orbit term, i.e. $\lambda_R > \lambda_{SO}$, then the gap would close, leaving the electronic band structure of a zero-gap semiconductor with quadratic bands [48].

However, if both intrinsic and Rashba spin-orbit interactions are included such that the Rashba term obeys $0 < \lambda_R < \lambda_{SO}$, then a finite gap of $2(\lambda_{SO} - \lambda_R)$ occurs with only two edge states travelling through that gap. This is shown in Figure 2.8 with the quadratic conduction and valence bands shown in red and blue respectively and the edge states shown in black.

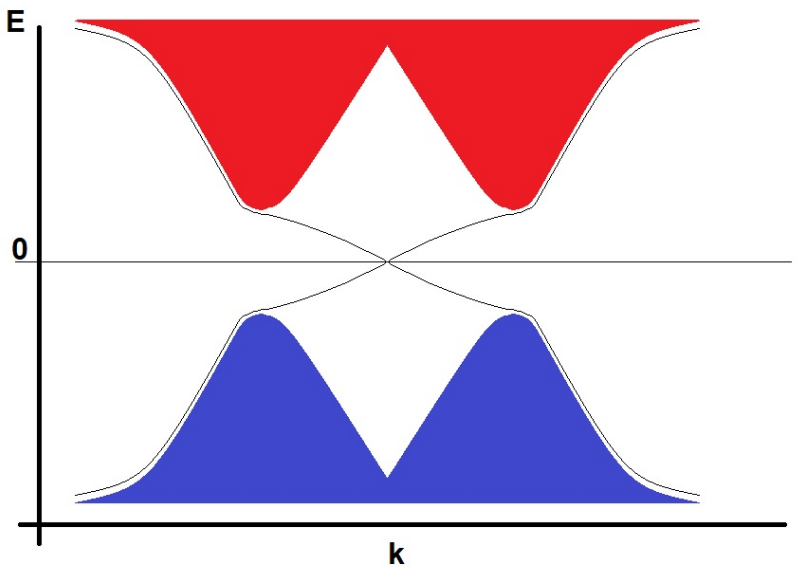

Figure 2.8: Graphene's dispersion relation includes quadratic conduction and valence bands in red and blue and two spin-polarized edge states shown in black.

This indicates that while Rashba spin-orbit interaction violates s_z conservation, the bulk band gap remains intact while gapless edge states cross at the Brillouin zone boundary. Time reversal symmetry prevents backscattering processes resulting in these spin-filtered edge states being stable against weak interactions and disorder. In a low temperature system, the ballistic transport can be described by a Landauer-Büttiker [49] formalism such that in

a two-terminal measurement, there would be quantized charge conductance:

$$G = \frac{2e^2}{h}, \tag{2.36}$$

accompanied by spin accumulation at the edges. Similarly, in a four-terminal geometry, a quantized spin current:

$$I_{spin} = \frac{eV}{4\pi}, \tag{2.37}$$

could be measured [48].

Because graphene intrinsically has a very small spin-orbit coupling, how can one add spin-orbit coupling to graphene such that the extraordinary mobility is not negatively affected and the band structure obeys the Kane-Mele model of conducting edge states with the bulk acting as an insulator? As described in the previous subsection, atoms with few protons have small spin-orbit coupling. Indeed, the Z^2 relationship indicates that small atoms, such as the carbon atoms in graphene, will have a much smaller spin-orbit coupling than atoms with significantly larger Z. Thus, References [50–52] propose a method to induce a large spin-orbit coupling to graphene via proximity to large Z adatoms.

For this method, the original graphene Hamiltonian would need a term that accounts for the presence of the adatom on the graphene and a term that accounts for hybridization between the adatom and the graphene. This assumes that the adatom preferentially sits in the central area of a graphene hexagon (hollow site) [53] after deposition. Other possible bonding sites for the adatom are the bridge (centered above and between two carbon atoms) or top (above a carbon atom) sites. The hollow and bridge sites tend to be energetically preferable to a position above a carbon atom (top site) and we choose adatoms with a preference for the hollow site because they should be the most effective adatoms for mediating spin-dependent next-nearest neighbor hopping without breaking the local sublattice symme-

try [50, 54, 55]. In addition, it is obvious that because we are discussing adatoms on one side of the graphene, and likely graphene supported by a substrate rather than suspended, there will likely be *both* an intrinsic spin-orbit coupling and a Rashba spin-orbit coupling present. However, if the outer shell electrons of each adatom come from p-orbitals, then the intrinsic spin-orbit coupling is predicted to dominate the Rashba coupling [50].

In this case the graphene Hamiltonian is replaced by the total system Hamiltonian:

$$\hat{H}_{sys} = \hat{H}_g + \hat{H}_{ad} + \hat{H}_{hy}, \tag{2.38}$$

where $\hat{H}_g$ is the graphene nearest neighbor Hamiltonian (Eq. 2.4) $\hat{H}_{ad}$ is the adatom Hamiltonian, and $\hat{H}_{hy}$ is the Hamiltonian for the hybridization between the adatom and the graphene. First, we rewrite the graphene Hamiltonian in simpler form:

$$\hat{H}_g = -t \sum_{ij=nn} \sum_{\sigma} a^{\dagger}_{i\sigma} b_{j\sigma} + b^{\dagger}_{j\sigma} a_{i\sigma} = -t \sum_{ij=nn} \sum_{\sigma} (a^{\dagger}_{i\sigma} b_{j\sigma} + HC_1), \tag{2.39}$$

where HC_1 is the second term in Eq. 2.4, which is the Hermitian conjugate of the first term in Eq. 2.4. Then, we also need to include a term involving the chemical potential of each adatom affecting the 6 sites surrounding it. $\hat{H}_g$ becomes:

$$\hat{H}_g = -t \sum_{ij=nn} \sum_{\sigma} (a^{\dagger}_{i\sigma} b_{j\sigma} + HC_1) + \delta\mu \sum_{\vec{R}_i} \sum_{j=1}^{6} c^{\dagger}_{\vec{r_j}} c_{\vec{r_j}}, \tag{2.40}$$

where $\delta\mu$ is the adatom chemical potential and $c^{\dagger}_{\vec{r_j}}$ is the creation operator for the vector $\vec{r_j}$ between the adatom located at $\vec{R}_i$ and its nearby carbons.

Next, we write the adatom Hamiltonian:

$$\hat{H}_{ad} = \sum_{\vec{R}} \left[\sum_{\alpha,m} \epsilon f^{\dagger}_{m\vec{R}\alpha} f_{m\vec{R}\alpha} + \sum_{\alpha,\beta=\uparrow,\downarrow} \lambda_{SO} (f^{\dagger}_{1\vec{R}\alpha} s^z_{\alpha\beta} f_{1\vec{R}\beta} - f^{\dagger}_{-1\vec{R}\alpha} s^z_{\alpha\beta} f_{-1\vec{R}\beta}) \right], \tag{2.41}$$

where $f^{\dagger}_{m\vec{R}\alpha}$ is the creation operator that fills the adatom d-orbital located at position vector $\vec{R}$ with magnetic quantum number $m = \pm 1$ and spin $\alpha = \uparrow, \downarrow$. As usual, s^z is a Pauli matrix and λ_{SO} is the spin-orbit coupling. Finally, ϵ is a scaling factor for setting the orbital energies in relation to the Dirac points of graphene.

Finally, to write the Hamiltonian representing the hybridization (or electron tunneling) between graphene and the adatoms, we need vectors that point from the adatom to the surrounding carbons. We will call these vectors $\vec{r_j}$. In addition, we ignore weak spin-orbit terms self-coupling the graphene electrons and Coulomb interactions. Then the hybridization Hamiltonian is described by:

$$\hat{H}_{hy} = -t_{hy} \sum_{\vec{R},\alpha,m} (iC^{\dagger}_{m\vec{R}\alpha} f_{m\vec{R}\alpha} + HC_2), \tag{2.42}$$

where t_{hy} is the hybridization hopping energy, $\vec{R}$ is the adatom location vector, $\alpha = \uparrow, \downarrow$ is the spin, $m = \pm 1$ is the angular momentum, HC_2 is the Hermitian conjugate of the first term in Eq. 2.42, and $C_{m\vec{R}}$ is the linear combination of the 6 vectors pointing from the adatom to the surrounding carbons, r_j, given by:

$$C_{m\vec{R}} = \frac{1}{\sqrt{6}} \sum_{j=1}^{6} e^{-i\frac{\pi}{3}m(j-1)} c_{\vec{R}+\vec{r_j}}. \tag{2.43}$$

2.2.3 Electronic Transport

Drude model

In a 2D electron gas, where electrons in a material move around in a background of stationary ions, the conductivity can be expressed in the Drude model for conductivity of a metal [56]. In this model, the resistivity of a material is defined as the proportionality

constant between the charge current and the electric field causing it:

$$\vec{E} = \rho\vec{j}, \tag{2.44}$$

where $\vec{E}$ is the electric field, ρ is the resistivity, and $\vec{j}$ is the current density. The charge current density may be defined by the number of charges present, the velocity with which they are moving, and the signed charge of the carriers via:

$$\vec{j} = -ne\vec{v}, \tag{2.45}$$

where n is the number of carriers (electrons), e is the elementary electron charge, and $\vec{v}$ is their velocity. However, we also know that within this material, there will be collisions of the electrons with boundaries, defects, other electrons, and the immobile lattice of ions. This scattering has an average relaxation time τ, or scattering rate of $1/\tau$. Thus the average velocity becomes:

$$\vec{v}_{avg} = \frac{-e\tau}{m}\vec{E}, \tag{2.46}$$

with m representing mass. Then this equation can be inserted into Eq. 2.45:

$$\vec{j} = -ne \times \frac{-e\vec{E}\tau}{m} = \frac{ne^2\tau}{m}\vec{E}. \tag{2.47}$$

By this, we define the conductivity (or the inverse of the resistivity) to be the proportionality factor between the current density and the electric field, i.e.:

$$\sigma_0 = \frac{\vec{j}}{\vec{E}} = \frac{ne^2\tau}{m}. \tag{2.48}$$

In a steady-state system, the rate for which electrons are gaining momentum from the electric or magnetic field balances the rate at which electrons are losing momentum due to

scattering [57]. This is expressed by:

$$\frac{m\vec{v}}{\tau} = e[\vec{E} + \vec{v} \times \vec{B}], \tag{2.49}$$

which can be written in terms of the x and y components of the electric field and velocity:

$$\begin{pmatrix} E_x \\ E_y \end{pmatrix} = \begin{pmatrix} \frac{m}{e\tau} & -B \\ B & \frac{m}{e\tau} \end{pmatrix} \begin{pmatrix} \frac{J_x}{en} \\ \frac{J_y}{en} \end{pmatrix}, \tag{2.50}$$

$$\begin{pmatrix} E_x \\ E_y \end{pmatrix} = \frac{1}{en}\frac{m}{e\tau} \begin{pmatrix} 1 & -B\frac{e\tau}{m} \\ B\frac{e\tau}{m} & 1 \end{pmatrix} \begin{pmatrix} J_x \\ J_y \end{pmatrix}. \tag{2.51}$$

Since

$$\sigma_0 = \frac{ne^2\tau}{m} = n|e|\mu, \tag{2.52}$$

where, μ is the mobility defined by

$$\mu \equiv \frac{|e|\tau}{m}. \tag{2.53}$$

We see that:

$$\frac{\mu}{\sigma_0} = \frac{1}{en}, \tag{2.54}$$

and finally, we have:

$$\begin{pmatrix} E_x \\ E_y \end{pmatrix} = \sigma_0^{-1} \begin{pmatrix} 1 & -\mu B \\ \mu B & 1 \end{pmatrix} \begin{pmatrix} J_x \\ J_y \end{pmatrix}. \tag{2.55}$$

Then from Eq. 2.44, we see the resistivity and compare Eq. 2.44 with Eq. 2.55:

$$\begin{pmatrix} E_x \\ E_y \end{pmatrix} = \begin{pmatrix} \rho_{xx} & \rho_{xy} \\ \rho_{yx} & \rho_{yy} \end{pmatrix} \begin{pmatrix} J_x \\ J_y \end{pmatrix} = \begin{pmatrix} \sigma_0^{-1} & -\mu B\sigma_0^{-1} \\ \mu B\sigma_0^{-1} & \sigma_0^{-1} \end{pmatrix} \begin{pmatrix} J_x \\ J_y \end{pmatrix}. \tag{2.56}$$

From 2.56, we know that $\rho_{xx} = \sigma_0^{-1}$ and $\rho_{xy} = -\mu B\sigma_0^{-1} = B/en$. Now, we can see that

the longitudinal resistance does not depend on magnetic field and the transverse resistance will vary linearly with magnetic field.

Conductivity in a magnetic field: classical Hall effect

The classical Hall effect was studied in the late 1800s by E.H. Hall, in pursuit of determining whether the force exerted on a wire carrying current in a magnetic field was due to the wire or due to the electrons within the wire. He discovered that a rectangular sheet carrying current I_x along the x-direction, within a magnetic field, B_z, in the z-direction, feels a Lorentz force that causes charge accumulation on the sides of the conductor. Eventually, this accumulation is balanced by the electric field, E_y, in the y-direction, resulting from that accumulation. In an equilibrium state, the new field due to accumulation, which is in the transverse direction to the wire, will balance the Lorentz force and current will only travel in the original direction [56]. This can be seen in Figure 2.9.

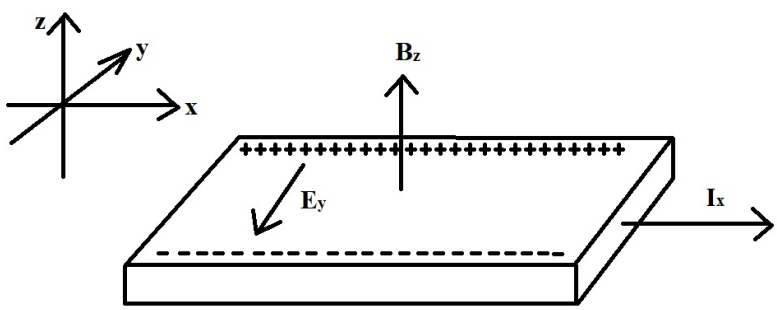

Figure 2.9: Carriers in a rectangular current-carrying conductor in a perpendicular magnetic field feel a Lorentz force that causes charge accumulation at the sides.

In a classical Hall effect system, there are characteristic resistances (or resistivities that we must understand. When a voltage is measured along the direction of the current, the longitudinal resistance (or resistivity) may be measured. This is characterized by the following equations:

$$R_{xx} = \frac{V_{xx}}{I_x}, \tag{2.57}$$

$$\rho_{xx} = \frac{E_x}{j_x} = \sigma_0^{-1}. \tag{2.58}$$

As discussed in the previous section, the value of the longitudinal resistivity is not dependent on the magnetic field and thus should be constant in a classical conductor. On the other hand, because of the charge accumulation on the sides of the conductor and resulting electric field, a voltage should be measurable in the y-direction as well. This results in a measurable transverse voltage, V_{xy}, which by simple calculation results in the transverse resistance, R_{xy}, by:

$$R_{xy} = \frac{V_{xy}}{I_x} = \frac{B}{ne}. \tag{2.59}$$

where I_x is the current in the x-direction as shown in Figure 2.9. The Hall coefficient is defined by:

$$R_H \equiv \frac{dR_{xy}}{dB} = \frac{1}{n_H e}. \tag{2.60}$$

High-field MR: Shubnikov de Haas oscillations

Experimentally, both the longitudinal and transverse resistance closely follow the Drude model trends when the magnetic field is small. However, at larger magnetic fields, the longitudinal resistance oscillates with amplitude increasing with magnetic field and the transverse resistance exhibits plateaus at cryogenic temperatures. An example of the oscillations in the longitudinal resistance at high magnetic field are shown in Figure 2.10.

These oscillations are a result of the step-like density of states for a 2D electron gas in

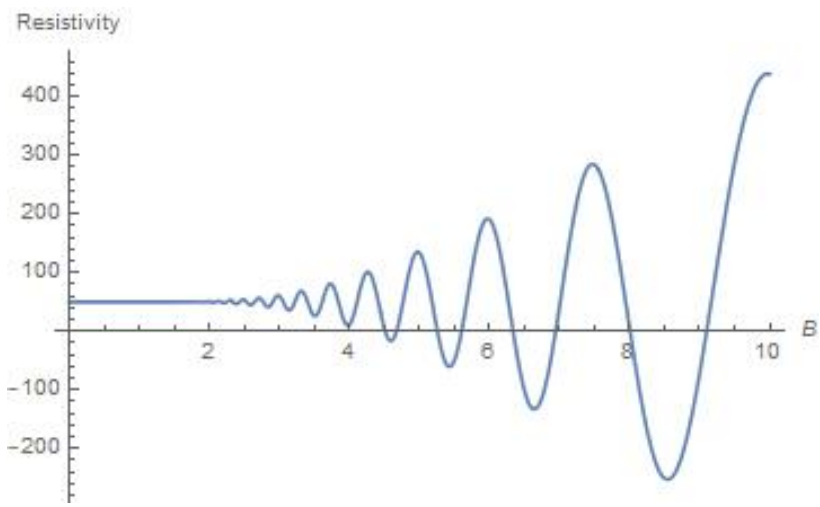

Figure 2.10: Oscillations in the longitudinal resistance of graphene

a quantizing magnetic field. If we ignore Zeeman splitting, then in a magnetic field, the density of states becomes a sequence of peaks separated by $\hbar\omega_c$ where ω_c is the cyclotron frequency of charge carriers in a magnetic field given by $\omega_c = \frac{eB}{m}$. This density of states is shown in Figure 2.11.

As the magnetic field increases, the energies of the Landau levels (the discrete energy levels of charge carriers in cyclotron orbits in a magnetic field) change. Because the resistivity is dependent on the Fermi energy, as the energy of the Landau levels change, the resistivity will go through oscillations because the Fermi energy moves from the center of one Landau level to the center of the next Landau level [57]. In a perfect system with no scattering, these peaks would instead be delta functions. However, in a real 2D electron gas, there will be scattering processes that cause the delta functions to smear out in energy.

Quantum Hall effect in graphene

Extending the classical Hall effect into quantum mechanics, we will now discuss the quantum Hall effect (QHE). This description is generic to 2D systems and has been measured in other systems such as GaAs heterostructures and silicon MOSFETS [58], as well as black

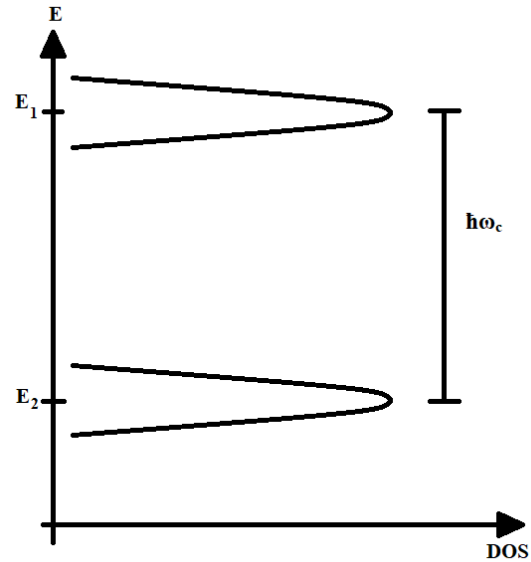

Figure 2.11: The density of states of a 2D electron gas in a quantizing magnetic field.

phosphorus [59]. In addition, measurements of the QHE in graphene are of particular interest and importance [60].

In high mobility devices, with large magnetic field perpendicular to the plane of the graphene, the Landau levels obey the following energy relationship:

$$E_n = sgn(n)\sqrt{2e\hbar v_F^2|n|B}, \tag{2.61}$$

where $sgn(n)$ is the sign of n, $\hbar$ is the Planck reduced constant, e is the elementary electron charge, v_F is the Fermi velocity in graphene, n is the Landau level number, and B is the magnetic field amplitude. As discussed previously in this Chapter, the allowed Landau energy levels E_n for $n = \pm 1, 2, 3, ...$ are a discrete spectrum of values with negative n for holes and positive n for electrons. In addition, when $n = 0$, there is a Landau level at the Dirac point $E_n = 0$. This Landau level is due to the unique structure of the band relationship for graphene and is electron-hole degenerate [61].

In this Landau level energy description of the 2D electron gas, such as is found in graphene sheets, the electron orbitals corresponding to different n values are localized such that there is one state per magnetic flux quantum in each Landau level. Then, we can define the filling factor, ν, as the fractional occupation of occupied Landau levels for a given applied magnetic field,

$$\nu = \frac{n_e \phi_0}{B}, \tag{2.62}$$

where n_e is the electron density, $\phi_0 = \frac{h}{e}$ is the flux quantum, and B is the magnetic field amplitude. By this relationship, we see that as the magnetic field increases, the filling fraction of Landau levels that are filled will decrease.

In the previous section, we mentioned that the transverse or Hall resistance should vary linearly with magnetic field as predicted by the classical Hall effect for large magnetic fields. However, in graphene, the Hall resistance increases with magnetic field but also exhibits several plateaus, which indicate quantization at certain magnetic fields. If we rewrite Eq. 2.62 for the electron density:

$$n_e = \frac{\nu B}{\phi_0}, \tag{2.63}$$

then:

$$R_H = \frac{B}{n_e e c} = \frac{B \phi_0}{\nu B e c} = \frac{h}{\nu e^2}. \tag{2.64}$$

Thus, we find that the Hall resistance is quantized with inverse relation to filling factor ν and units of $h/e^2 = 25812.8\ \Omega$ [62]. In high mobility graphene, plateaus that correspond to integer filling factors and fractional filling factors are found. The integer plateaus correspond to states where the Landau level is completely filled and a finite energy gap must be crossed to reach the next Landau level. In a real graphene system, impurities create local potentials that may trap the electrons such that as the filling factor changes by small amounts, the

extra electrons fill the localized states and do not contribute to the current. This causes a plateau in the resistance.

In high mobility 2D systems, it is also possible to observe states corresponding to fractional filling factors which also create plateaus in the Hall resistance [63]. The observation of these fractional quantum Hall states are due to the condensation of the 2D electron gas into a collective ground state [64]. Small changes in the fractional filling factor causes the excitation of quasi-particles that carry fractional charge and are similarly localized by impurities such that they do not contribute to the current [62].

Quantum spin and anomalous Hall effects in graphene

The quantum spin Hall effect is similar to the integer and fractional quantum Hall effect in that edge channel conduction occurs due to cyclotron orbitals of charge carriers bouncing along the device edges. However, unlike the usual quantum Hall effect, the quantum spin Hall effect occurs without an applied magnetic field. One possible way for this to occur is for a quantum Hall material such as graphene to have a large spin-orbit coupling. The Hamiltonian and resulting bulk insulation (band gap) with counter-propagating spin polarized edge channels was discussed in Section 2 of this chapter. The prediction for graphene becoming a 2D topological insulator from inherited spin-orbit coupling [48] and the inheritance of spin-orbit coupling to graphene via metallic adatoms [50, 51] is the underlying motivation for the entirety of this work.

In addition, the quantum anomalous Hall effect takes this process a step farther. If a quantum Hall material has a large spin-orbit coupling and a magnetic moment, then the magnetic moment will suppress one of the edge channels. This leaves a single edge channel, for a single type of spin, with quantized conductance through it. The three quantum Hall effects are shown in Figure 2.12 with the spin up channel shown in orange and the spin down channel in green. Theoretically this could also be realized by adatoms on graphene as long

as the adatoms contained both a large spin-orbit coupling and a magnetic moment.

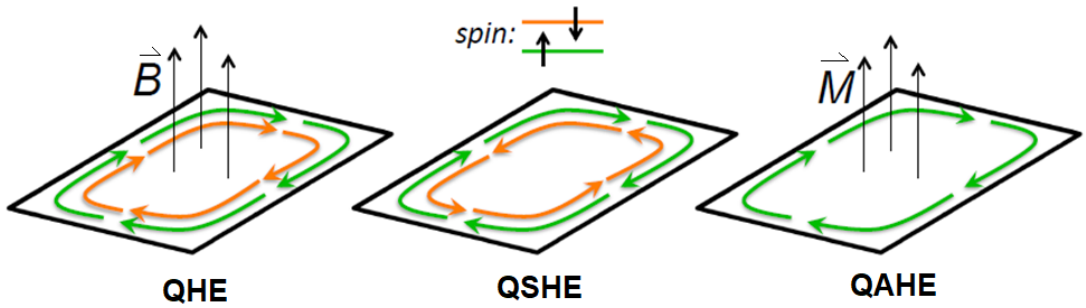

Figure 2.12: The QHE, QSHE, and QAHE explained diagrammatically. In the quantum Hall effect, an external applied magnetic field causes charge carriers to move in orbitals. This causes the bulk of a 2D sheet to be insulating, while carriers bounce along edge states in one direction or another based on their spin. The QSHE is similar but occurs without an applied magnetic field due to interactions between the motion of the charge carriers and the spin on those carriers. Finally the QAHE is analogous to the QSHE but one of the spin-polarized channels is suppressed due to a magnetic moment on the material.

Low-field MR: Weak localization in graphene

In systems that are not ballistic, electrons diffuse through the material undergoing many collisions that may be modeled as a random walk. A given electron starts at a location at a specified time and travels through the material with some probability of returning to its original location within a particular time period. This return probability is affected by the electron path intersecting either the paths of other electrons or other ions, as well as by the probability that the electron path coincides with impurities, material boundaries, or defects.

We consider an individual closed path than an electron could travel, such as is shown in Figure 2.13. Then, due to its wave nature, the electron has a well-defined phase [65, 66] and can travel the forward (clockwise in Figure 2.13) and the reverse (counterclockwise in Figure 2.13) path simultaneously; the wave travelling the forward path is correlated to the wave traveling the reverse path. Both the forward and reverse waves have an amplitude, P_A. At the starting point, the correlated forward and reverse waves interfere constructively

such that the probability of an electron returning to the initial location is $(2P_A)^2 = 4P_A^2$. If the electron travelling the forward path and the electron travelling the reverse path are not correlated, then that probability after constructive interference is instead $2P_A^2$. Because of this difference between the correlated and uncorrelated electron probability amplitudes, we can identify which interferences occur due to an electron self-interfering and due to separate electrons interfering with each other [67].

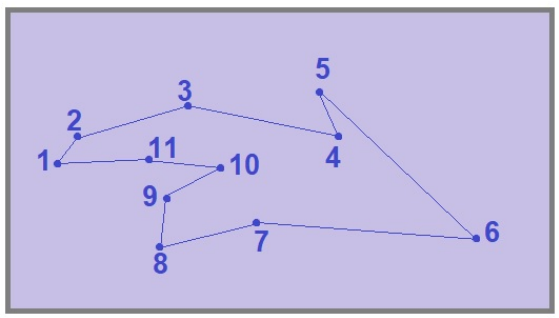

Figure 2.13: A possible closed path of an electron within a rectangular 2D material beginning at location labeled 1. The electron can travel either clockwise (1, 2, 3, ..., 11, 1) or counterclockwise (1, 11, 10, ..., 2, 1) to complete the same path.

Of course, a given electron has many possible paths it can take and so the probability that the electron returns to a location is given by:

$$\begin{aligned} P_{return} &= \int_0^\infty \frac{1}{4\pi Dt}(1 - e^{-t/\tau_{el}})e^{-t/\tau_\phi}dt \\ &= \frac{1}{4\pi D}\ln[\frac{\tau_\phi}{\tau_{el}} + 1], \end{aligned} \tag{2.65}$$

where $P_0(t) = 1/4\pi Dt$ is the return probability for a diffusivity D, $(1 - e^{-t/\tau_{el}})$ represents the elastic scattering time τ_{el} contribution, and e^{-t/τ_ϕ} represents the phase-coherence contribution.

At low temperature, the phase-coherence time (the average time before an electron loses track of its phase) is much longer than the elastic scattering time (the average time for an elastic scattering event to occur) and this interference effect produces a correction to the

conductivity. However, the return probability will also be dependent on magnetic field. This adjustment can be accomplished by solving the field-dependent diffusion equation to get:

$$P(B,t) = \frac{eB}{h\sinh\left(t/2\tau_B\right)}, \tag{2.66}$$

$$\tau_B = \frac{\hbar}{4eBD}. \tag{2.67}$$

At zero-field, the time-reversed path has the same phase as the original path, so the waves constructively interfere. In finite magnetic field, the magnetic flux enclosed by the traveled path rotates the phase but by the same amount on either the original or time-reversed path, thus the waves begin to destructively interfere until the accumulated phase reaches 2π, where complete destructive interference occurs. This interference leads to a correction to the return probability and, by extension, a correction to the conductivity [68].

There are two types of elastic scattering in graphene: intervalley scattering which occurs when scattering happens from one valley to the other and intravalley which is scattering within a valley. This distinction is shown in Figure 2.14. The intravalley scattering time in graphene is typically much shorter than the intervalley scattering time because it requires much smaller momentum exchanges. Large momentum scattering events that contribute to the intervalley scattering time are usually due to short-range impurities, grain boundaries, or lattice defects.

Extending this to graphene, McCann *et al.* [69, 70] derived the conductivity correction for graphene due to weak localization. They obtained:

$$\frac{\Delta\rho}{\rho_0^2} = -\frac{e^2}{\pi h}\left[F\left(\frac{B}{B_\phi}\right) - F\left(\frac{B}{B_\phi + 2B_i}\right) - 2F\left(\frac{B}{B_\phi + B_*}\right)\right], \tag{2.68}$$

where $F(z) = \ln(z) + \Psi(\frac{1}{2} + \frac{1}{z})$ with Ψ being the digamma function, and B_ϕ, B_i, B_* are the magnetic fields corresponding to the dephasing time (τ_ϕ), the intervalley scattering time

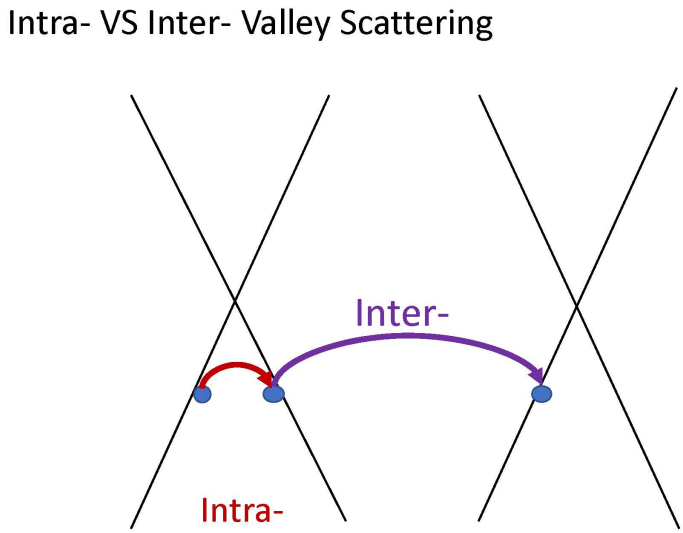

Figure 2.14: Inter- (intra-) valley scattering occurs between the two valleys (within one valley) as shown by an electron in blue scattering by the arrows.

(τ_i), and the intravalley relaxation time including trigonal warping and chirality-breaking elastic scattering such as occurs at surface ripples, atomically sharp defects, and dislocations (τ_*). Further, $\Delta\rho = \rho(B) - \rho_0$ where ρ_0 is the zero-field resistivity $\rho(B = 0)$. Finally, these scattering rates are related by:

$$B_{\phi,i,*} = \frac{\hbar c}{4De}\tau_{\phi,i,*}^{-1}. \tag{2.69}$$

Typically, graphene is closely coupled to the substrate material which may create sharp point-like scattering centers. This causes the intervalley scattering time to be shorter than the dephasing time. In addition, because intravalley scattering occurs with much smaller necessary momentum than intervalley events, the intravalley and trigonal warping time τ_* is much smaller than τ_i [71].

In addition, there is also a formalism for weak localization which includes spin-orbit coupling [72], shown in Eq. 2.70.

$$\frac{\Delta\rho}{\rho_0^2} = \frac{e^2}{2\pi h}\left[F\left(\frac{B}{B_\phi}\right) - F\left(\frac{B}{B_\phi + 2B_{asy}}\right) - 2F\left(\frac{B}{B_\phi + B_{asy} + B_{sym}}\right)\right], \tag{2.70}$$

where B_{asy} is the magnetic field corresponding to the asymmetric (Rashba) spin-orbit time and B_{sym} is the magnetic field corresponding to the symmetric (intrinsic) spin-orbit time. In this formalism, we find that the effect of spin-orbit coupling on the weak localization of graphene has two forms. A mirror symmetric spin-orbit coupling leads to a saturation in the size of the weak localization correction at low temperature [72]. On the other hand, a spin-orbit interaction that breaks mirror symmetry would lead to a correction of the weak antilocalization form. These descriptions of the weak localization in graphene will be used to examine reported weak localization measurements for information about the scattering in the device and evidence for the presence of spin-orbit coupling induced to the graphene.

Chapter 3

Electronic transport and scattering in graphene with tungsten adatoms

3.1 Abstract

The electronic transport properties of monolayer graphene have been studied before and after the deposition of a dilute coating of tungsten adatoms on the surface. For coverages up to 2.5% of a monolayer, we find tungsten adatoms simultaneously donate electrons to graphene and reduce the carrier mobility, impacting the zero- and finite-field transport properties. Two measurements indicate that the tungsten adatoms have settled to an effective height of 1 nm above the graphene surface. A proposed hypothesis for this effective height is given to be polymer residue covering much of the graphene surface after fabrication. This could also explain why the graphene does not seem to inherit spin-orbit coupling from the distributed tungsten adatoms.

3.2 Introduction

3.2.1 Motivation

The two-dimensional electronic system in single layer graphene is inherently unprotected from external influences and thus can be readily altered by proximity to supporting substrates and incidental adsorbates [7, 73]. A common and predictable outcome of such interactions is a more disordered electronic system. However, there is much interest in the potential to use surface adsorbates to advantageously alter the electronic properties of graphene. For example, one application is gas sensors that can accurately report the presence of single atoms or molecules [74–76]. Other groups are working toward the use of graphene for energy storage [77–81].

Another example is the recent focus on boosting the weak native spin-orbit interaction in graphene in an attempt to engineer topological band structure effects [50, 51] motivated by the desire to realize the Kane-Mele Hamiltonian [47, 48]. This Hamiltonian consists of the relativistic Dirac-like dispersion of graphene plus an intrinsic spin-orbit coupling term that together give rise to a quantum spin Hall insulator. To date, numerous theoretical works address the potential of several different atoms to play the role of spin-orbit donors leading to graphene-based topologically insulating systems [50–52, 82–91]. Furthermore, there is a wide range of proposals and evidence for altering the electronic properties of graphene with adatoms or nanoparticles beyond spin-orbit physics, including but not limited to: the possibility of novel magnetic systems [92, 93], interesting plasmonic systems [94, 95], and even superconductivity [96–98].

3.3 Experiment

Toward inducing a spin-orbit coupling to pristine graphene, we deposit tungsten adatoms

via *in situ* thermal evaporation of tungsten source wires. In this work we explore the effect of tungsten adatoms on the electronic transport of monolayer graphene at cryogenic temperatures with and without magentic field. Scattering times are found via measurements of the zero-field conductivity, Shubnikov de Haas oscillations of the magnetoresistance are measured, and weak localization in magnetoresistance is observed.

3.3.1 Dilution fridge methods

Electronic transport measurements were performed in a BlueFors LD-400 dilution fridge equipped with an American Magnetics Inc. 13.5 T superconducting solenoid, using a custom-built sample dipper, Figure 3.1(a)-(b), in which graphene samples are mounted on a ceramic stage with wire bonds connecting the sample bond pads to much larger gold stage pads. The back-gate is connected via a small custom metallic clamp holding the wafer at positions where the thermal oxide has been removed. This entire stage faces down and each stage pad is electrically connected via a fuzz button to the stage with phosphorus/bronze wiring thermally bound to the 4 K platform before exiting at the 50 K platform. The wiring is split to a breakout box outside the fridge where all measurements are conducted.

The ceramic stage faces downward, Figure 3.1(c), toward a small thermal evaporator, as shown in Figure 3.1(d), built from electrically isolated posts connected to a second copper/superconducting wire set and breakout box. This wiring channel also includes access to a heater, RTD thermometer, and RuOx thermometer located in the gold plated copper in surface contact with the back of the ceramic stage. Earlier versions of this dipper included only gold coated copper posts, visible in the bottom of Figure 3.1(d). However, because the vapor pressure of gold is so much lower than that of our source adatoms [99, 100], it became necessary to update the design to include tantalum extensions to the posts. Tungsten wires, 20 μm diameter, 99.95% purity, and annealed until smooth are suspended from these posts 4-8 cm below the sample for use as evaporation sources. The extension of the tantalum posts

reduced the distance between the evaporation source and the graphene device, which had the desirable effect of increasing the amount of adatoms deposited from equivalent source wires by a factor of 4. The evaporation rate is controlled by pushing a current through the wire while simultaneously monitoring changes occurring in the electronic transport.

During evaporation, the sample temperature rises to approximately 40 K while the rest of the cryostat remains close to 4 K. The density of deposited atoms is estimated from changes to the graphene transport caused by charge doping and independently by measuring the change in diameter of the wire sources. Graphene samples are produced starting with mechanical exfoliation of Kish graphite onto Si wafers having a 300 nm thermal oxide, followed by fabrication of electrical contacts by three methods: electron beam lithography and thin film Cr/Au deposition, shadow-masking of Cr or Cr/Au contacts, and standard electron beam lithography and thermal evaporation followed by AFM brooming to clean the surface of residual polymer resist (PMMA). These processes are examined in detail in Appendix A.

Transport data is acquired before and after evaporation using standard low-frequency AC lock-in techniques. Applying a gate voltage, V_g, to the degenerately-doped Si substrate allows control of the free carrier density in graphene. Here we present results from two single layer graphene devices, before and after tungsten depositions. All measurements were taken at 4 K unless otherwise noted.

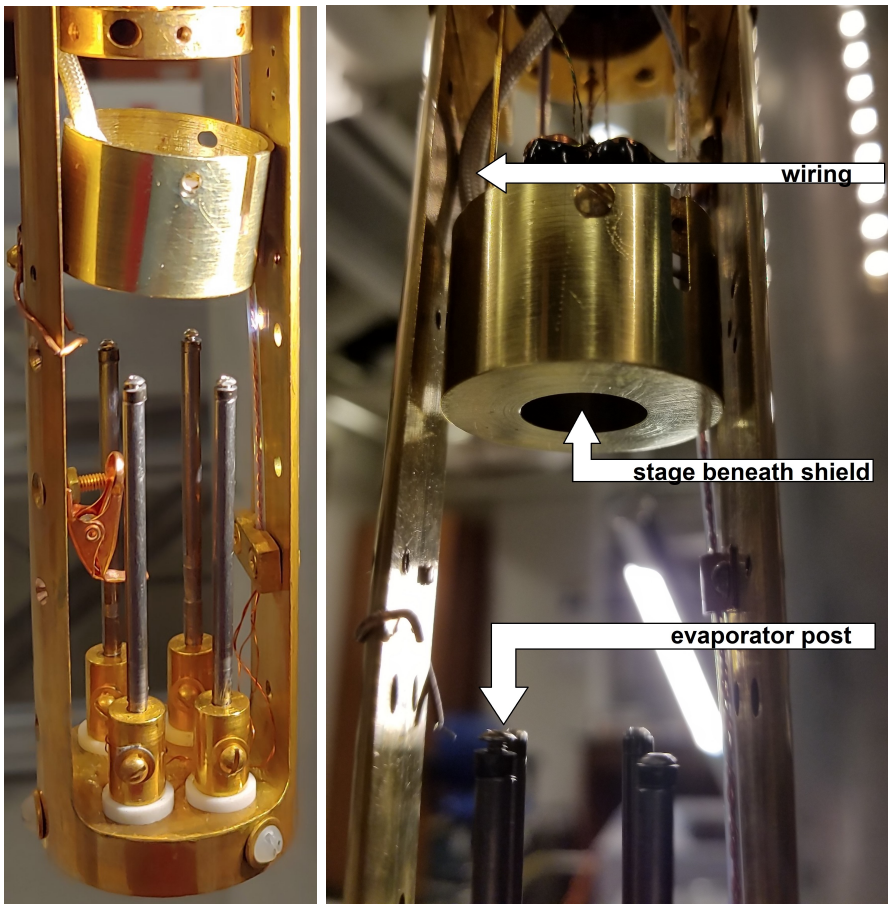

(a) dipper (b) labeled dipper

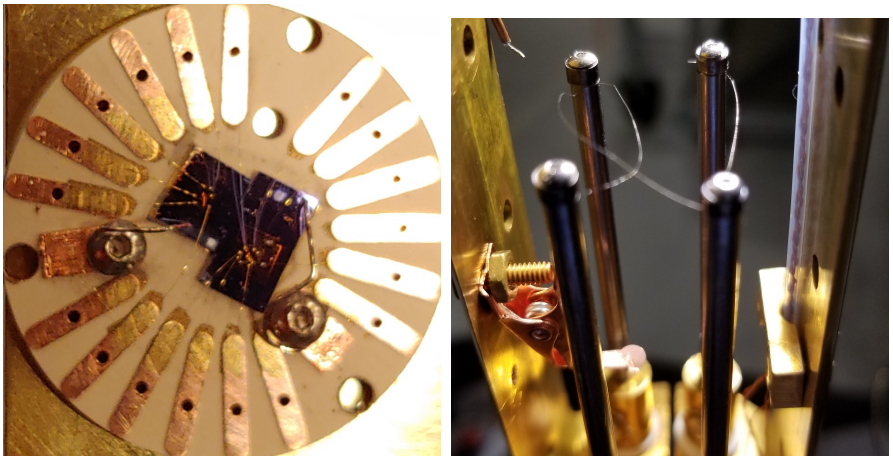

(c) ceramic stage (d) miniature thermal evaporator

Figure 3.1: (a)-(b) The photographed adatom dipper with (c) a ceramic stage and (d) local thermal evaporator.

3.3.2 Thermal evaporation of tungsten adatoms

We employ tungsten wires purchased from California Fine Wire Company as evaporation sources; these are shown in Figure 3.2(a) as delivered and are about 20 μm in diameter. However, due to the pulling process for making such tiny wires, the surface shows striations. In order to adequately estimate the amount of tungsten deposited, we must be able to measure the diameter of the wires. For this reason, the tungsten wires are annealed at 200 mA for 3 minutes while under vacuum, approximately 2 μTorr. This significantly smooths the surface of the wire, Figure 3.2(b). Short sections of this wire are mounted between two posts of a miniature thermal evaporator which is located in the cryostat, 8 cm directly below the sample stage. Up to three wires can be mounted for a single experimental run.

A DC voltage applied to the wire drives a current that resistively heats it to achieve evaporation. Typical currents are $\approx$ 150 mA. In this work two wires were employed, one for the first two evaporations, and a second for the third evaporation. Due to the approximate T^4 dependence of the power radiated by the extremely hot wire during evaporation [99, 101], the wire temperature rapidly equilibrates along its length so we assume uniform evaporation from a 1-cm-long suspended portion. The adatom density on the graphene can be estimated by geometry. We measure the tungsten wire radius by inspection in a scanning electron microscope before and after each experiment.

We estimate the adatom density by measuring the diameter of the tungsten wire source in a scanning electron microscope both before and after the experiment. Geometry then enables an estimate of the adatom density:

$$n_{dep} \;=\; \pi\left(r_i^2 - r_f^2\right) \times L \times \frac{\rho_W}{m_W} \times N_A \times \frac{1}{4\pi d^2}, \tag{3.1}$$

where r_i is the initial radius of the tungsten wire, r_f is the final wire radius, L is the length of the source wire, ρ_W is the density of tungsten, m_W is the atomic weight of tungsten,

N_A is Avogadro's number, and d is the vertical distance between the source wires and the sample stage. This method gives the final total density deposited by all three evaporations performed.

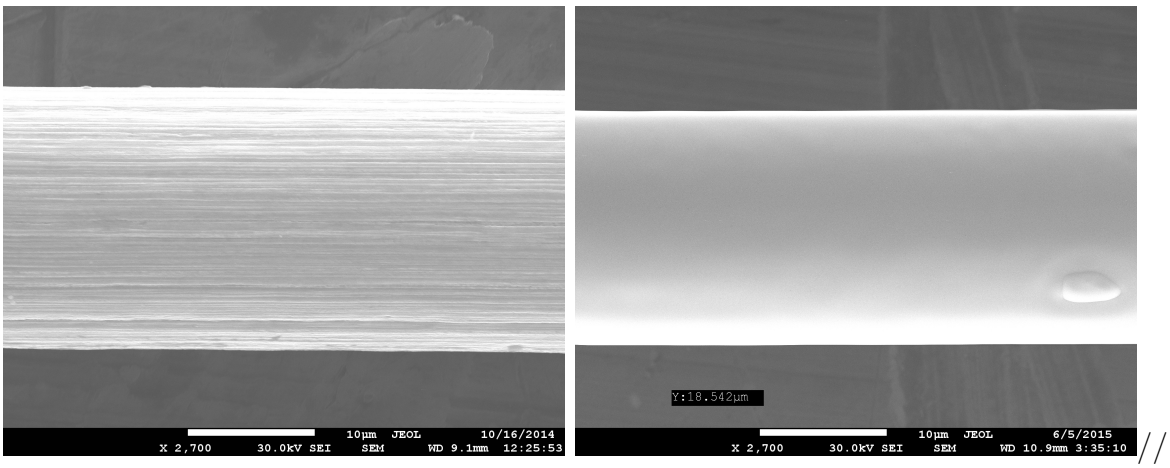

(a) tungsten wire (b) annealed tungsten wire

Figure 3.2: Scanning electron microscopy of tungsten wires (a) as purchased and (b) after a smoothing anneal

For the experiment discussed here, the first wire we measure $r_i = 10.2$ μm and $r_f = 9.7$ μm from the SEM images like those shown in Figure 3.2, and double this result to find the total density in the whole experiment, since the two wires used produced a nearly identical shift in charge doping and the second wire was lost during demounting. Thus the expected tungsten density after all three evaporations is found to be $n_{dep} = 5 \pm 1 \times 10^{13}$ cm^{-2}. The error bars are dominated by uncertainty in the measurement of the active length of the wire, particularly in how the wire radius changes near the evaporator posts which are thermally coupled to the cryostat.

3.3.3 Graphene device fabrication

Graphene samples are produced starting with mechanical exfoliation of Kish graphite onto Si wafers with 300 nm thermal oxide, followed by fabrication of electrical contacts by

electron beam lithography and thermally evaporated Cr/Au deposition. These processes are examined in detail in Appendix A. Transport data is acquired before and after evaporation using the application of a gate voltage, V_g, to control the free carrier density in graphene via:

$$n = \alpha(V_g - V_{g0}), \tag{3.2}$$

where the coefficient $\alpha = 7.0 \times 10^{10}$ cm^{-2}V^{-1} is calibrated by oscillations in the magnetoresistance at high fields. Here we present results from a single layer graphene sample etched by an O_2 plasma into a 2-micron-wide Hall bar as shown in the inset to Figure 3.3(a); similar behavior has been observed in a second sample. In addition, other devices were measured with both osmium adatoms and tungsten adatoms evaporated in different steps. This allowed for identifying the behavior of osmium independently from tungsten.

The deposition of tungsten atoms on to the surface of graphene impacts the electronic transport in several ways as will be presented. An independent measurement of the deposited adatom density is desirable, however, unattained at this time. The final density of evaporated tungsten that impacted the electronic behavior of graphene is found to be 5×10^{13} cm^{-2}, covering 2.5% of the unit cells in graphene (or just over 1 tungsten atom per 100 C atoms). We estimate the uncertainty in this value to be ±20%.

3.4 Results

3.4.1 Transport at zero magnetic field

Figure 3.3(a) shows the measured conductivity as a function of gate voltage for one device used in this study, starting with data obtained from the as-made device (red trace) and continuing with traces recorded after three successive depositions of tungsten atoms,

shown as the orange, green, and blue curves. Each trace exhibits a linear dependence on carrier density away from the conductivity minimum. This implies a constant carrier mobility

$$\mu = \frac{1}{e}\frac{d\sigma}{dn}, \tag{3.3}$$

which is observed to decrease after each evaporation. Moreover the charge neutrality point at the conductivity minimum of each curve is seen to shift to the left indicating electron doping of the graphene. Additionally, the slope of the conductivity versus density, $\frac{d\sigma}{dn}$, decreases suggesting a decrease to the mobility and an increase in carrier density inhomogeneity [17]. Broadly, these observations are consistent with prior works such as: the impact of potassium adatoms on graphene [7, 23], results from Ti, Fe, and Pt adatoms on graphene [21], Au adatoms [24], indium adatoms [16, 17], and iridium as well [22]. These altogether strongly suggest that tungsten adatoms donate electrons to graphene, becoming ionized impurities that enhance the scattering and reduce the mobility.

Away from the charge neutrality minimum in conductivity, the conductivity of graphene can be written as [8, 102, 103]

$$\sigma^{-1}(n) = \sigma_{ci}^{-1}(n) \ + \ \sigma_{sr}^{-1}, \tag{3.4}$$

reflecting two sources of scattering: screened charged impurities and short-ranged scattering such as might result from edges or vacancies.

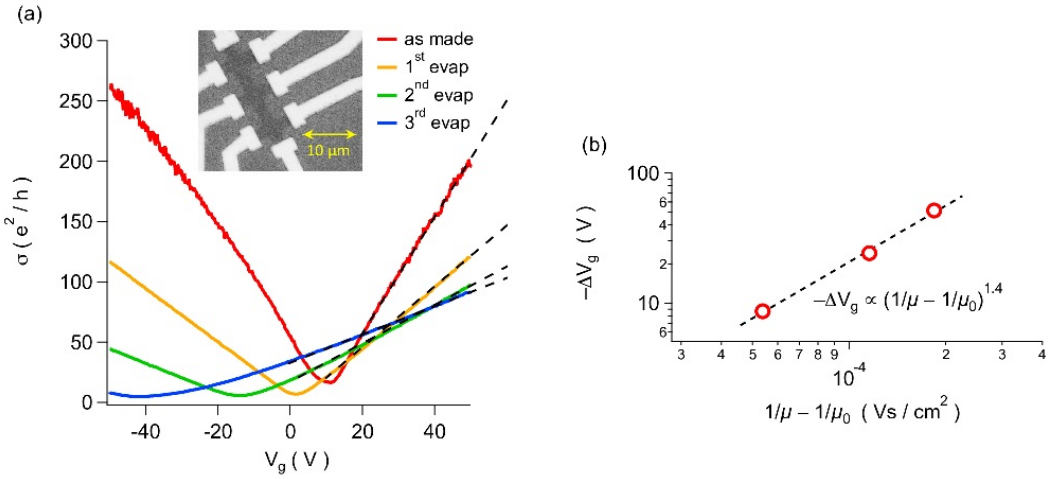

Figure 3.3: (a) The conductivity, σ, versus gate voltage, V_g, for the monolayer graphene Hall bar sample shown inset. The as-made device has a σ minimum at $V_g = 10$ V, which shifts left indicating electron doping after subsequent tungsten evaporations. Dashed lines show linear fits used to extract carrier mobility. (b) The gate voltage shift, $\Delta V_g = V_{g,min} - V_{g,0}$, of the minimum conductivity in part (a) for each evaporation, plotted against the change in the inverse mobility, where μ_0 is the mobility of the as-made trace. The shift has a power law dependence on the inverse mobility with slope of 1.4, consistent with point-like scattering [7, 24, 103].

In the case of screened charged impurities, the conductivity is linear in the carrier density:

$$\sigma_{ci}(n) = C|n|/n_{imp}, \tag{3.5}$$

where n_{imp} is the impurity density and C has been theoretically calculated [103] to be $C \approx 20\ e^2/h$ in the limit that the charged impurities lie in the graphene plane. Short-ranged impurities, on the other hand, lead to a conductivity that is independent of density. In many graphene-on-SiO_2 devices including those used in this work, $\sigma_{sr} >> \sigma_{ci}$, and thus the

conductivity is simply observed to be linear in density.

The conductivity data allow us to extract the added charge density,

$$\Delta n = \alpha \Delta V_g, \tag{3.6}$$

donated by the adatoms, by measuring the shift of the conductivity minimum along the gate voltage axis. The conductivity also allows us to extract the change in the impurity density:

$$\Delta n_{imp} = (C/e)(1/\mu - 1/\mu_0), \tag{3.7}$$

where we subtract off the contribution of the initial impurity distribution in the as-made sample. Naively, one might expect each adatom to donate one electron such that $\Delta n = \Delta n_{imp}$. However, we instead find the induced charge density to be $2-3$ times larger than the n_{imp} values extracted from the conductivity data of Figure 3.3(a). We note that to determine n_{imp} we use the aforementioned value $C = 20\ e^2/h$ which is strictly true only for $z = 0$, where z is the effective height of the impurities above the graphene plane. In fact the self-consistent theory of Adam *et al.* predicts [103] that C has a super-linear density dependence for $z > 0$, growing increasingly with z. Without *a priori* knowing the height of the adatoms above the graphene, we can make an estimate by first *assuming* that the increase in n_{imp} is in fact *equal* to Δn, and then applying this theory to calculate the value of z. The fact that C increases with z explains why n_{imp} is initially underestimated. The results of our analysis are given in Table I where we list the observed change in density, Δn, the n_{imp} values calculated from the slope $d\sigma/dn$ using $C = 20\ e^2/h$, and the calculated heights, z. With increasing W coverage, z approaches 1 nm. Although this is greater than the $z = 0.16 - 0.17$ nm separation predicted for tungsten atoms above the center of a graphene honeycomb by density functional theory (DFT) calculations [52, 104], it is not altogether unreasonable. We further note that predictions for the charge transfer from tungsten to

graphene range between 0.56 and 0.93 electrons/atom [105, 106]. Assuming the average of these would increase the calculated height by roughly 30%.

State of sample	Δn (cm^{-2})	n_{imp} (cm^{-2})	z (nm)
as made	0	2.9×10^{11}	0.08
1st evap	6.1×10^{11}	5.5×10^{11}	0.6
2nd evap	1.7×10^{12}	8.5×10^{11}	0.92
3rd evap	3.6×10^{12}	1.2×10^{12}	1.1

Table 3.1: Adatom-induced electron density Δn determined from shift in minimum conductivity; the impurity density $n_{imp} = (C/e)(1/\mu - 1/\mu_0)$; and the height of impurities above the plane, z, calculated using the theory of Adam *et al.* as discussed in the text [103].

In Figure 3.3(b) we plot the shift in gate voltage, $-\Delta V_g$, versus the change in the inverse mobility, $1/\mu - 1/\mu_0$. This quantity is both predicted and experimentally found to obey a power law,

$$\Delta V_g \propto (1/\mu - 1/\mu_0)^b, \tag{3.8}$$

where b is typically $1.2 - 1.3$ for point-like charged impurities [103]. In contrast, $b < 1$ for adatom clusters [7, 24]. For tungsten adatoms on graphene, we find $b = 1.4$. Thus altogether the zero-field conductivity implies that tungsten adatoms are isolated, charged impurities lying approximately 1 nm above the surface.

3.4.2 Comparison of transport and quantum scattering times

We now investigate the behavior of the transport and quantum scattering times, τ_μ and τ_q, as tungsten atoms are deposited on graphene. Both parameters are a measure of electron scattering, but where the single particle relaxation (or "quantum") time τ_q is sensitive to all scattering events, the transport time τ_μ only measures those that contribute to the resistance of the material. In the transport time, forward scattering processes are ignored. In standard

2D systems, backscattering, where

$$|\mathbf{k}_{final} - \mathbf{k}_{initial}| = 2k_F, \tag{3.9}$$

is the most efficient at limiting τ_μ. But these events are suppressed in single layer graphene [107] leaving right-angle scattering to have the strongest impact on the transport time. The scattering rates are found by integrating over the total angular scattering potential $Q(\theta)$ as

$$\frac{1}{\tau_q} = \int_0^\pi Q(\theta)\ (1 + \cos\theta)\ d\theta, \tag{3.10}$$

$$\frac{1}{\tau_\mu} = \int_0^\pi Q(\theta)\ (1 - \cos^2\theta)\ d\theta, \tag{3.11}$$

where factors of $1 + \cos\theta$ in each formula account for the suppression of $2k_F$ scattering, and the additional factor of $1 - \cos\theta$ in the transport scattering rate limits the effect of forward scattering.

The ratio τ_μ/τ_q can be used to discriminate between the type and location of scattering potentials. For instance, short-range (i.e. δ-function) impurities scatter equally into all angles and thus $\tau_\mu = 2\tau_q$ where the factor of 2 is linked to the absence of backscattering. On the other hand, Coulomb scattering leads to an increase in forward scattering events due to its long-ranged nature [108, 109], such that $\tau_\mu/\tau_q > 2$. Indeed, in high mobility GaAs 2D systems, τ_μ/τ_q can exceed 100 due to the exceptional purity of the host crystal and the fact that ionized impurities are removed many 10s of nm from the 2D layer.

In graphene on SiO_2, this ratio is expected to be small due to strong scattering caused by close coupling of the graphene sheet to the substrate, as was observed by Hong *et al.* [110]. In particular, theoretical work predicts that $\tau_\mu/\tau_q < 2$ for short-ranged scattering, $\tau_\mu/\tau_q > 2$ for (screened) Coulomb scattering when the impurities lie in the plane, and becomes increasingly larger for charged impurities that are set back a distance z above the plane [109]. The reason

is that the more distant a Coulomb scatterer is, the smaller the scattering angle will be which preferentially limits the quantum scattering time. Moreover, the ratio depends on whether impurities are either isolated or clumped together in clusters, in which case the charge doping efficiency and hence the number of ionized scatterers is reduced [24]. Indeed, for clusters the ratio τ_μ/τ_q is predicted to increase by roughly the number of impurities per cluster as the total scattering cross-section outstrips the rate of backscattering [111].

To learn more about the impact of tungsten adatoms, we have studied the τ_μ/τ_q ratio as it is impacted by tungsten evaporations. We extract the transport scattering time from the conductivity data of Figure 3.3 and the τ_q values from an analysis of Shubnikov-de Haas oscillations of the magnetoresistance at high magnetic fields. Both are performed over a range of carrier densities for electron-doped graphene. This was done in both the as-made device and after all following evaporations. The amplitude of Shubnikov-de Haas oscillations is generally well-described by the first term of the Lifshitz-Kosevich equation [112],

$$\frac{\delta\rho_{xx}}{\rho_0} = 4\ X_{th}\ e^{-\pi/\omega_c\tau_q}, \tag{3.12}$$

with the thermal factor

$$X_{th} = \frac{2\pi^2 k_B T/\hbar\omega_c}{\sinh(2\pi^2 k_B T/\hbar\omega_c)} \tag{3.13}$$

and where $\rho_0 = \rho(B = 0)$, and the cyclotron frequency

$$\omega_c = eB/m^* \tag{3.14}$$

with the effective mass

$$m^* = \hbar\sqrt{\pi n}/v_F. \tag{3.15}$$

Figure 3.4(a) shows a representative SdH trace at a density $n = 4.3 \times 10^{12}$ cm^{-2} after a

second tungsten evaporation. The logarithm of the amplitude of the oscillations, divided by ρ_0 and the thermal damping factor X_{th}, yields a straight line when plotted versus $1/B$ as shown in Figure 3.4(b), with a slope that is inversely proportional to the quantum scattering time [110, 113]. For this analysis, the linear fit is constrained to a y-intercept of 4, and the slope is proportional to the quantum scattering rate τ_q^{-1}. The transport and quantum scattering times we find are plotted in Figure 3.4(c) and (d), respectively. Both follow a roughly $\sqrt{n}$ dependence, shown by the dashed red curves.

In Figure 3.4(e) we plot the ratio of these scattering times as a function of carrier density, for the as-made sample and following each evaporation. A clear downward trend is visible with the ratio dropping from $6-7$ down to $3-4$ over the course of the depositions, and while the ratio is more or less constant in the as-made sample, with each evaporation a slight but clear increase in the slope emerges. The density range explored is limited by a combination of the shift in the minimum conductivity due to electron doping, and the associated decrease in mobility which smears out Shubnikov de Haas oscillations at lower densities. We compare these data to predictions from the theory of Hwang & das Sarma [109] for the variation of τ_μ/τ_q with the effective height z of charged impurities above the graphene sheet, for $z = 1$ nm and $z = 3$ nm. Assuming that charged impurity scattering in the as-made sample arises from oxide charges and dangling bonds in the underlying SiO_2 surface, 3 nm is a reasonable value given the few-nm RMS surface roughness of SiO_2, and is close to the 2 nm found previously for graphene-on-SiO_2 devices [110, 114]. The decrease to a 1 nm separation after the evaporations implies that ionized W adatoms lie closer to the surface and agrees with the value found above from consideration of the zero-field conductivity. As previously noted, however, the separation distance for tungsten adatoms predicted by DFT calculations is rather smaller, $z = 0.16-0.17$ nm [52, 104]. A similar discrepancy in separation distances was found for indium adatoms [17].

Finally we note that although the final impurity-graphene separation of 1 nm found from

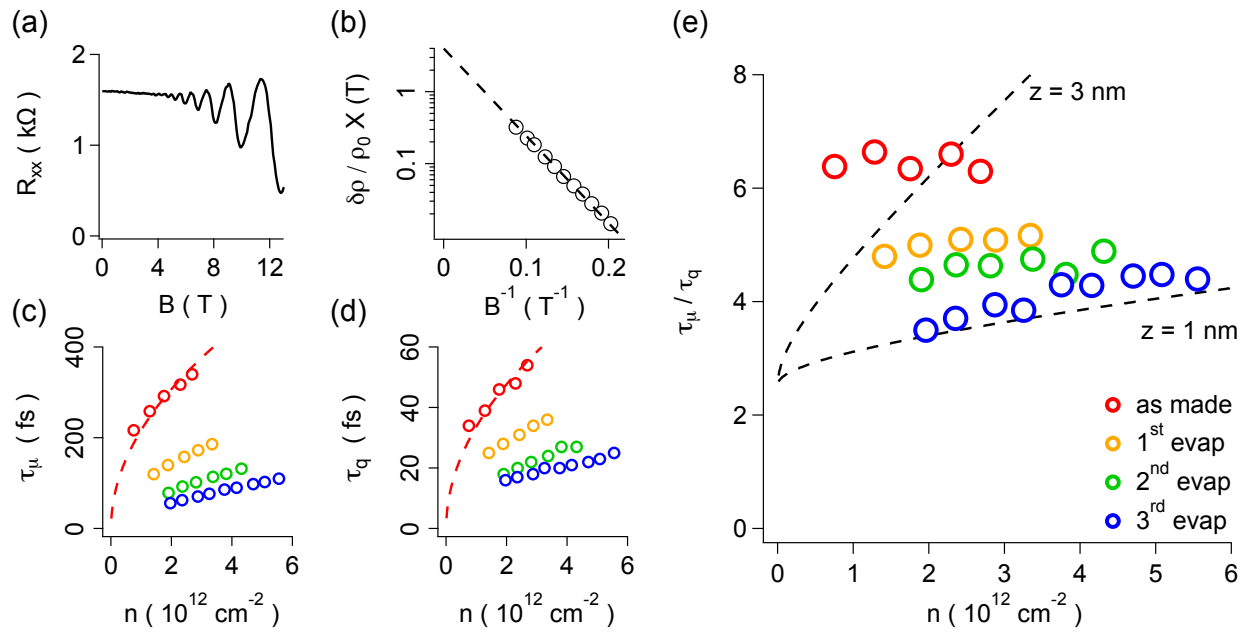

Figure 3.4: (a) Representative Shubnikov-de Haas trace after the second tungsten evaporation at constant density. (b) Temperature-corrected oscillation amplitudes versus B^{-1} with best fit line. (c),(d) Transport and quantum scattering times. (e) Ratio of transport to quantum scattering time, τ_μ/τ_q, versus carrier density, n. Uncertainty in the data is given by the symbol size. The dashed black lines are calculated using the theory of Hwang & das Sarma [109].

the scattering time ratio agrees with the value found from the zero-field conductivity analysis above, the initial separations prior to any tungsten deposition are in sharp disagreement. This may speak to our ignorance of the impurity distribution in the as-made sample, in which scattering sources other than charged impurities will play a larger role. For instance, we have not isolated the contribution of long- and short-ranged scattering in our analysis of the zero-field conductivity, as in all cases the charged impurity linear-in-n scattering dominates.

3.4.3 Results from a second sample

We have performed experiments similar to those in the main text on a second monolayer graphene sample. Although here the W wires were initially coated with a thin (~ 0.2 μm) layer of osmium, aggressive evaporation resulted in immediate deposition of the underlying W wire. We estimate the W density is $9 \pm 2 \times 10^{13}$ cm^{-2}, approximately $4 - 6$ times the osmium coverage. Despite the presumed mix of adatoms, the results are qualitatively similar to those in the main text: the conductivity curves are seen to shift leftward due to electron doping, with a concomitant decrease in mobility (or slope $\mathrm{d}\sigma/\mathrm{d}V_g$) (see Figure 3.5). The change in charge doping shows a steeper dependence on the inverse mobility. Additionally, the scattering time ratio τ_μ/τ_q is initially lower due to the different (and uncontrolled) initial impurity distribution (see Figure 3.6). The ratio *rises* slightly at higher densities with the first two evaporations, and finally falls again to a lower value in the range $2.5 - 3$. The rise in the ratio highlights how the two scattering times respond differently to the same impurity potential. Scattering time calculations produce the best agreement to this final curve assuming an adatom-graphene separation of 0.5 nm; smaller than the previous sample. It is possible that the quantitative differences in the transport shown here are due to the presence of osmium adatoms. Nonetheless, the behavior qualitatively mimics that occurring for a dilute coating of W adatoms alone. Weak localization data are not available for this sample.

3.4.4 Weak localization

Dephasing and intervalley scattering analysis

At magnetic fields below 50 mT, the first sample shows clear signs of weak localization in the magnetoresistance. Figure 3.7 shows four traces, plotted as $\delta\rho/\rho_0^2$ where $\delta\rho = \rho(B) - \rho(B = 0)$, for the as-made sample and following each evaporation at a carrier density of

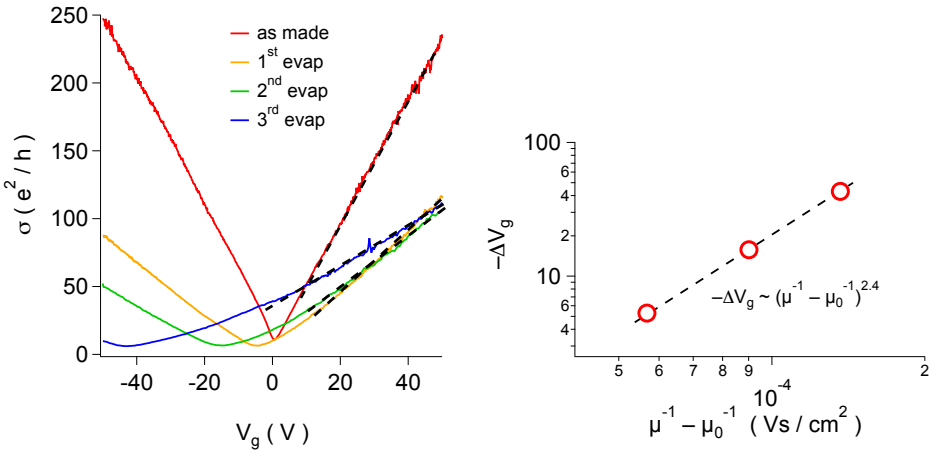

Figure 3.5: Left: conductivity, σ, vs gate voltage for sample 2, for the as-made sample and after each of three evaporations. Right: shift in gate voltage as a function of the change in inverse mobility.

$n = 1.4 \times 10^{12}$ cm^{-2}. All four traces show a narrow peak that is roughly e^2/h in magnitude, along with universal conductance fluctuations that are symmetric in the field. With each evaporation both the localization peak and the conductance fluctuation features are seen to broaden and become reduced in amplitude.

Analysis of the localization correction to the conductivity can yield useful information on characteristic scattering times including the phase coherence time τ_ϕ and various other scattering mechanisms [67]. In graphene these may include intervalley scattering rates, intravalley scattering processes including sublattice symmetry effects and trigonal warping of the Dirac cones, and spin-orbit effects [69, 72]. We perform fits to our data using a simplified version of the theory developed by McCann & Fal'ko *et al.* which ignores small corrections to the weak localization due to intravalley scattering processes [70]:

$$\frac{\Delta\rho}{\rho_0^2} = -\frac{e^2}{\pi h}\left[F\left(\frac{B}{B_\phi}\right) - F\left(\frac{B}{B_\phi + 2B_i}\right)\right], \tag{3.16}$$

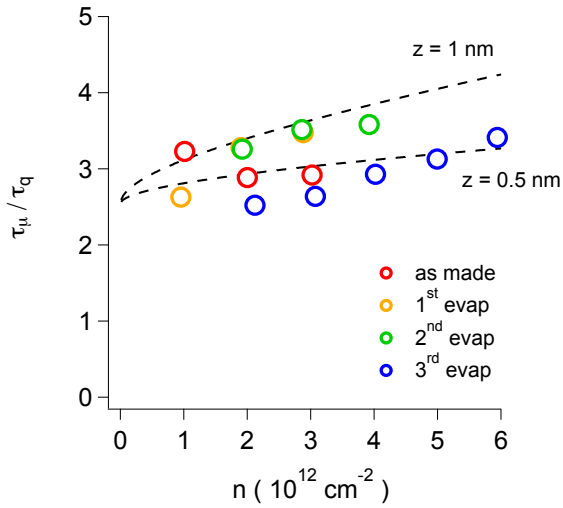

Figure 3.6: Scattering time ratio τ_μ/τ_q in a second sample. Here the ratio is initially lower, rises as the two scattering times vary with the addition of adatoms, and finally falls to a value lower than the sample in the main text.

$$F(z) = \ln(z) + \psi\left(\frac{1}{2} + \frac{1}{z}\right) \tag{3.17}$$

$$B_{\phi,i} = \frac{\hbar}{4De}\tau_{\phi,i}^{-1}. \tag{3.18}$$

Here $D = v_F^2\tau_\mu/2$ is the diffusivity and ψ is the digamma function. Use of this simplified theory is justified by the fact that graphene on SiO_2 devices have a high intravalley scattering rate that results in a negligible contribution to localization effects [70, 71, 115]. Indeed in comparing fits to our data made using either the simplified WL equation, Eq. 3.16, or the full WL equation, Eq. 3.23, from [69]. We find virtually no difference in the fitting curves. However, the inclusion of an additional fitting parameter for intravalley scattering in the full theory leads to χ^2 values that are poorly constrained and large uncertainties in the scattering times. Thus we obtain our numerical estimates of τ_ϕ and τ_i from fits using Eq. 3.16, applied over a magnetic field range such that the elastic mean free path is much

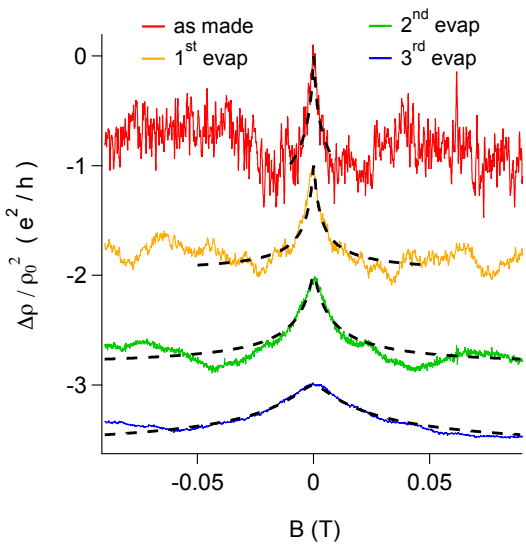

Figure 3.7: Low-field magnetoresistance for a carrier density $n = 1.4 \times 10^{12}$ cm^{-2}, showing characteristic weak localization peaks about $B = 0$. Traces are vertically offset for clarity. The dashed black lines are fits using Eq. 3.16, with the field range restricted to the diffusive regime $(l_\mu/l_B)^2 << 1$; the fitting parameters are plotted in Figure 3.8.

less than the magnetic length [116]

$$l_{el}^2 << l_B^2, \tag{3.19}$$

where

$$l_B = \sqrt{\hbar/eB}. \tag{3.20}$$

If we define the critical magnetic field as the field for which the elastic mean free path is less than the magnetic length, then we fit the data only within that field range [116]. This field is

$$B_c = \frac{4\pi|n|\hbar}{e\sigma^2} \times 10^4. \tag{3.21}$$

Figure 3.8 shows the results of our fitting procedure for values of the dephasing time τ_ϕ and the inter-valley scattering time τ_i. The differing density ranges used for the as-made

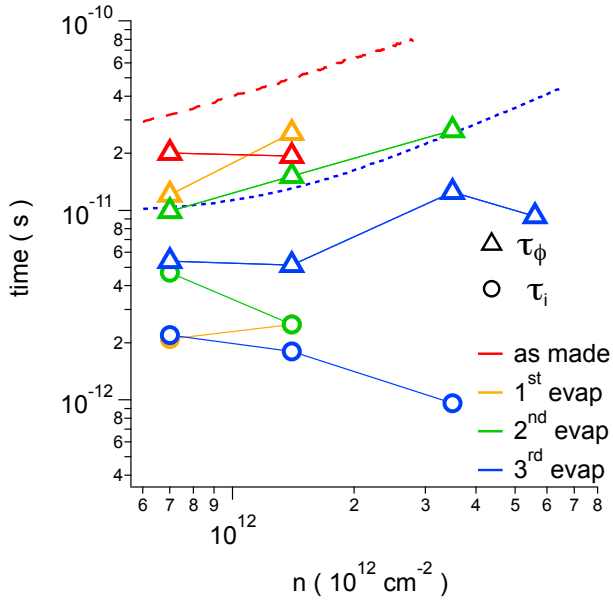

Figure 3.8: Phase-breaking time, τ_ϕ, and intervalley scattering time, τ_i, extracted from curve fits to the low-field magnetoresistance using Eq. 3.16, as illustrated in Figure 3.7. The theoretical phase breaking times calculated with Eq. 3.22 are shown as dashed lines in the upper portion of the figure, using data from the as-made sample (dashed red) and after the 3rd evaporation (dotted blue). Trends in the data reflect the increase (decrease) in conductivity with carrier density (successive evaporations).

sample and each separate evaporation are a consequence of the electron doping which, for the fixed gate voltage range employed, accesses an enlarged span of electron densities with each successive deposition. Not shown in Figure 3.8 is the distribution of transport scattering times, but even the largest τ_μ measured, occurring in the as-made sample at the highest explored carrier density, is only 0.3 ps so that in all cases τ_i exceeds τ_μ by at least one or two orders of magnitude. Roughly speaking, we find the dephasing times τ_ϕ show a modest increase with carrier density and a decrease with each tungsten deposition. Such behavior is in accordance with the predictions of Altshuler, Aronov and Khmel'nitski [117]

$$\tau_\phi^{-1} = \frac{k_B T}{2\hbar}\frac{\ln(\pi\hbar\nu D)}{\pi\hbar\nu D} = \frac{k_B T}{2\hbar}\frac{\ln(k_F l)}{k_F l}, \tag{3.22}$$

with D again the diffusivity and ν the density of states at the Fermi level. The expression on the right accounts for the single layer graphene density of states $\nu = 2E_F/(\pi\hbar^2 v_F^2)$. This formula is plotted in Figure 3.8 using the transport parameters for the as-made sample (red dashed line) and after the final tungsten evaporation (blue dotted line). The data clearly follow the general trend illustrated by these curves.

Meanwhile the inter-valley scattering times, although suffering from a fair degree of scatter, do tend to show a decrease with each evaporation. This is surprising: if tungsten adatoms act as charged impurities only intravalley scattering should increase, and an increase in τ_i would be expected due to the accompanying reduction in diffusivity. Moreover the intervalley times $\tau_i \approx 1-5$ ps correspond to a scattering lengths $l_i = \sqrt{D\tau_i} = 200-300$ nm, which is rather smaller than the 2 μm width of the device, although device edges are where the strongest intervalley scattering is expected. This may indicate that other sources for large-angle scattering are present in the device.

Search for spin-orbit coupling in weak localization magnetoresistance

Tungsten atoms have a strong inherent spin-orbit coupling which is predicted [52] to be inherited by graphene. Thus, we should study the low-field magnetoresistance with curve fits to the theory that incorporates the physics of spin-orbit scattering [72]. We have attempted this and find the fits from Eq. 3.23 to be generally inferior to those found using Eq. 3.16, as described below. Additionally, it is clear that no obvious signatures of Rashba spin-orbit coupling, i.e. weak anti-localization [72, 118], are observed. Altogether these findings suggest that any scattering due to an inherited spin-orbit interaction, if present at all, is weaker than intervalley scattering.

The data in Figure 3.9 show signatures of weak localization in the low-field magnetoresistance; Figure 3.9(a) and (b) reproduce the middle two traces of Figure 3.7, while Figure 3.9(c) and (d) show two additional traces at the highest adatom density. In all cases the

black dashed lines show fits performed using the simplified weak localization equation which yields characteristic times, τ_ϕ and τ_i, accounting for electron dephasing due to inelastic and intervalley scattering, respectively. Allowing for uncertainty due to the presence of universal conductance fluctuations, these fits closely match both the central peak, which is dominated by the phase breaking time, and the magnetoresistance at higher fields. For comparison, here we consider fits using an extension of the graphene WL theory that accounts for spin-orbit coupling effects [72], shown as solid lines in Figure 3.9, since tungsten adatoms may be expected to induce a spin-orbit coupling [52], and also both historically [118] and recently [35] the low-field magnetoresistance has been used to identify spin-orbit contributions to transport. This theory contains three fitting parameters that control electron dephasing, the phase-breaking time and two contributions from spin-orbit coupling τ_{sym} for mirror-symmetric couplings relative to the graphene plane (intrinsic) and τ_{asy} which breaks this symmetry (Rashba):

$$\frac{\Delta\rho}{\rho_0^2} = \frac{e^2}{2\pi h}\left[F\left(\frac{B}{B_\phi}\right) - F\left(\frac{B}{B_\phi + 2B_{asy}}\right) - 2F\left(\frac{B}{B_\phi + B_{asy} + B_{sym}}\right)\right], \tag{3.23}$$

where as before,

$$F(z) = \ln(z) + \psi\left(\frac{1}{2} + \frac{1}{z}\right), \tag{3.24}$$

and

$$B_j = \frac{\hbar}{4De}\tau_j^{-1}, \tag{3.25}$$

where the j index represents either ϕ, asy, or sym.

The asymmetric Rashba coupling can give rise to a weak *anti*-localization that has recently been seen in graphene on transition metal dichalcogenide substrates [35]. In the absence of spin-orbit couplings, Eq. 3.16 yields a weak localization magnetoresistance due to

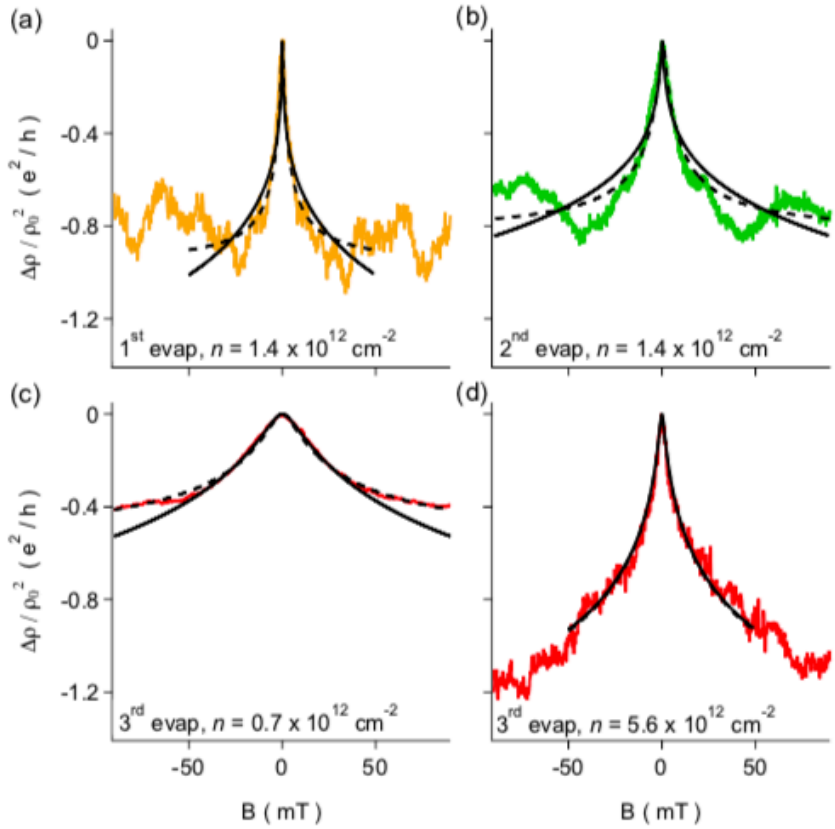

Figure 3.9: Comparison of fits to low-field magnetoresistance using either the standard weak localization theory [69] (dashed lines) or the theory including spin-orbit coupling [72] (solid lines). Top plots reproduce data and fits from Figure 3.7; bottom plots are additional traces at different densities after the last evaporation. The green and yellow traces, which are described earlier, are vertically offset as they otherwise perfectly obscure the black dashed line.

an assumption in its derivation that the intervalley scattering rate, τ_i^{-1}, exceeds the inelastic scattering rate, τ_ϕ^{-1}. A symmetric intrinsic SOC acts as an additional source of dephasing, resulting in a broader weak localization peak, while an asymmetric SOC will yield a weak anti-localization – a phenomenon not present in our data.

Despite this lack, we have attempted fits to our data using Eq. 3.23 and show typical results as the solid lines in Figure 3.9. Indeed we find these fits to be generally inferior to those that take account of variation in intervalley scattering. In particular, the SOC

fits can closely describe the central WL peak since the low-field region is dominated by τ_ϕ-dependence. However, they fail to match the magnetoresistance at higher fields that are still within the field range of validity for WL physics, a condition given by Eq. 3.21. Moreover, the extracted scattering times from the SOC fit do not satisfy $\tau_\phi > \tau_{asy,sym}$ that sets the applicable range of Eq. 3.16, nor can the effect of τ_{asy} be distinguished from τ_{sym}; for instance in Figure 3.9(c), the solid line results from $\tau_\phi = 9$ ps and either $\tau_{asy} = 100$ ps with $\tau_{sym} = 0$, or $\tau_{asy} = 0$ with $\tau_{sym} = 30$ ps. However the dashed line uniquely results from a fit performed with Eq. 3.16, yielding $\tau_\phi = 5.4$ ps and $\tau_i = 2.2$ ps. In Figure 3.9(d), the SOC WL fit (made using non-zero values of *either* τ_{sym} or τ_{asy}) almost perfectly overlies the fit accounting only for intervalley scattering.

In sum, we find that our weak localization data are not well accounted for by a WL theory that includes spin-orbit coupling effects.

3.5 Surface measurements

Measurements of the surface have been done in attempts to independently identify the concentration of adatoms on the graphene surface. In addition, surface measurements may clarify the distribution of adatoms and the presence of contaminants. Common methods used for such studies are: Auger, EDX, WDX, and XPS. These all are variant in both applicability and sensitivity.

3.5.1 Scanning Auger Electron Spectroscopy (SES)

One measurement we employed was Auger electron spectroscopy. Auger spectroscopy is a method in which the composition of the surface of a material is characterized by focusing a high energy monochromatic electron beam onto the surface and measuring the kinetic energy of low-energy Auger electrons that are emitted. Depending on the sample and equipment

used, this can result in sensitivities as high as 0.1 monolayers [119].

Results of our Auger measurements are shown in Figure 3.10. In part (a) of the figure, a comparative analysis of exfoliated graphene (unprocessed) and graphene that has been fabricated into a device (processed) is shown. Results indicate that the amounts of carbon, oxygen, and silicon may be highly variable. However, the general trend observed is correct: on the graphene location (all colored traces), the amount of carbon is higher than on a SiO_2 location (black trace) while the oxygen and silicon amounts are higher on the SiO_2 than on the graphene. In addition, a multiplex scan has been completed to confirm the presence of tungsten with the signal near gold energies used as a noise floor. This is shown in Figure 3.10(b). It is obvious that for both measurements, a tungsten peak is prevalent. While this peak is much smaller than the measured peaks for carbon, oxygen, and silicon, it is nonetheless not noise as can be seen by the lack of legible peak at the energy for gold. Indeed, this confirms that we do have tungsten, in extremely small amounts.

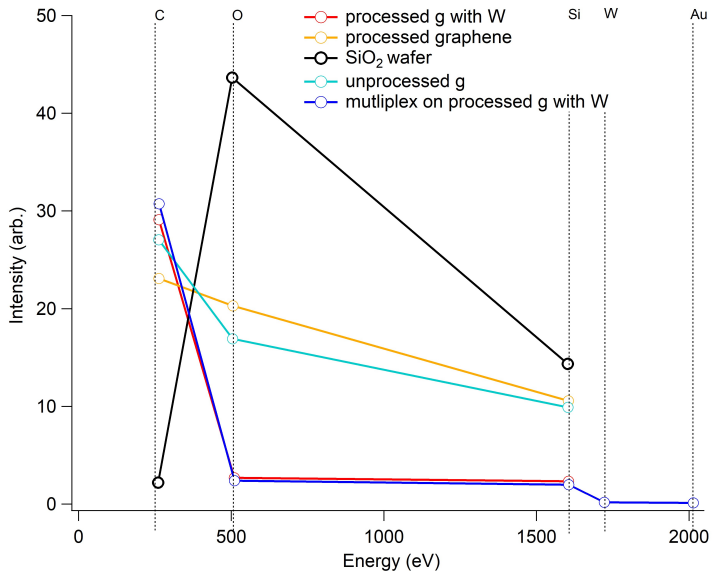

(a) Peak intensity

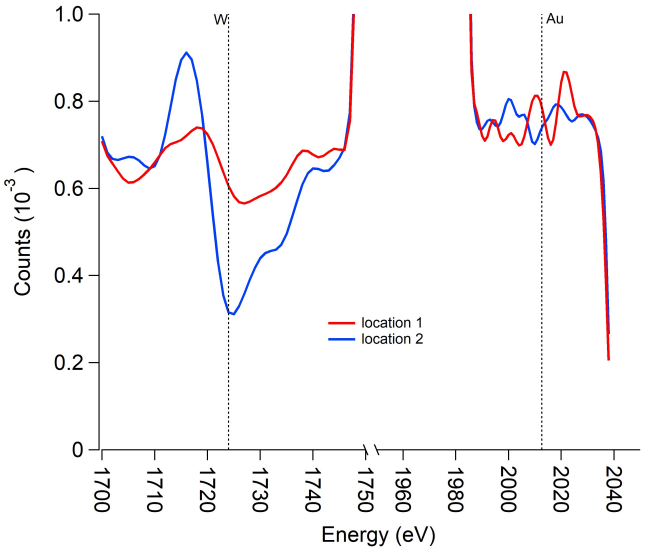

(b) High resolution W and Au scans

Figure 3.10: (a) Comparative results of Auger spectroscopy of processed and unproccessed graphene devices with (b) multiplex (high resolution) scanning for tungsten and gold signatures. Large variations in the amount of carbon, oxygen, and silicon are shown in both processed and unprocessed graphene.

3.5.2 Wavelength Dispersive X-ray Spectroscopy (WDX)

Another measurement we used to investigate the surface of the graphene after the experiment is Wavelength Dispersive X-ray Spectroscopy. In this method, an electron beam is focused on the desired sample and the detector counts the number of x-rays at specified wavelengths that are diffracted from the sample [120].

Our results for this analysis, shown in Figure 3.11, were only able to confirm the presence of tungsten on the surface of the graphene. In the top graph, the number of counts are shown for the wavelength corresponding to silicon, which are on the order of 250,000 counts. On the bottom, however, for the wavelength of tungsten, there are only around 145 counts. Indeed, the peak for tungsten is not much larger than the noise floor. This is not unexpected considering the usual resolution of WDX measurements.

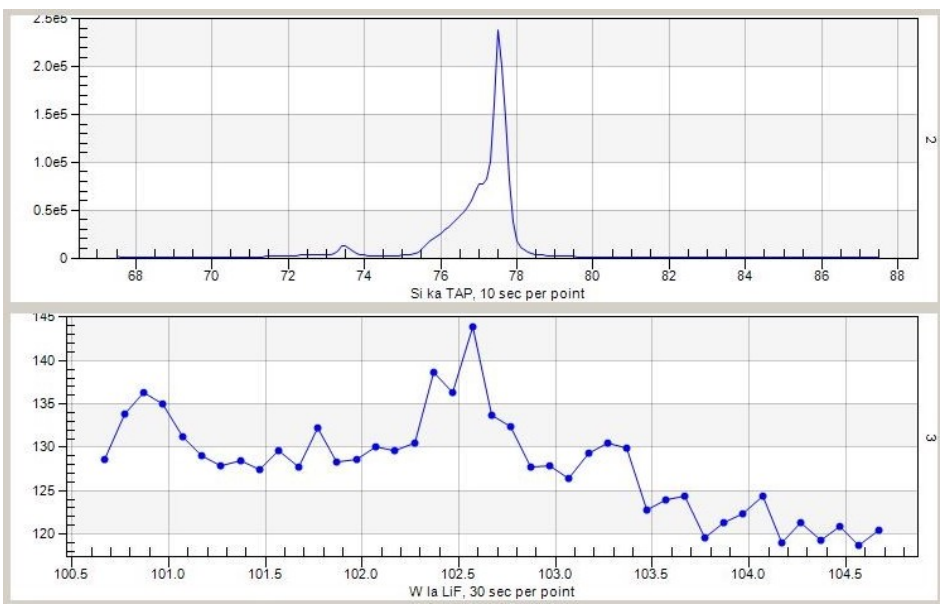

Figure 3.11: Number of counts made for silicon (top) and tungsten (bottom) showing a small noisy tungsten peak is present.

3.6 Discussion

In this work we present the results of electronic transport measurements on a sample of monolayer graphene with an increasing, but always small, density of tungsten adatoms. Measurements of the zero-field conductivity, the ratio of transport and quantum scattering times, and weak localization in the magnetoresistance point toward a now-familiar picture [7, 16, 17, 21–24] for metal adatoms wherein isolated impurities donate charge to the graphene substrate and become ionized impurities with a correlated increase in scattering and reduction of the mobility. However there is one standout feature in our experiment, namely as mentioned above we estimate that over 10 times as many tungsten atoms were deposited as can be accounted for by the magnitude of electron doping as measured by the shift in the minimum conductivity versus V_g, under the assumption that each atom donates one electron. Relaxing this assumption to within the range of theoretically-predicted values of $0.56 - 0.93$ electrons/atom [105, 106] does little to improve the match.

Regarding this discrepancy, two scenarios immediately suggest themselves: first, the adatoms may form clusters, or second, fabrication residues may prevent many atoms from reaching the surface. In the former case, we note the migration energy for W adatoms (the difference between binding energies at three high-symmetric sites: atop a C atom, astride a C-C bond, or in the middle of a hexagon) is calculated [105] by DFT to be $E_m = 1.2$ eV. The hopping rate for migrating adatoms is given by: [121]

$$\nu = \frac{k_B T}{h} e^{-eE_m/k_B T}, \tag{3.26}$$

where ν is the hopping rate, k_B is the Boltzmann constant, T is temperature, h is Planck's constant, and e is the electron charge. For all practical purposes, this vanishes below 150 K for tungsten atoms. For completeness, we note this strongly disagrees with a second DFT study [106] that finds the diffusion energy to be a mere 20 meV with the stable site to be

the C-C bond; clearly this would change our expectations.

In any event these considerations apply to atoms already on the surface, however adatoms with a high kinetic energy freshly evaporated from the ≈ 2800 K hot wire may diffuse on the graphene surface before losing their energy via thermal radiation or phonon emission, and thus have the opportunity to form clusters. Clusters of metal atoms on graphene are known to be far less efficient at charge doping [22, 24] and consequently have a limited impact on the mobility. However, the total charge-scattering cross-section in transport remains large for clusters and indeed a key prediction [111] of cluster-dominated transport is a ratio $\tau_\mu/\tau_q >> 1$, precisely the opposite of what we observe. Thus, we rule out clustering of tungsten adatoms on graphene.

So, we consider a second possibility: that fabrication residues prevent most of the evaporated atoms from reaching the surface. The surface of graphene after standard fabrication procedures employing PMMA as a resist for electron-beam lithography has been directly imaged by transmission electron microscopy [122, 123], and a thin ($\sim$ nm) coating of PMMA molecules is found to remain even after aggressive thermal annealing procedures, which were in any case not performed on our tungsten adatom devices. That work, [122, 123], reveals that a significant portion of the surface may be covered by this remnant PMMA, enough to perhaps account for the discrepancy between the expected density of tungsten atoms based on the change in the source wire diameter, and the maximum possible density assuming each atom donates one electron. This PMMA layer also provides a natural means to prevent clustering: if any hot tungsten atom does migrate upon landing, it will shortly encounter this impurity layer and come to a halt.

Finally, we note an induced spin-orbit coupling in graphene has been found by measuring so-called "non-local" voltages, by driving a current through one region of a graphene sample and finding a voltage drop far away where no appreciable current flow is expected in an ohmic material [26]. We have checked for such non-local voltages and find results consistent

with zero nonlocal voltage present.

3.7 Conclusions

In conclusion, we have performed a transport study of graphene with a dilute coating of tungsten adatoms. The adatoms induce an electron doping of the graphene and a reduction of the mobility, enforcing a linear dependence of the conductivity on density consistent with charged impurity scattering. Analysis of the changes in the conductivity suggest the tungsten atoms reside approximately 1 nm above the surface. Similar to the case of indium adatoms [17], this distance is unexpectedly large given that the atoms clearly are close enough to donate charge, and it also disagrees with the results of DFT calculations. One possibility is the height discussed in the self-consistent theory should be considered an "effective" distance that is correlated with, if not identical to, the actual physical separation that DFT attempts to calculate. We hypothesize that this may be in relation to the polymer residue likely coating much of the graphene device. This clearly requires further experimental investigation, preferably by a scanned probe method that is sensitive to the adatom height.

We have also performed a study of the ratio of the transport to quantum scattering time, τ_μ/τ_q, finding the ratio to decrease from $6-7$ down to $3-4$ as the density of tungsten adatoms increases. The adatom height inferred by comparison to theoretical calculations is approximately 1 nm, in agreement with the estimate found from the zero-field conductivity.

Clear signatures of weak localization are seen at low magnetic fields. The dephasing times extracted from fits are in agreement with values expected from theory. The intervalley scattering times are shorter than expected, but the precise scattering potential of the as-made device is not known and there may be defects or surface impurities that cause scattering with large momentum transfers. All transport data point to a picture wherein tungsten deposition at low coverages leads to isolated charged impurities. No evidence of spin-orbit coupling

transferred from the tungsten adatoms to the graphene is found. Overall, because of the residual polymer layer and discrepancies with DFT, it may be illuminating to repeat this process with devices that have been cleaned. However, based on the strikingly similar results from annealed devices with indium adatoms [17], the inheritance of a spin-orbit coupling may be more successful with AFM brooming rather than annealing.

3.8 Further Acknowledgements

We thank S. Adam, J. Alicea, U. Chandni, S. Das Sarma, M. Franz, M. Fuhrer, R. Mong, J. Pollanen, and M.-F. Tu for helpful correspondence and discussions.

Chapter 4

Effect of osmium adatoms on electronic transport of monolayer graphene devices

4.1 Abstract

Similar to the previous chapter, electronic transport of graphene is studied before and after osmium adatoms are evaporated *in situ*. A multitude of devices were studied, including those that were cleaned by basic solvent soak, shadow masked devices which require no cleaning due to their inherent polymer-free fabrication, and AFM broomed devices. The coatings of adatoms are randomly distributed and dilute. Interestingly, unlike all other metallic adatoms studied here and by other groups, osmium adatoms shift the charge neutrality point to the right in gate-voltage space. This indicates that osmium adatoms accept electrons from the graphene, thus hole doping the graphene. Similarly to tungsten, the addition of osmium to the surface of graphene causes a decrease in the mobility of the graphene, though to a lower extent; an estimated density of 4.5×10^{12} cm^{-2} osmium coverage causes a 34% decrease

in mobility versus an 85% decrease in the mobility for a 3.6×10^{12} cm^{-2} tungsten coverage. Measurements such as weak localization, Shubnikov de Haas, and nonlocal voltage measurements are examined for evidence of an inherited spin-orbit coupling or a transformation toward the quantum spin Hall insulator state. The current methods in use for analyzing weak localization with the intent to extract information about spin-orbit coupling, in particular the intrinsic-type coupling motivating this experiment, are not adequate for measurements where the inherent scattering potential also changes.

4.2 Introduction

4.2.1 Motivation

As in the previous chapter, we desire to boost the weak, native spin-orbit coupling of the electronic system of single layer graphene in order to realize the Kane-Mele Hamiltonian [48]. This extra term in the graphene Hamiltonian has been predicted to be useful for the engineering of topological materials such as the quantum spin Hall insulator [50, 51].

4.2.2 Device overview

As perhaps the most promising adatom for the creation of a graphene-based topological insulator [50, 51], many variations of this experiment have been performed. The first several devices were preliminary in nature, fabricated by standard lithographic methods and cleaned only by soaking in acetone. These are devices hereafter called "Preliminary": bz042215a, 081015b1, 061416a1, and 062415c3. Other measurements were made on devices fabricated by the shadow mask method; these are to be called "Shadow masks": 022017b3, 020817a2, and 011717d2. And finally, we studied two AFM broomed devices, hereby listed as "Broomed": 080317b2 and 092018a3. While the data presented below includes data and analyses of all

listed devices, we will summarize the data in three sections: preliminary devices, shadow masks, and broomed devices as suggested by the aforementioned naming scheme. More detailed discussion of the AFM cleaning procedure is discussed in Appendix B.

4.3 Experimental details

4.3.1 Dilution fridge methods

Electronic transport measurements were performed in a dilution fridge equipped with a superconducting 13.5 T magnet, using the same custom-built sample dipper shown in Chapter 3 with a ceramic stage shown in Figure 4.1(a) and a local thermal evaporator, Figure 4.1(b). Tungsten wires, 20 μm diameter, 99.95% purity, and annealed until smooth are suspended from these posts 4-8 cm below the sample for use as evaporation sources. Each tungsten wire is coated with a 1-3 μm layer of osmium and the evaporation rate is controlled by pushing a current through the wire while simultaneously monitoring changes occurring in the electronic transport.

During evaporation, the high wire temperature affects the surroundings such that the sample stage temperature approaches 40 K. The density of deposited atoms is estimated from changes to the graphene transport caused by charge doping and by measuring the change in diameter of the wire sources as was discussed in Chapter 3. Graphene devices are fabricated via mechanical exfoliation onto Si wafers with 300 nm thermal oxide, followed by fabrication of electrical contacts by three methods: electron beam lithography and thin film Cr/Au deposition, shadow-masking of Cr or Cr/Au contacts, and electron beam lithography and thermal evaporation followed by AFM brooming to clean the surface of residual PMMA. These processes are examined in detail in Appendix A and B.

(a) stage (b) evaporator

Figure 4.1: (a) The ceramic adatom stage mounted in a custom grounding chamber and (b) the thermal evaporator loaded with osmium coated tungsten wires.

Transport data is acquired before and after evaporation using low-frequency AC lock-in techniques. Applying a gate voltage to the substrate allows control of the carrier density in graphene, $n = \alpha(V_g - V_{g0})$, where the coefficient $\alpha = 7.0 \times 10^{10}$ cm^{-2}V^{-1}. Here we present results from several single layer graphene devices, some of which are etched by an O_2 plasma into Hall bars of various sizes.

4.3.2 Thermal evaporation of osmium adatoms

To evaporate osmium adatoms from the *in situ* thermal evaporator, we must obtain osmium coatings. The tungsten wires as provided by California Fine Wire Company, Figure 4.2(a), are about 20 μm in diameter and show striations in the surface. In order to adequately estimate the amount of osmium on a wire, we must, with reasonable accuracy, be able to measure the diameter of the wires. For this reason, the tungsten wires are annealed at 200 mA for 3 minutes while under vacuum, approximately 2 μTorr. This significantly smooths the surface of the wire, Figure 4.2(b). The wires are then mounted to a square Teflon ring

and plasma coated with a layer of osmium, courtesy of Jeff Hall at Structure Probe, Inc. We use scanning electron microscopy to measure the diameter of the wires before and after the osmium plasma deposition. An example wire after the Os coating has been applied is shown in Figure 4.2(c). During such measurements it became obvious, as seen in Figure 4.2(d), that the osmium coating is not well adhered to the tungsten surface and may be flaking off the wire in areas. If these wires are dropped or otherwise mishandled when loading them into the evaporator, then it is possible that they will have lost some of their osmium coating. This increases the potential error on our geometric calculation of the coverage percentage. In addition, it is possible that during loading, the tweezers used to load the osmium wires could also cause disrepair in the wires such as is shown in Figure 4.2(d) or worse.

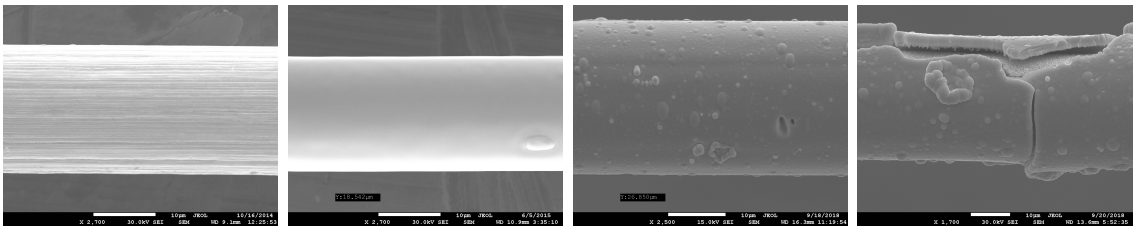

(a) tungsten wire (b) annealed wire (c) osmium coated wire (d) flaking osmium

Figure 4.2: Scanning electron microscopy of tungsten wires (a) as purchased, (b) after a smoothing anneal, and (c)-(d) with osmium coating

4.3.3 Devices measured

Preliminary devices

Preliminary graphene devices studied include graphene with Cr/Au contacts made via electron beam lithography and thermal evaporation. Polymer is removed from the devices by an acetone soak. According to [123] and our previous experience with tungsten adatoms, we know that some PMMA has been left on the graphene surface. This residue likely limits

the ability of the graphene to inherit spin-orbit coupling from the adatoms. In addition, it is likely to decrease the initial mobility, increase the amount of scattering due to impurities on the surface, and decrease the ability of the adatoms to diffuse or cluster on the graphene surface. The devices measured are shown in Figure 4.3; a graphene on hexagonal boron nitride (hBN) device, which was fabricated by Boyi Zhou, and three graphene on SiO_2 which were fabricated by the author. In the case of the graphene on boron nitride device, the three contacts nearest the top-left of the photo are disconnected from the rest of the device by a crack in the graphene. Another crack became apparent during measurement that also separated the five contacts nearest the bottom-right from the other two in the larger graphene piece. This became obvious by the inability of the left contacts (of the seven contact set on the larger graphene piece) to carry a current to the contacts to their right. Post-experiment SEM images confirm both splits in the graphene and are shown in Figure 4.4.

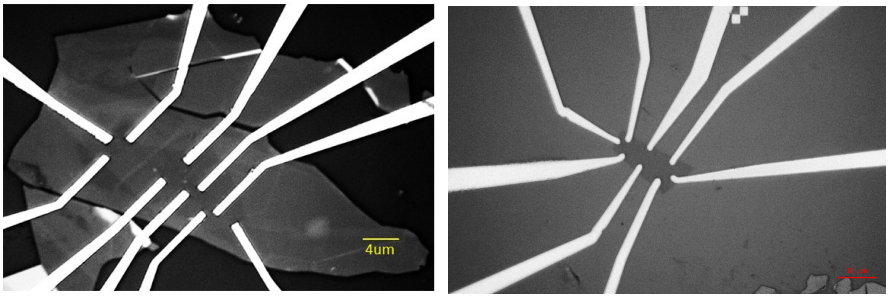

(a) bz042215a

(b) 081015b1

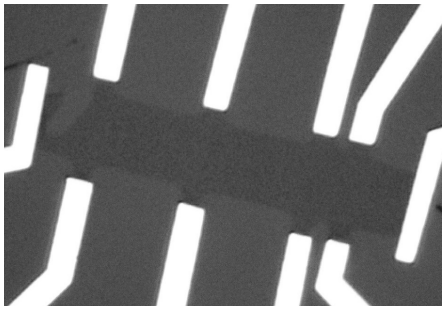

(c) 061416a1

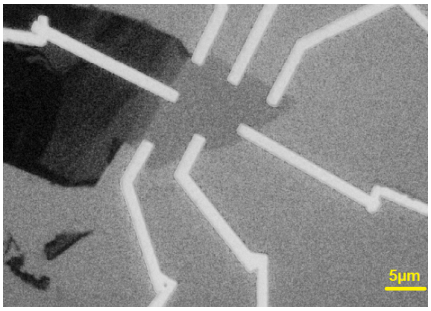

(d) 062415c3

Figure 4.3: Optical microscope images of preliminary graphene devices, magnification x100

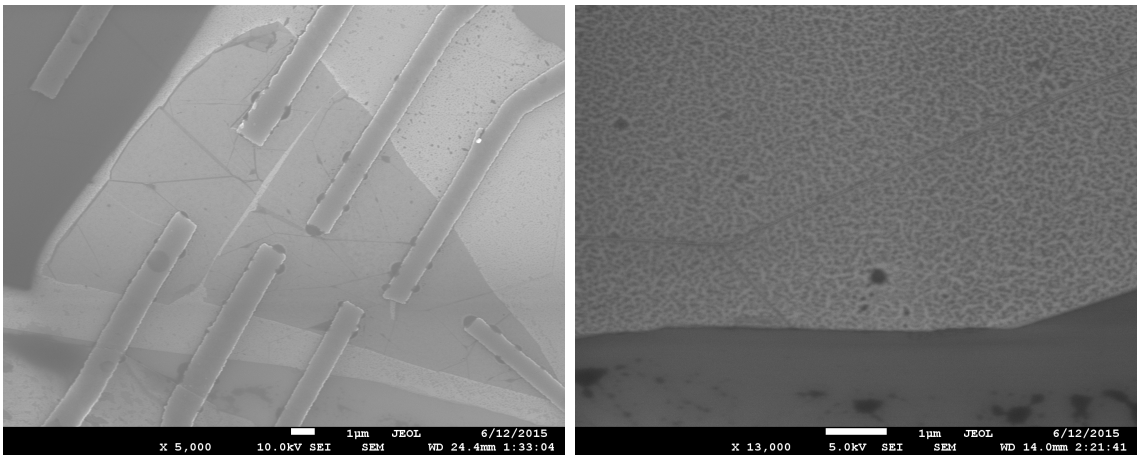

(a) contact configuration and graphene cracks (b) surface morphology

Figure 4.4: Scanning electron microscope images of bz042215a after osmium deposition and post evaporation measurements

An important quality to note of this preliminary batch is that the devices are varied in size, shape, and substrate. One of the devices was etched to a Hall bar shape, others were not. The first has a hBN substrate, while the others were fabricated on SiO_2. The results obtained for such devices are different than for similar devices with tungsten adatoms but generally consistent with all other osmium-decorated graphene devices. In addition, some of these devices were used for tuning of the evaporation current and include both osmium and tungsten adatoms. All reported data with both adatoms will be labeled as such to avoid confusion.

Shadow-masked devices

After our preliminary work with osmium and tungsten adatoms, it became clear that we were not inducing any significant spin-orbit coupling to the graphene. In addition, tungsten adatoms were not settling as close to the surface as predicted by density functional theory [104]. Indeed, it has been discovered that simple solvent soaks like acetone used for metal

contact liftoff procedures leaves significant (a nm) PMMA residue behind on the graphene. This polymer layer may be removed by annealing procedures but the level of aggression required also damages the graphene [123]. Instead, we chose to fabricate graphene devices without PMMA or other polymers coming into contact. This required quite a few engineering adaptations to our device fabrication process; these are also described in Appendix A.

The shadow masks discussed in this chapter are shown in Figure 4.5; due to the level of difficulty in the fabrication of these devices, we only have data from 2-contact shadow masks. For two of these devices, a thicker chromium layer was used for the shadow-masked contacts. It is obvious in the optical images that there is some tension in the thin metallic film evaporated as contacts to the graphene. While the metal seems to be peeling wherever it is in contact with the graphene, the contact resistances were low enough to make measurements.

(a) 022017b3 (b) 020817a2 (c) 011717d2

Figure 4.5: Shadow masked devices measured with osmium adatoms

AFM nano-broomed devices

Finally, we report the results of graphene fabricated by standard lithographic methods and cleaned via AFM brooming. For detailed discussions of this method and it's efficiency in cleaning graphene surfaces, please see Appendices A and B, respectively.

Two independent graphene on SiO_2 devices were measured for this section: a 5μm x 15μm un-etched flake with a small graphite piece far from the measurement region, Figure 4.6(a), and two devices fabricated side-by-side out of the same graphene flake, one being a large-scale hall bar for good weak localization averaging, Figure 4.6(b), and the other being a small hall bar, Figure 4.6(c), designed with a narrow, about 250 nm, central region and small distance between the contacts, 500 nm - 1 μm. The latter two devices are labeled SHB (small hall bar) and LHB (large hall bar) respectively. Unfortunately, the LHB only had three good contacts available after brooming so the measurements taken for that device are limited.

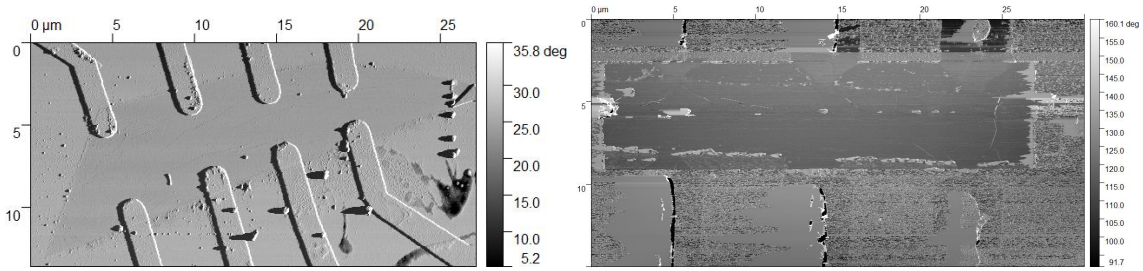

(a) 080317b2

(b) 092018a3 LHB

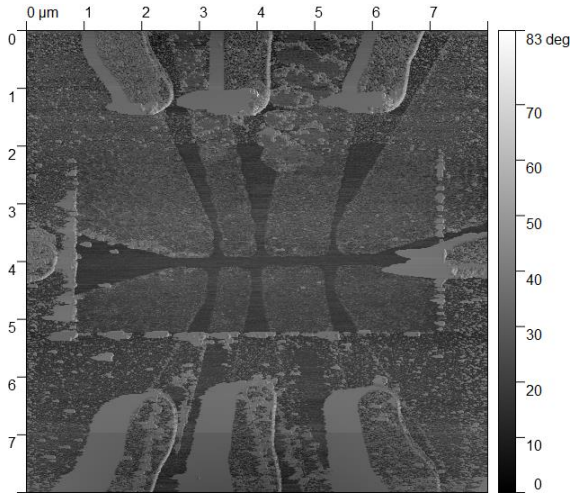

(c) 092018a3 SHB

Figure 4.6: AFM phase images of devices 080317b2, 092018a3 LHB, and 092018a3 SHB after brooming.

4.4 Results

4.4.1 Zero-field electronic transport

Preliminary devices

The basic electronic transport of graphene with osmium adatoms is entirely different from graphene with tungsten. This shown by the change in the direction of the Dirac peak

movement. For the as-made (pre-evaporation) devices, the Dirac peak is around gate voltage 0 V. As osmium is added, the Dirac peak shifts to the right (rather than left for tungsten and other metals). This first result is remarkable; all other metallic adatoms that have been measured on graphene electron dope the graphene [7, 16–25]! This includes: Au, Ca, Fe, In, Ir, K, Li, Mg, Pt, and Ti. This result is consistent across all preliminary devices as well as across shadow-masked and AFM broomed devices.

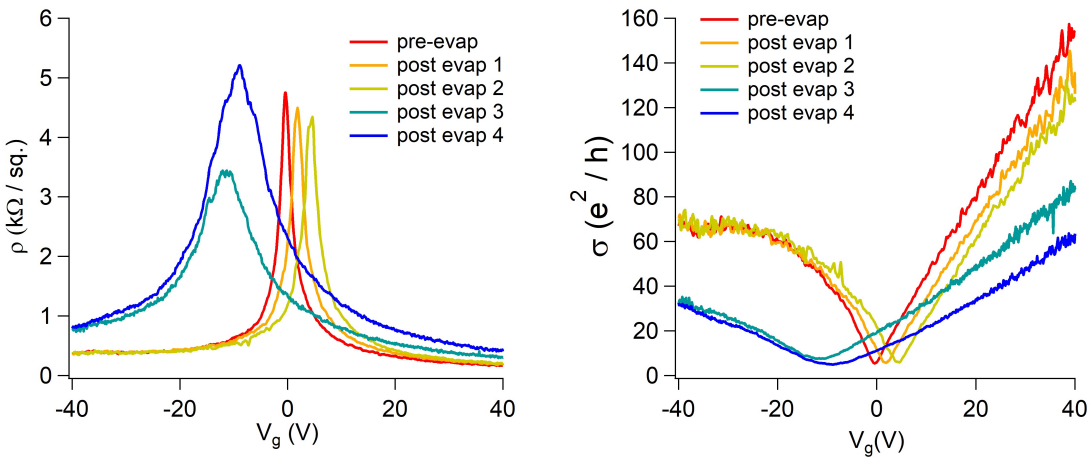

(a) Resistivity

(b) Conductivity

Figure 4.7: (a) The resistivity versus gate voltage of graphene without adatoms in red, after each of two sequential osmium adatoms in orange and yellow, after a tungsten evaporation in teal, and after an osmium evaporation in blue. (b) The conductivity versus gate voltage of the same device and experimental steps.

In Figure 4.7, the resistivity and conductivity of device bz042215a is reported. The first two evaporations were of osmium. During the third osmium evaporation, the osmium source wire broke, depositing tungsten and rapidly dropping the current through the wire to 0 mA which allowed the graphene to cool to 4 K. We measured the "post-evap 3" (teal) data after this and saw a large shift of the Dirac peak to the left and a very obvious decrease in the mobility shown by the change in the width of the Dirac peak. There are several possible

reasons that could explain the source wire breaking during evaporation. Perhaps there was a point along the wire that had been pinched or bent during loading of the wires to the thermal evaporator. A constriction such as this may cause a hot spot (place where the temperature is significantly hotter than elsewhere) on the wire. Furthermore, some impurity or defect in the purchased and coated wire could also cause a hot spot. This hot spot would evaporate material faster and decrease the diameter of the wire nearby more quickly than elsewhere along the wire, which could result in a mechanically weaker location on the wire that is likely to break. After evaporation 3, a new source wire was chosen for evaporation 4. This wire did not break and only osmium was evaporated.

In addition to the remarkable hole doping, the presence of osmium adatoms decreases the mobility of the graphene. However, the effect is less severe than for tungsten adatoms. This can be seen by the width of the Dirac peak on the resistivity versus gate voltage plot in Figure 4.7(a). After the first and second evaporations, which we know are osmium adatoms because of the hole doping, the width of the Dirac peak changes negligibly. When the wire breaks and tungsten adatoms are deposited, however, the width of the Dirac peak is increased by a factor of 3 or 4. This corresponds to a percent decrease in the mobility of about 59% (from about 15000 cm^2/Vs to about 6200 cm^2/Vs). While this difference may be partially due to the amount of adatoms deposited from the broken tungsten in comparison to the thin osmium layer, it seems unlikely that this is the only reason why tungsten decreased the mobility so drastically in comparison to osmium on this device.

Shadow masks

Shadow mask devices are inherently different from the standard graphene devices fabricated by electron beam lithography. Indeed, our transport for these devices, shown in Figure 4.8, displays a surprisingly low mobility and a Dirac peak farther to the right of gate voltage 0 V. Of course, because these are all 2-wire measurements, there is some contact resistance

that is included in these measurements.

Nonetheless, in the transport of these devices we continue to observe that the osmium hole dopes the graphene, as evidenced by both the resistivity peak and the conductivity minima shifting to the right, as in Figure 4.8(a) and (b). In addition, the osmium affects the mobility of the device. In the transport of device 022017b3, shown in Figure 4.8, the resistivity is found by approximating the contact resistance to be 1700 Ω and using the geometry of the device to approximate the number of squares between measurement contacts (1.58 squares). The pre-evaporation mobility is found to be 1900 cm^2/Vs for device 022017b3. This initial value is surprisingly low considering the polymer-free fabrication process used! After a single osmium evaporation, the mobility decreases to about 400 cm^2/Vs. Surprisingly, the mobility actually increases to about 1000 cm^2/Vs after the second osmium evaporation. Similar behavior was seen in the other two devices, except that the second evaporation seemingly did not affect transport at all in the other devices, perhaps due to the osmium source layer having been fully evaporated previously.

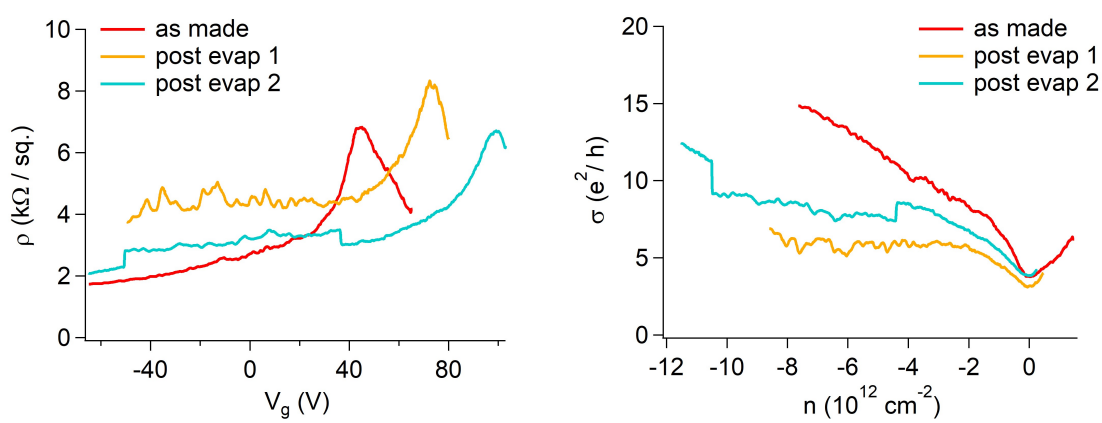

(a) resistivity

(b) conductivity

Figure 4.8: Transport of shadow masked device 022017b3 before approximating contact resistance.

AFM nano-broomed devices

For broomed devices, the transport behavior is similar to preliminary and shadow-masked devices. As seen in Figure 4.9, osmium is shown to hole dope the graphene, moving the Dirac peak to the right in gate voltage, Figure 4.9(a), and shifting the conductivity minimum to the right, Figure 4.9(b). Furthermore, the mobility initially decreases when osmium is added but remains nearly constant with sequential evaporations. In addition to evaporations, for these devices, the sample stage was heated *in situ* to room temperature. It is expected that when heating the stage, the ability of the osmium adatoms to diffuse around the surface is increased. This could mean either they are removed from the surface or that they collide and form clusters on the surface or that they fall into local energy minima that were not accessible during the initial deposition because the low temperature of the graphene inhibited adatom diffusion across the surface.

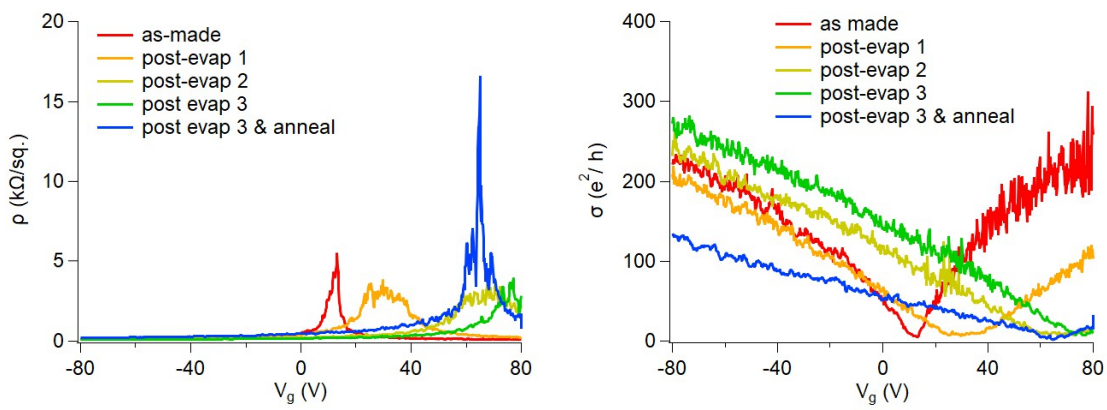

(a) resistivity (b) conductivity

Figure 4.9: Transport of broomed device 092018a3 for the as-made device, after each of three evaporations, and after a final anneal

Similar to Chapter 3, we also studied the relationship between the change in the mobility and the change in the gate voltage location of the Dirac peak. For the broomed devices, this

data is so far inconclusive. For example, in Figure 4.10(a), we plot the evaporation steps in red and the anneal steps in blue. The purple lines connect steps in chronological order. For this graph, all mobilities were calculated using: $\mu = \frac{1}{ne\rho}$ at constant carrier density $n = -5.45x10^{12}\ cm^{-2}$. The slope of the fitted line is equivalent to the exponent b in the equation $\Delta V_g = c_1(\frac{1}{\mu} - \frac{1}{\mu_0})^b$. Thus, for device 092018a3, this exponent is highly dependent on the method used to obtain the mobility. In addition, device 080317b2 had fewer data points and a significantly smaller exponent.

These calculated exponents are listed in Table 1 for the corresponding device and method used for calculating the mobility. From this, and then Figure 4.11, it is obvious that the only conclusion we can make is that *maybe* the value for this exponent could be near 1 for osmium-decorated, broomed graphene. Overall, it is difficult to draw strong conclusions from this data.

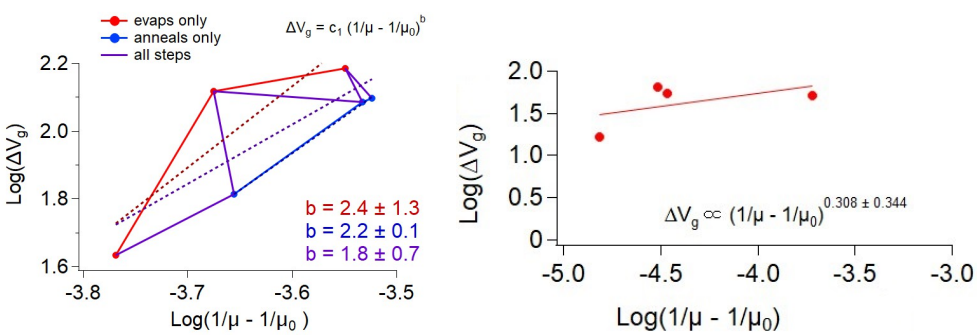

(a) 080317b2

(b) 092018a3 SHB

Figure 4.10: The power law for mobility and gate voltage changes of graphene decorated by osmium adatoms is not sufficient to describe osmium interactions with graphene.

Device	Method for Calculating μ	b
092018a3 SHB	slope of σ	0.308 ± 0.344
080317b2	average μ	1.16 ± 0.29
080317b2	μ at lowest n	0.80 ± 0.32
080317b2	μ at $n = -5.45x10^{12}cm^{-2}$	2.40 ± 1.3
080317b2	average μ consistent n range	1.81 ± 0.66

Table 4.1: Exponent b given by various methods and in multiple devices are not consistent.

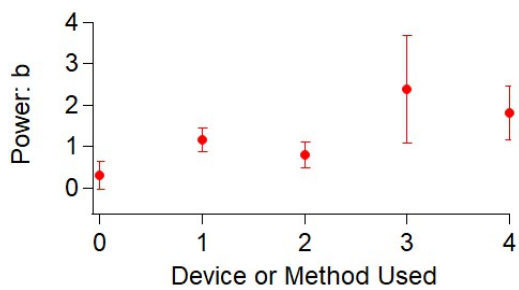

Figure 4.11: Range of exponents, b, for broomed graphene with osmium

For the first broomed device, the osmium adatom density calculated by assuming one hole donated by each adatom is 1×10^{13} cm^{-2}. For the second device set, the adatom density calculated in this way is 4.5×10^{12} cm^{-2}. This is quite surprising since the osmium coated wires for the second broomed data set began with approximately a coating thrice as thick as previous source wires. However, when analyzing the osmium wire surfaces after evaporation, it become clear that the new, thicker layer of osmium evaporated much less uniformly than in previous source batches. Indeed, in most images, the wires appeared as if the osmium layer was loosely attached to and flaking off the tungsten wire. These wire images are shown in Figure 4.2(c)-(d) and Figure 4.12. For this reason, adatom densities calculated by a geometric estimation of the change in the osmium source wire radius are not

adequate for the second broomed device set.

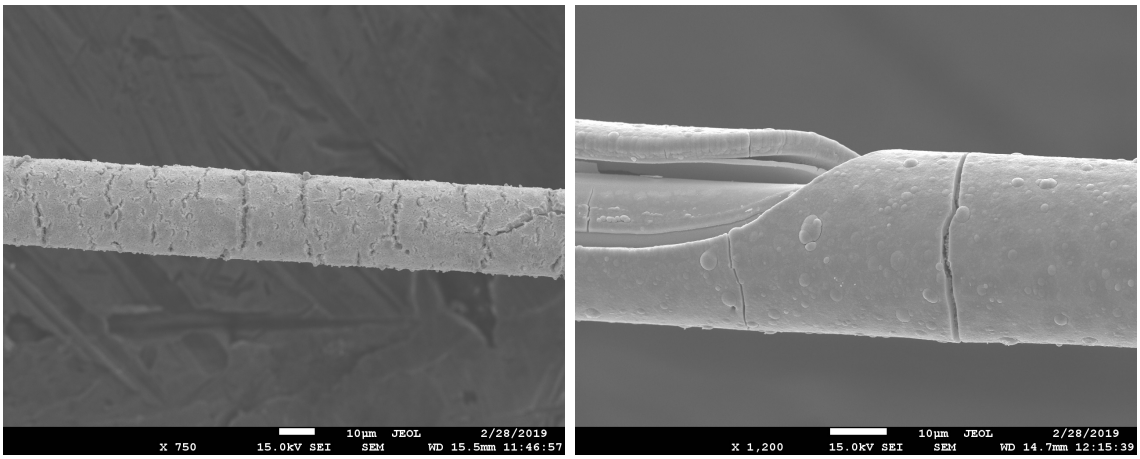

(a) (b)

Figure 4.12: Osmium wires used for the second set of broomed devices showed extensive flaking. It seems the osmium was grown onto the tungsten surface in layers and during the evaporation, these layers were not uniformly hot due to bad thermal contact.

4.4.2 High-field quantum Hall effect

Preliminary devices

We have also measured the quantum Hall effect in preliminary graphene devices before and after evaporations of osmium adatoms. This is accomplished by ranging the magnetic field slowly while the gate voltage is more quickly ranged. While the magnetic field and gate voltage are changing, the longitudinal and transverse voltages of the graphene are measured. Typical graphene behavior shows the Dirac peak at zero-field and oscillations in the resistance as the field increases at constant gate voltage. This behavior results in a fan-like diagram, often called Landau fan diagrams. For preliminary devices, the as-made graphene quantum Hall diagram, shown in Figure 4.13(a), is broadened after osmium is added and shifts to the right, reflecting the hole-doping, shown in Figure 4.13(b)-(c).

If we take constant gate voltage line cuts of this data, we can extract Shubnikov de Haas oscillations as well. The amplitude of Shubnikov-de Haas oscillations is generally well-described by the first term of the Lifshitz-Kosevich equation [112],

$$\frac{\delta\rho_{xx}}{\rho_0} = 4\ X_{th}\ e^{-\pi/\omega_c\tau_q}, \tag{4.1}$$

with the thermal factor

$$X_{th} = \frac{2\pi^2 k_B T/\hbar\omega_c}{\sinh(2\pi^2 k_B T/\hbar\omega_c)} \tag{4.2}$$

and where $\rho_0 = \rho(B = 0)$, and the cyclotron frequency, $\omega_c = eB/m^*$, with the effective mass, $m^* = \hbar\sqrt{\pi n}/v_F$.

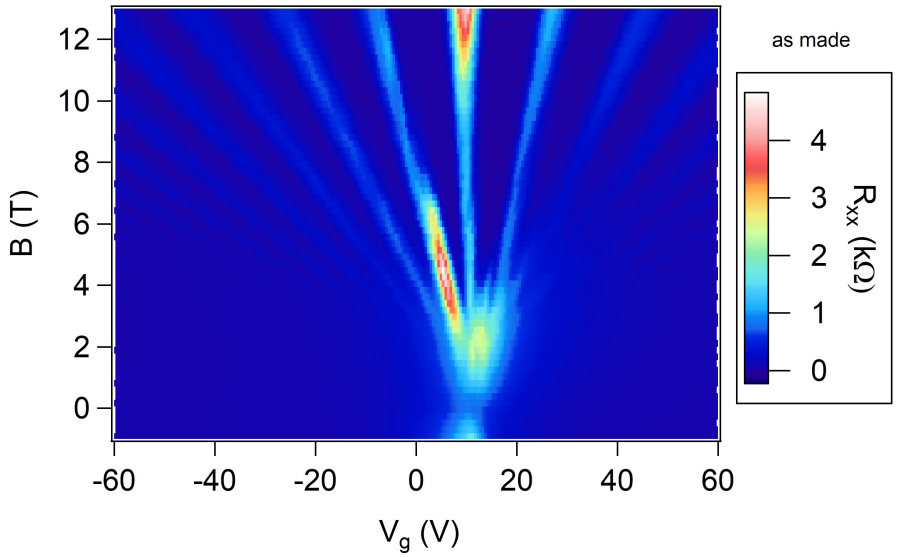

(a) as made

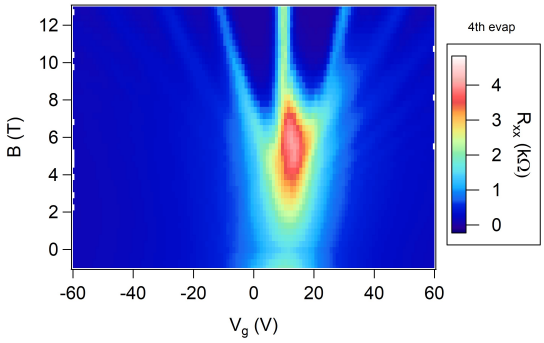

(b) post evap 4

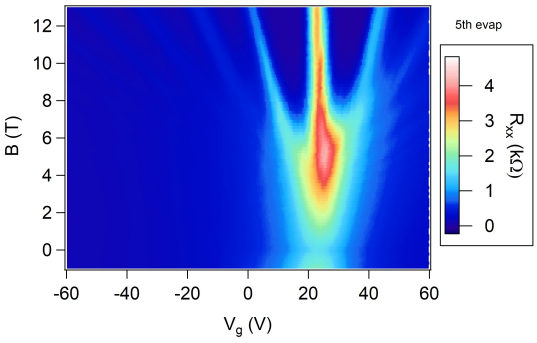

(c) post evap 5

Figure 4.13: Quantum Hall effect measurement of device 061416a1: (a) as-made, (b) post evaporation 4, (c) post evaporation 5

We use the Shubnikov de Haas oscillations to calculate the quantum scattering time, τ_q. Because τ_q is sensitive to all scattering events and τ_μ is only sensitive to scattering events that increase the resistance, the ratio τ_μ/τ_q can be used to discriminate between the types and locations of dominant scattering potentials. In particular, the ratio is expected to be

less than 2 for short-range scattering, greater than 2 for Coulomb scattering in the graphene plane, and greater still when Coulomb scatterers are above the plane. Furthermore, a very large ratio might indicate clustering of the adatoms.

In our Shubnikov de Haas oscillations, the best available data was acquired after the first and third evaporations, for two carrier densities of device 062415c3. At other densities and evaporation steps, the quantization and oscillations are washed out. The scattering time ratios τ_μ/τ_q are shown in Figure 4.14.

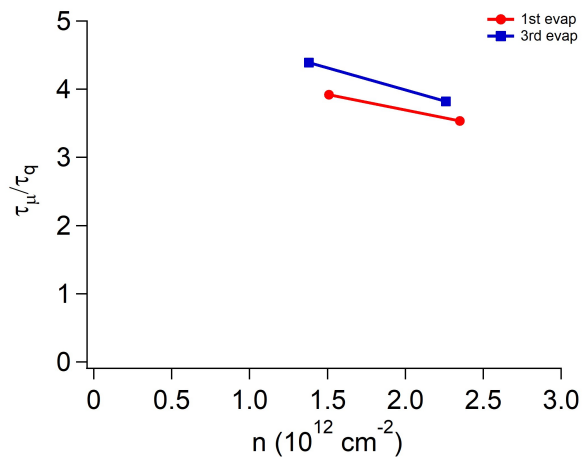

(a) τ ratio

Figure 4.14: The ratio τ_μ/τ_q versus carrier density for the first and third evaporations of preliminary device 062415c3

Albeit from a small data set, the ratio increases as osmium is added. In comparison to tungsten adatoms on graphene devices, we saw the opposite trend. It is possible that because very few data points were taken, that this trend will not be reproducible in more thorough investigations.

Furthermore, if osmium adatoms were inducing spin-orbit coupling to graphene of the asymmetric (Rashba) type, then we may expect a beating pattern in the Shubnikov de Haas oscillations [34, 35]. For this device, no resonance beating pattern was seen in the Shubnikov

de Haas oscillations. This provides initial evidence that we do not see any Rashba spin-orbit coupling present in the measured preliminary devices.

Shadow-masked devices

For one shadow-masked device, 020817a2, we obtained a quantum Hall color map. From this image, shown in Figure 4.15, it is obvious that the low mobility and high disorder in the device causes a smearing out of the typical high mobility Landau fan of graphene.

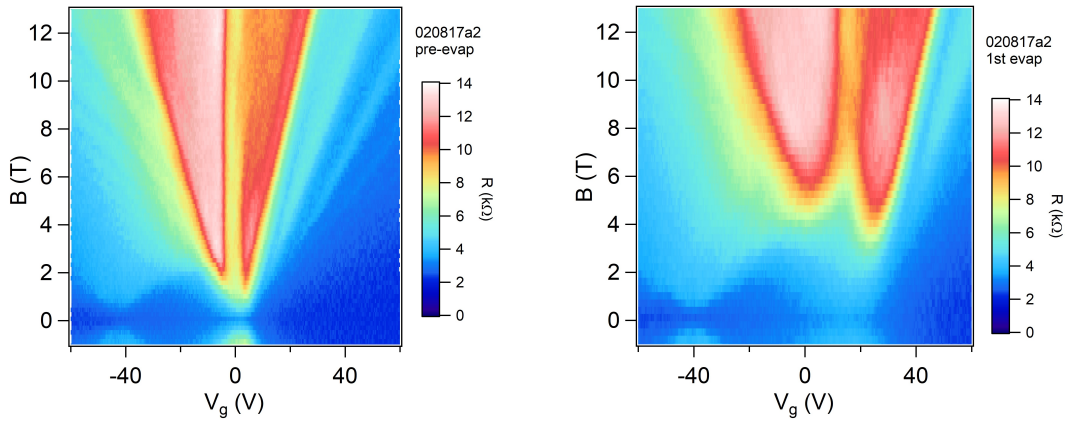

(a) as made

(b) post evap 1

Figure 4.15: Quantum Hall color maps of an as-made and post-evaporation shadow mask. The mobility is low enough to destroy the high field quantization of graphene.

High field Shubnikov de Haas measurements for these devices were neither clear nor useful and thus are not reported.

AFM nano-broomed devices

Broomed devices were also measured under high magnetic field. Example quantum Hall color maps are shown in Figure 4.16 for before and after osmium evaporations of device 080317b2. While the Landau fan does move to the right due to the hole doping and become

washed out towards larger gate voltages, the fan is still visible for all steps. The other broomed devices behaved similarly. This suggests that as osmium is added, the scattering in the device is increased and fewer electrons are capable of completing cyclotron orbitals before scattering, inhibiting quantization.

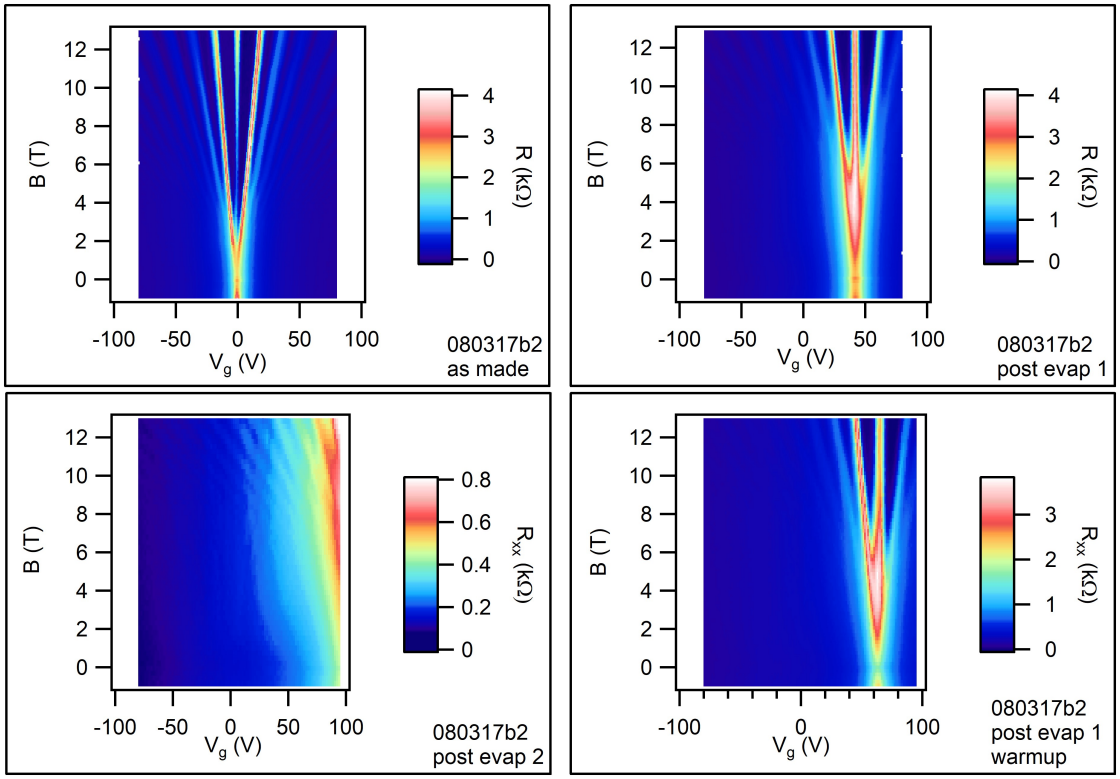

Figure 4.16: Quantum Hall effect of broomed devices

Only broomed device 080317b2 was of high enough mobility and low enough noise to reasonably measure Shubnikov de Haas oscillations. The amplitude of the oscillations was studied in relation to the magnetic field and carrier density at which the oscillations occurred. This allows us to extract the quantum scattering time. The quantum scattering time and the ratio of the quantum scattering time to the mobility scattering time are shown in Figure 4.17. These tell us something of the scattering potential present in the graphene at the given steps [109]. Unfortunately, the data shown in Figure 4.17 suggests that this simple model of

either Coulomb impurity scattering or short-range scattering is not adequate for graphene with osmium adatoms. Our broomed device in the as-made state was of the correct order and approximate shape for Coulomb impurity scattering with an effective height 1 nm above the graphene plane, the yellow dotted line in Figure 4.17(b), while the particular details were incorrect. However, after adding osmium to the graphene, the general trend nor the particular values adhere to this model. Indeed variations with larger effective distances are similar in shape with a more dramatic increase with carrier density.

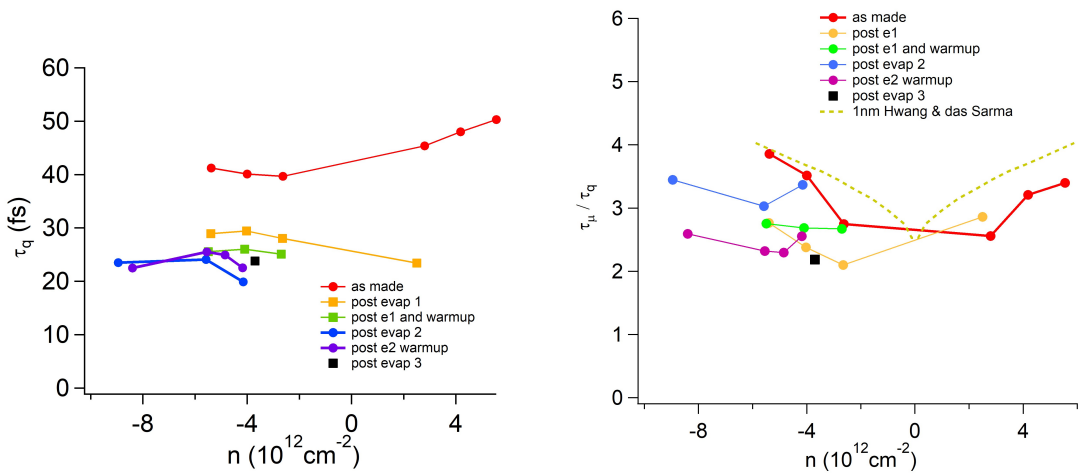

(a) τ_q

(b) τ_μ/τ_q

Figure 4.17: Quantum scattering time and the ratio of the mobility scattering times to the quantum scattering time

4.4.3 Low-field weak localization

Preliminary devices

As discussed in Chapter 2, weak localization, the quantum correction to the resistance due to interference of self-intersecting electron paths, is another measurement that could indicate whether or not graphene has inherited some spin-orbit coupling by proximity to a spin-orbit

material. If the weak localization shows a transition toward weak antilocalization, then a Rashba-type (asymmetric) spin-orbit coupling has been induced by the adatoms. Otherwise, an intrinsic (symmetric) spin-orbit coupling results in a weak localization with saturation in the size of the conductivity correction as the temperature approaches zero [72]. We measure the low field magnetoresistance and look for changes in the peak amplitude and breadth at constant carrier density, that is, constant gate voltage. These gate voltages are chosen such that $dV = V_g - V_{g,0}$ is consistent between as-made and post-evaporation measurements, where $V_{g,0}$ is the gate voltage of the Dirac peak. Many of these measurements exhibit large universal conductance fluctuations (UCFs) which are the fluctuations in resistance occurring over longer ranges of magnetic field.

Universal conductance fluctuations to the conductivity are specific to a given device. They occur as a function of magnetic field and chemical potential [124] as well as impurity configuration. Rather than arising from interference of pairs of time-reversed electron paths, UCFs arise from interference between all possible electron paths in the device. Further, UCFs are characterized by two length scales. The first is the dephasing length, $L_\phi = \sqrt{D\tau_\phi}$, where D is the diffusion constant and τ_ϕ is the electron dephasing time. In 2D metallic samples, however, the thermal length, $L_T = \sqrt{\hbar D/k_B T}$, the distance in which electrons differing in energy $k_B T$ become out of phase with each other, is the dominant UCF mechanism [125].

In Figure 4.18, a few example traces of weak localization in preliminary device 062415c3 are shown. In Figure 4.18(a), the peak near B = 0 T is small and noisy, with universal conductance fluctuations large enough that it is difficult to draw any coherent conclusions about the peak width or amplitude. Other examples of UCFs that do not dominate the weak localization are shown in Figure 4.18(b)-(c). In Figure 4.18(b), there is a sizeable fluctuation exhibited as a broad dip between 0.05 T and 0.1 T and in Figure 4.18(c), there is a similar dip around 0.025 T.

For this device, the pre-evaporation weak localization was largely dominated by noise

and UCFs, likely due to the initial impurity configuration and potential. This has been seen in several other devices. However, in Figure 4.18(b)-(c), it seems that the weak localization peak shown in red, which corresponds to the device after a single osmium deposition, has a larger amplitude but smaller width than the post-third evaporation peak shown in blue. This behavior is consistent across all measured carrier densities in this device, with exception to those where universal conductance fluctuations dominate. This indicates that after some osmium has been added to the graphene, the scattering potential is affected enough such that the signal-to-noise ratio improves and the universal conductance fluctuations are no longer dominant over the weak localization. As more osmium is added, the electron dephasing time decreases. This is altogether similar to results shown for tungsten adatoms on graphene in Chapter 3 and is in accordance with predictions of Altshuler *et. al.* [117] where a decrease in the diffusivity affects the electron dephasing time by:

$$\tau_{\phi}^{-1} = \frac{k_B T}{2\hbar} \frac{\ln(\pi\hbar\nu D)}{\pi\hbar\nu D} = \frac{k_B T}{2\hbar} \frac{\ln(k_F l)}{k_F l}, \tag{4.3}$$

with D again the diffusivity and ν the density of states at the Fermi level. The expression on the right accounts for the single layer graphene density of states $\nu = 2E_F/(\pi\hbar^2 v_F^2)$.

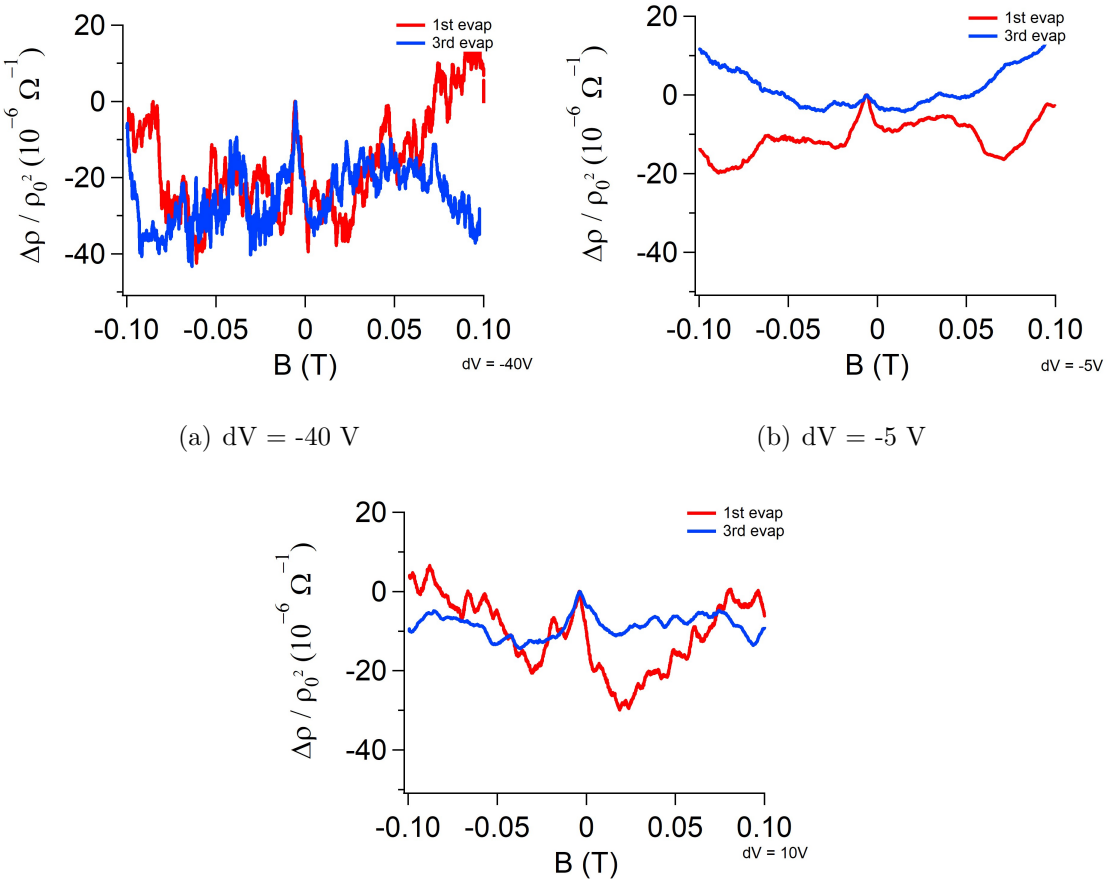

(a) dV = -40 V

(b) dV = -5 V

(c) dV = +10 V

Figure 4.18: Weak localization of preliminary device with osmium adatoms

We also measured weak localization in preliminary device 061416a1, however, both tungsten and osmium were deposited on this device. For this device, evaporations 1, 4, and 5 correspond to osmium adatom evaporations. For all carrier densities measured where the universal conductance fluctuations and noise are small in comparison to the weak localization, the post-evaporation state has a *larger* amplitude and a larger width. This is somewhat intriguing since tungsten adatoms (which were similarly fabricated preliminary devices) decreased the amplitude and increased the width. Thus, one would naively expect that if tungsten adatoms decrease the amplitude and osmium adatoms independently decrease the

amplitude, then it is likely that mixed evaporations of osmium and tungsten ought also to decrease the amplitude. However, these weak localization measurements were made without any averaging on small devices so it is possible that we are seeing effects of the device size and inherent scattering potential. In addition, the residual polymer layer left on the graphene is unlikely to be uniform or consistent between devices meaning the adatoms may settle neither a consistent height above the graphene plane nor randomly distributed on the surface.

For device 061416a1, we apply the McCann fittings [72] after each osmium evaporation step. We obtained the scattering times shown in Figure 4.19 with (a) being the dephasing time τ_ϕ and (b) the intervalley scattering time τ_i. Due to the mixed evaporations, we may not be able to draw clear conclusions about what these fits imply for osmium adatoms alone. However, we do notice a slight increase in the dephasing time with carrier density, consistent with tungsten adatom results shown in Chapter 3. In addition, the dephasing time decreases between the first and fourth evaporations. Whether this is a result of tungsten adatoms from evaporations two and three or a result of osmium adatoms, we cannot say. However, it is interesting to note that there is only negligible change in scattering times between the fourth evaporation and fifth evaporation. This saturation to the weak localization correction likely implies a saturation in changes to the scattering potential.

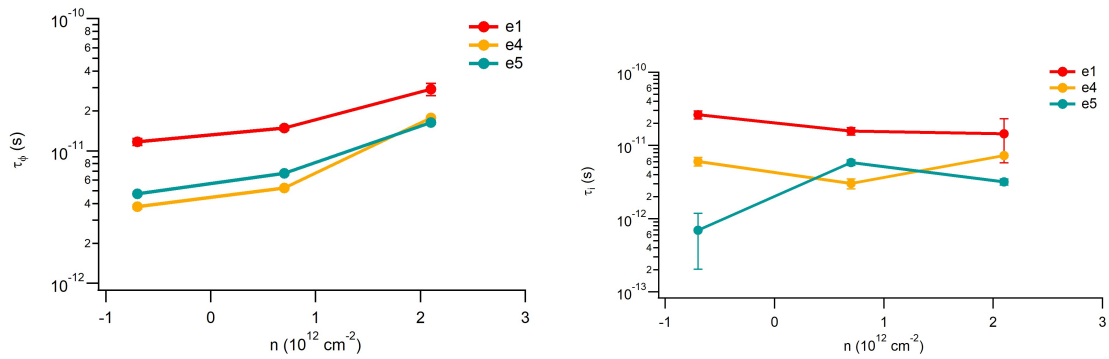

(a) τ_ϕ (b) τ_i

Figure 4.19: Dephasing and intervalley scattering times of osmium evaporations only

Shadow-masked devices

Weak localization was measured for all three shadow-masked devices. However, only device 022017b3 displayed a weak localization peak that was significantly larger than the noise in the clean and decorated devices. Because this is a 2-wire device, we keep in mind that the calculated resistance includes a contact resistance of unknown value. In Figure 4.20, we show the weak localization at three carrier densities before and after the evaporations.

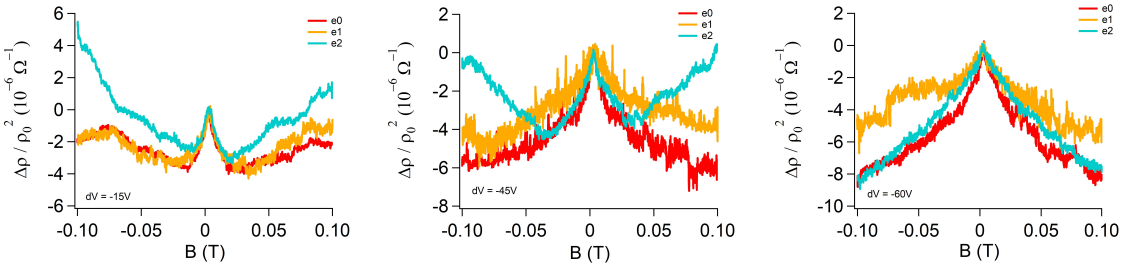

(a) dV = -15 V (b) dV = -45 V (c) dV = -60 V

Figure 4.20: Weak localization before (e0) and after evaporations (e1 and e2) for three carrier densities: (a) dV = -15 V, (b) dV = -45 V, and (c) dV = -60 V.

Unfortunately, the weak localization for shadow-masked devices is not well fit with the

McCann equation [70] given in Eq. 3.16. This may be due to the 2-contact configuration used, which results in the measured resistance including the contact resistance between the metal film contacts and the graphene. This causes a scaling adjustment which is not accounted for in $\Delta\rho/\rho_0^2$. This scaling results in fitting parameters that are not well constrained to physically reasonable results.

However, we qualitatively find: close to the Dirac peak, there is little if any change in the width of the weak localization peak. This is shown in Figure 4.20(a) where the width of the as-made, here labeled e0, and the post evaporation, e1 and e2, states are nearly identical. In addition, the amplitude of the peak is similar for the as-made and first evaporation and decreased after the second osmium evaporation. It is possible, however, that this amplitude of any or all of these peaks is affected by the universal conductance fluctuations. For the carrier densities far from the Dirac peak, dV = -45 V and dV = -60 V, shown in Figure 4.20(b)-(c), the width of the peak increases slightly after the first evaporation and remains nearly the same after the second evaporation. The amplitude of the peak seems to follow a similar trend where the amplitude decreases after the first evaporation and reverts to it's initial height after the second evaporation.

Overall, the width of the weak localization peak is also tied to the amplitude of the peak, and that amplitude is affected by the false scaling given by 2-contact measurements. This suggests it is possible that these small changes in the amplitude and width, which correspond to changes in the intervalley scattering time and the phase decoherence time, are entirely due to slight changes in the contact resistance, which lead to large changes in the scale of $\Delta\rho/\rho_0^2$.

AFM nano-broomed devices

We also measured weak localization in broomed devices at several carrier densities. In device 080317b2, the behavior of the weak localization is difficult to assign trends to. At five

of seven carrier densities measured, the weak localization peak gets broader after the first evaporation. For the remaining two carrier densities, the width is approximately the same before and after the first evaporation. After each evaporation, the device was annealed *in situ* to allow the osmium the opportunity to diffuse into its equilibrium position. After the first anneal, the peak width seems to remain the same or decrease, depending on carrier density. For all steps after the first anneal, the weak localization peak width remains constant. This indicates that the dephasing field increases with the first evaporation, usually decreases with the first anneal, and remains constant after all other evaporations and anneals. This implies the dephasing field is unaffected by the amount of osmium added to the surface after the initial evaporation and anneal. This behavior is shown in an example weak localization plot at a single carrier density in Figure 4.21(a). Altogether, this suggests that the first evaporation increases the scattering in the device, which decreases the average time between electron dephasing events. Then, during the first anneal, the adatoms move into equilibrium positions on the graphene surface. These positions reduce some of the added scattering and increase the average dephasing time. All other adatoms deposited after these steps have minimal effect on the scattering potential, as seen by the much smaller changes in mobility, and thus have minimal effects on the dephasing time.

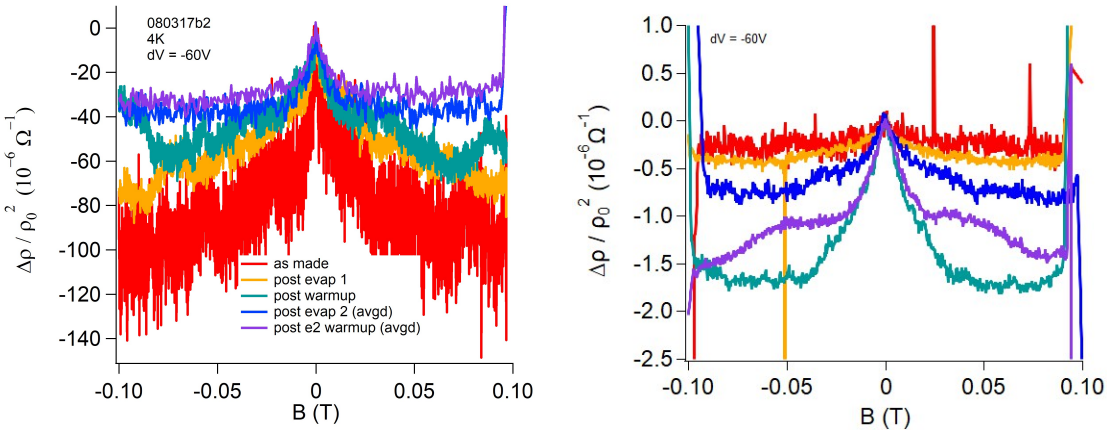

(a) 080317b2

(b) 092018a3 LHB

Figure 4.21: Example weak localization data from the broomed devices, both at dV =-60 V

Fits to the weak localization have been carried out for device 080317b2; the results are shown in 4.22. The dephasing times extracted from the simplified McCann equation [72] do not directly follow the theoretical phase breaking times calculated with Eq. 3.22 and are shown as dotted lines, using data from the as-made sample (dashed red) and after the 3rd evaporation and anneal (dashed purple). However, the data from the first anneal through the third anneal do follow the general trend, i.e. increasing τ_ϕ with increasing carrier density, and the values fall mostly between the theoretical values for the device in the as-made state and the device in the post third anneal (final) state.

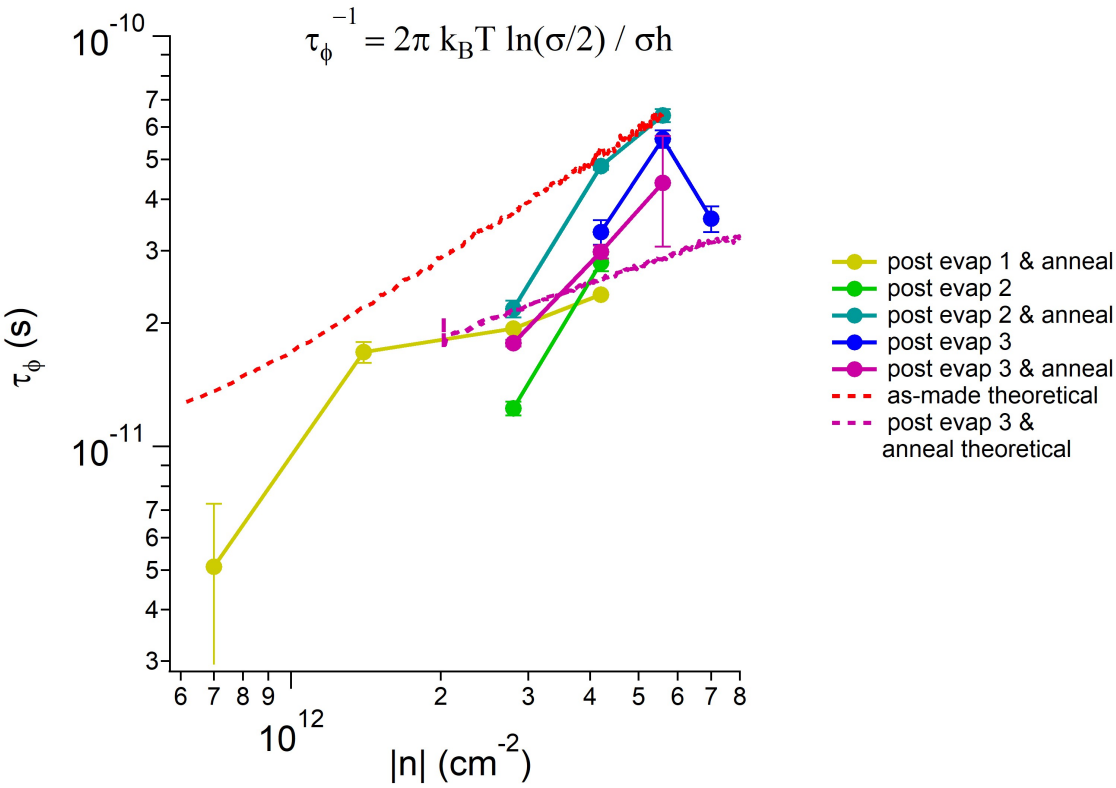

Figure 4.22: Dephasing times extracted from the weak localization

In the second set of devices (092018a3) both the large Hall bar and the small Hall bar were measured. However, the signal-to-noise ratio in the small Hall bar weak localization measurements was abysmal, even after a 17-point voltage averaging procedure. For this reason, we neglect to discuss weak localization in the small device. Furthermore, the large Hall bar had only three contacts available. As such, the weak localization measurements performed on 092018a3 LHB were 2-contact measurements.

Much like the shadow-masked devices, the attempted fits to weak localization data from 092018a3 LHB are affected by the unknown scaling caused by the contact resistance. However, qualitatively, the width of the weak localization peak after the first evaporation either remains the same or decreases slightly at the two carrier densities far from the Dirac peak.

At the carrier density closer to the Dirac peak, the width of the peak decreases more dramatically. After the second and third evaporations, the width of the peak varies with seemingly no pattern for the two measurements far from the Dirac peak, and reverts to the as-made width for the measurement closer to the Dirac peak. With the exception of one carrier density far from zero, the width after the final anneal remains the same as the width from after the third evaporation.

4.4.4 Temperature dependence

Preliminary devices

Should a band gap open due to spin-orbit coupling, it may be possible to see an effect on the temperature dependence of graphene. Preliminary device bz042215a was measured during the final dilution fridge warm-up. The results are shown in Figure 4.23. As the device warmed beyond around 40 K, the Dirac peak started shifting to the right. This is likely due to thermal activation; once the system temperature has increased enough, the adatoms will be able to diffuse. This rightward shift could indicate that osmium adatoms are diffusing along the surface of the graphene until they fall into a local energy minimum. Around 175 K, the original gate voltage range of -40 V to 40 V was not enough to keep the Dirac peak in sight which is why the range is extended to 60 V around 225 K. Shortly thereafter, the peak begins to travel leftward again to settle near 10 V at room temperature. At these high temperatures, it is likely that some of the adatoms were removed from the graphene surface.

The gap in the data around 30-40 K represents the switch from measuring the stage temperature via a thermocouple beneath the stage, which is adequate below 100 K and the Lakeshore 4K-plate thermometer, which represents the temperature of the 4 K plate of the fridge. The stage follows the 4K-plate temperature with a finite time gap. For the temperatures shown here, the thermocouple was used below 25 K and the 4K-plate

thermometer was used above 35 K.

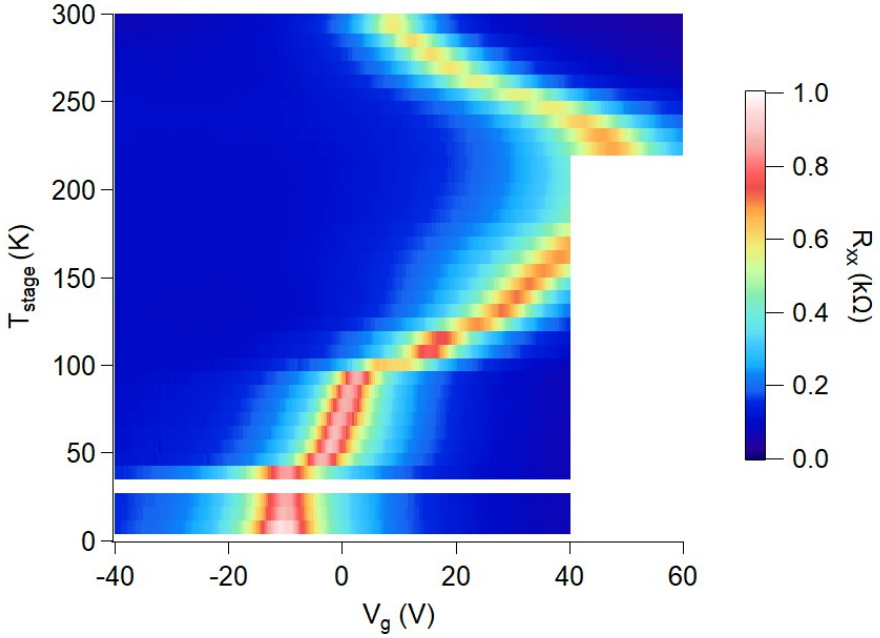

Figure 4.23: The resistance in color of device bz042215a versus both the gate voltage on the x-axis and the stage temperature on the y-axis.

Shadow-masked devices

We also report the temperature dependence of shadow masks. In Figure 4.24, we see that as the temperature increases, the Dirac peak shifts farther to the right until just after 150 K, where the Dirac peak begins to return toward lower gate voltages. Surprisingly, even up to 250 K, the graphene does not return to the initial state. This indicates that the osmium may be bonding in such a way that while it diffuses on the surface at finite temperatures, not all of the adatoms are removed from the graphene. The overall shape of this behavior is consistent with the measured preliminary devices.

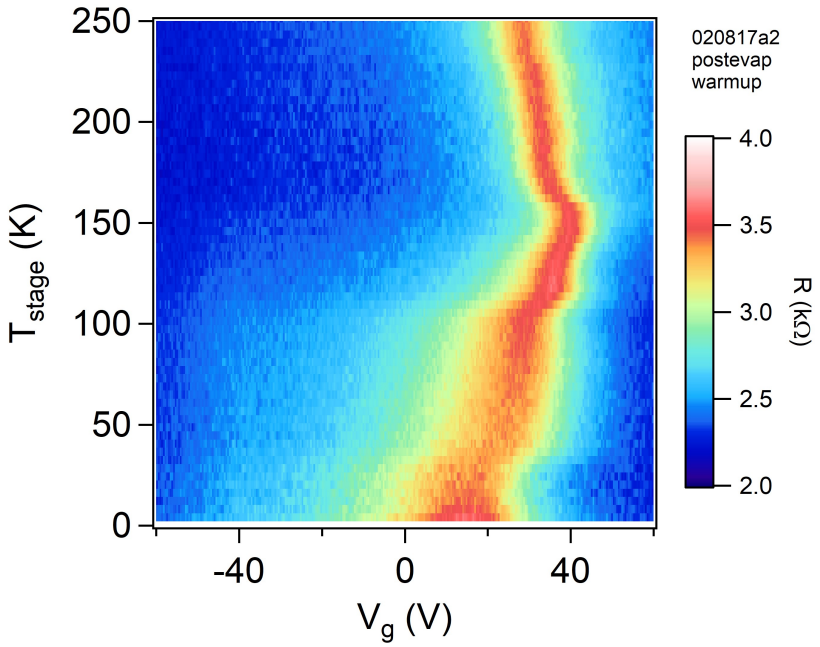

Figure 4.24: Temperature dependence of shadow-masked graphene transport with osmium adatoms decorating the surface

4.5 Surface measurements

For osmium decorated graphene devices, an effort was made into using various available surface measurements to determine coverage percentages and degree to which the osmium is randomly distributed, clustered, or settled into a pattern.

4.5.1 Energy Dispersive X-ray Spectroscopy (EDX)

In order to prove that our osmium wires contain a layer of osmium in addition to the tungsten base, we have performed EDX measurements on the osmium coated source wires. For a small region on a thinly coated tungsten wire, the EDX measurements resulted in 72.5% tungsten and 27.5% osmium. These values are not consistent with values reported

from Structure Probe, Inc. which deposited a 1 μm coating on our $\approx$19 μm wires. In addition, our SEM images confirmed the thickness of the osmium coating to be 0.4-1.0 μm. This would represent 2-6% osmium and 94-98% tungsten. Presumably, this discrepancy is due to the resolution of the spectroscopic measurement made. In addition, the chosen scan locations for spectroscopy may not have been properly chosen on the wire to represent the average wire morphology or could have been affected by tweezers loading the wires into the microscope. However, this measurement did confirm the presence of osmium on the tungsten wire.

Furthermore, we have attempted to measure the adatom density on the graphene surface using EDX after the 4 K measurements have been completed. Unfortunately, while the measurement does confirm the presence of osmium, the amount of osmium on the surface is too small to be observed using EDX. The EDX scan is shown in Figure 4.25.

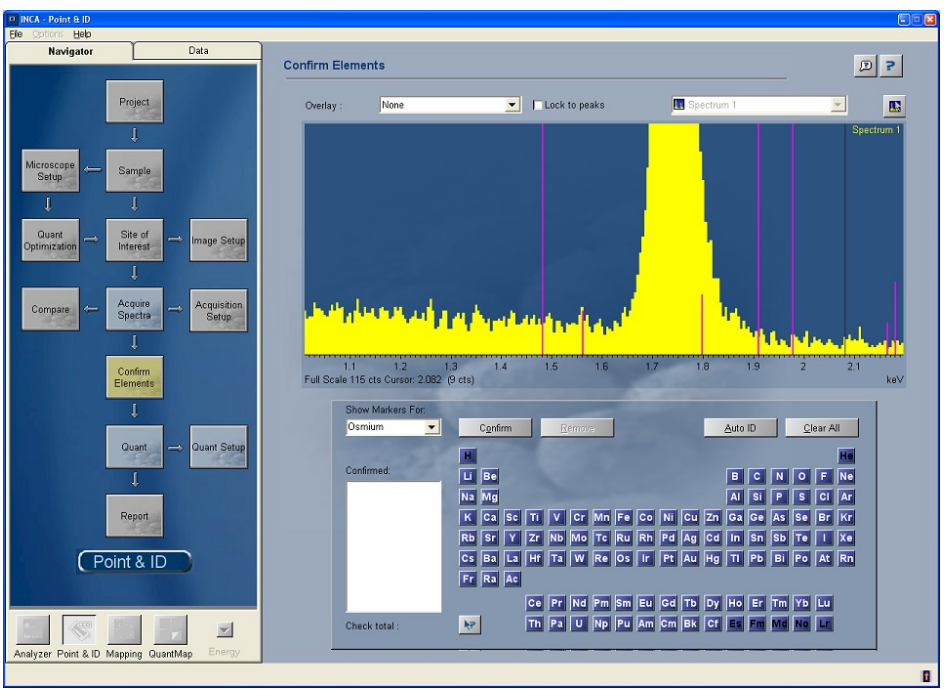

Figure 4.25: EDX spectra of graphene device 080317b2 after osmium adatom experiment. Small peaks are visible around where osmium signatures should be found.

4.5.2 X-ray Photoelectron Spectroscopy

Similarly, XPS was used to measure the amount of osmium present after an osmium adatom experiment on a broomed device. Both Table 4.2 and Figure 4.26 indicate that osmium adatoms are present and in extremely small amounts. Based on the 0.01% concentration of osmium in the measurement of exfoliated graphene, which should not have any osmium or tungsten present, it is believed that 0.01% may represent the measurement error or resolution of the instrument used.

In addition, one must note that in the device with osmium adatoms, a small but significant amount of tungsten was also found. This amount is about 20% of the measured osmium adatom concentration. This is likely due to error in the osmium evaporation process. In fact, because the vapor pressure of osmium and tungsten differ by a factor of 50, the current required to evaporate a tungsten source is only on the order of a couple 10s of mA larger than those necessary to evaporate osmium. In order to increase the temperature such that all of the osmium was removed from the source wire, we often increased the current through the wire by a small amount. While it was still 10s of mA from certain evaporation of the tungsten wire, it is possible that a hot spot on the wire, as described in Section 4.4.1, evaporated tungsten after all osmium was removed from on and nearby the hot spot.

In addition, evaporation occurs over a range of currents with only an approximated minimum current extracted by evaporation tests of the source wires. During such tests, we observed the Dirac peak of graphene while the current through the wire was increased. Thus, the minimum current used to evaporate tungsten is merely the average current such that a change in the transport of graphene was obvious. At lower currents, when the evaporation rate was slower, it is possible that the effect on graphene was less obvious. In this case, we may have unknowingly crossed the minimum current for tungsten evaporation while increasing the current to ensure full usage of the osmium source.

Device measured	Carbon	Oxygen	Silicon	Tungsten	Osmium
exfoliated graphene	15.15	56.26	28.59	0.00	0.01
fabricated, no adatoms	19.71	53.45	26.84	0.00	0.00
fabricated, osmium adatoms	25.45	50.25	23.65	0.11	0.54

Table 4.2: Concentrations of materials present in broomed osmium adatom device.

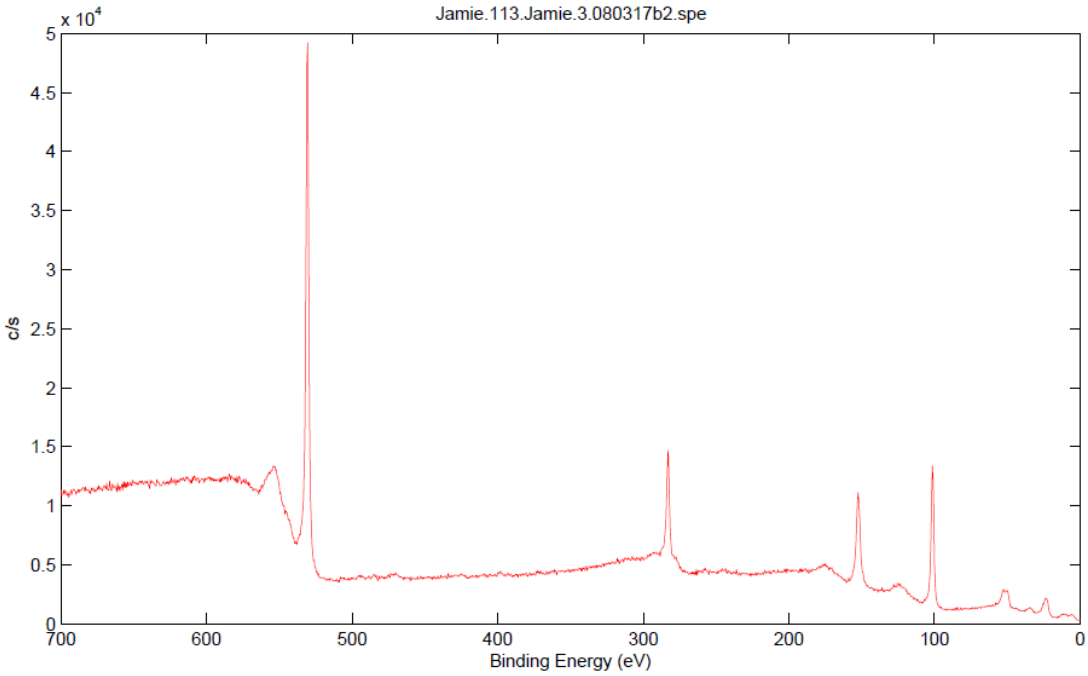

Figure 4.26: Measured XPS spectra of broomed graphene with osmium adatoms.

4.6 Discussion

Tying together the three types of devices on which osmium adatoms have been studied, we see several obvious connections. It seems that regardless of the mobility, substrate, or device size, osmium adatoms hole dope the graphene. This is interesting individually

because all other measured metallic adatoms - Au, Ca, Fe, In, Ir, K, Li, Mg, Pt, and Ti - electron dope [7, 16–25]. This may be due to the inherent electron configuration of osmium, though one would expect other transition metals such as tungsten to have similar electronic configurations and bonding schemes.

In addition, there is some evidence from these devices that the simple Coulomb scattering or short-range scattering models of electron transport is not adequate for osmium adatoms on graphene as it was for tungsten adatoms. Indeed, we could not extract a well-behaved or consistent exponent for the relationship between the change in Dirac peak location and the change in mobility.

Furthermore, our in-field measurements of weak localization, quantum Hall effect, and Shubnikov de Haas oscillations were insufficient to conclusively prove the presence of a spin-orbit coupling due to the adatoms. While the weak localization did change as adatoms were deposited, the changes were mostly indistinguishable from those that would occur due to differences in the scattering potential. From the conductivity and mobility data, we know that the scattering potential is changing as osmium is added and further, we know that it is changing in a more complicated way than the simplistic models we usually employ. For that reason, our conclusions about the weak localization data are insufficient *except* that we see no evidence of Rashba spin-orbit coupling, which would induce an antilocalization behavior. However, in device 080317b2, we did see that the amplitude and width of the weak localization peak saturated after the first evaporation and anneal. This resembles the behavior we would expect for a saturating phase-breaking time, which could indicate the presence of a symmetric spin-orbit coupling [72]. However, when the dephasing times are extracted (Figure 4.22), they vary significantly. Thus, the saturation in the conductivity correction must be due to a saturation in the changes to the scattering potential. Without temperature dependent weak localization data or the presence of an in-plane magnetic field, conclusive evidence for the presence of intrinsic spin-orbit coupling cannot be drawn.

In fact, without an in-plane magnetic field, the present models used for analyzing weak localization data are not adequate for distinguishing the effects of a changing scattering potential from the effects of an intrinsic spin-orbit coupling. Since an increase in scattering decreases the mobility, increased scattering decreases the phase-breaking time. This decrease in phase-breaking times, is altogether similar to the effect of a symmetric term present in Eq. 2.70.

Further evidence that we do not see Rashba spin-orbit coupling is shown in the lack of a beating resonance in the Shubnikov de Haas oscillations. Such resonances are of band origin and can be used to extract the spin-orbit interaction strength [35]. None of the osmium adatom data from any of the device types showed this behavior.

4.7 Conclusions

In conclusion, the inheritance of spin-orbit coupling from osmium adatoms on graphene has not been observed but there is much room for further work. For example, much effort was spent in increasing the size of measurable Hall bars for averaging of the universal conductance fluctuations in weak localization measurements. The ability to measure large devices for weak localization would be significantly improved with the presence of an in-plane magnetic field. This could be accomplished by either a rotating sample stage or by a small Helmholtz coil installed in the adatom dipper. Further, it has recently become obvious that to measure quantization due to edge channel conduction, which is a possible and desirable side effect of achieving the quantum spin Hall effect, we would like measurement contacts with separation distances several times smaller than those used. Instead of single devices with several microns between measurement contacts, it would be prudent to instead measure both a large device for weak localization as well as a small device having contacts with a separation distance on the order of hundreds of nanometers. One measured device was a so-named small Hall bar

but that particular device had strangely noisy transport and inconclusive nonlocal voltages in the pre-evaporation state. A more thorough analysis of smaller Hall bars is necessary to illuminate nonlocal voltage behaviors of graphene with osmium adatoms.

In addition, the amounts of osmium decorating the graphene surface are small while the theoretical predictions for the opening of a band gap due to inherited spin-orbit coupling are best above about 1% coverage. While thicker osmium layers on tungsten wires were thought to bring the coverage percent closer to this value, the likely poor evaporation from these wires caused the source wires to be less productive than previous batches, even considering that the source wires were 2 times closer to the graphene surface. This leads to the conclusion that *in situ* thermal evaporation of osmium is perhaps not the most efficient method for deposition. Indeed, other groups [126] have had success in using *in situ* electron beam evaporations for contacting and measuring 2D materials with custom-built systems under vacuum such that the samples need never be brought into atmosphere. A similarly designed electron beam evaporation of osmium adatoms could allow for depositions spanning much larger coverages.

It is possible that graphene on hexagonal boron nitride, which has an inherently higher achievable mobility than graphene on SiO_2, could improve weak localization results by decreasing the amount of universal conductance fluctuations present due to scattering. Since the initial scattering potential of graphene on boron nitride should be simpler than graphene on oxide, this may help with the current inability to use simplistic models in distinguishing changes due to an intrinsic spin-orbit coupling from those due to a changing scattering potential. In addition, a higher mobility graphene device may improve the resolution of Shubnikov de Haas oscillations measured at lower magnetic fields, which transitively increases the probability of seeing a beating resonance pattern in the oscillations if such is present. Of course, this beating pattern should also be observable as a transition from weak localization toward weak antilocalization.

Finally, another possibility for inducement of spin-orbit coupling (and the quantum spin

Hall effect) by osmium is to increase the size of the adatoms. Rather than depositing adatoms of osmium, instead osmium nanoparticles could be used. This would have the effect of both increasing the coverage percent drastically and increasing the amount of spin-orbit coupling present per particle. In this vein, copper nanoparticles have been shown to induce a giant spin Hall effect in graphene [26]. The difficulty of such a process reverts, however, to the deposition sourcing for *in situ* work.

4.8 Further Acknowledgements

We thank S. Adam, J. Alicea, U. Chandni, S. Das Sarma, M. Franz, M. Fuhrer, R. Mong, J. Pollanen, and M.-F. Tu for helpful correspondence and discussions, as well as Jeff Hall at SPI for providing the osmium plasma deposition necessary to coat the tungsten source wires.

Chapter 5

Investigation of Bi_2Te_3 nanoparticles on graphene

5.1 Introduction

During the pursuit of the induction of spin-orbit coupling to graphene for creating a 2D topological insulator (a 2D QSH system), preliminary measurements were made with Bi_2Te_3 nanoparticles. While another group has seen intriguing evidence that such particles may cause the presence of quantized edge channels [127], the data presented here shows no evidence of such quantization.

5.2 Methods

5.2.1 Graphene device fabrication

Graphene devices for Bi_2Te_3 nanoparticle decoration were fabricated from graphene flakes exfoliated using Scotch tape exfoliation. Chromium/gold contacts were made by standard electron beam lithography and thermal evaporation. The device used for this series of mea-

surements was etched into a Hall bar and nano-broomed to remove fabrication residues.

5.2.2 Deposition of nanoparticles

For Bi_2Te_3 nanoparticles on graphene, the deposition process is much different. Instead of evaporating the materials *in situ*, we deposit the nanoparticles in a cleanroom fabrication facility, then measure the device. For all measurements reported here, the device was coated in Bi_2Te_3 nanoparticles by spinning the wafer at 5000 rpm and using a syringe to apply a drop of Bi_2Te_3 nanoparticles suspended in toluene onto the spinning wafer. For each step, the device was measured in a liquid cryogenic Quantum Design Physical Properties Measurement System (PPMS).

For the nanoparticle covered device, three measurement steps were used. First, the nanoparticles were deposited on the graphene and their density measured to be 1 nanoparticle per $(100\ \text{nm})^2$. The particles are approximately 15 nm in diameter with a 1 nm coating of Polyvinylidene fluoride (PVDF) and exhibit a large concentration of stacking faults in the nanoparticles. The usual transport measurements were then performed at 2 K in the PPMS.

Second, the device was removed from the PPMS and the PVDF coating on the nanoparticles was removed by a tube furnace anneal at 200° C with 0.5 scfh of Ar. For this anneal, the ramp up to 200° C was set for 1 hour and we dwelt at that maximum temperature for 3 hours. After an overnight Ar purge of the tube furnace, the device was removed and reloaded into the PPMS. Due to the low temperature of indium solder, the back gate required re-soldering before we could reload the device into the PPMS.

Finally, the third step was to remove the device from the PPMS, apply another 3 drops of suspended particles while spinning, and perform another tube furnace anneal with 2 hour dwell time. The device was reloaded into the PMMS and measured again. During this anneal, the back-gate solder connection did not become disconnected.

AFM images of the device after brooming, with the first nanoparticles, and after the

second deposition and anneal are shown in Figure 5.1. As shown in Figure 5.1(c), the final density of nanoparticles is a bit ambiguous. In the shown AFM image, it appears as if nearly 50% or more of the graphene is covered by nanoparticles. However, because the anneal temperature was only a little larger than the melting temperature of the PVDF, it is possible that while the PVDF was removed from the nanoparticles, it was not removed from the graphene surface. A similar wafer without a graphene device was measured in an SEM after 4 drops of nanoparticle suspension were dropped on the wafer with the same spin speed. This wafer is shown in Figure 5.2. Indeed, the simplistic assumption that 4 drops would account for a density 4× that of 1 drop is inadequate due to clumping and clustering of the nanoparticles.

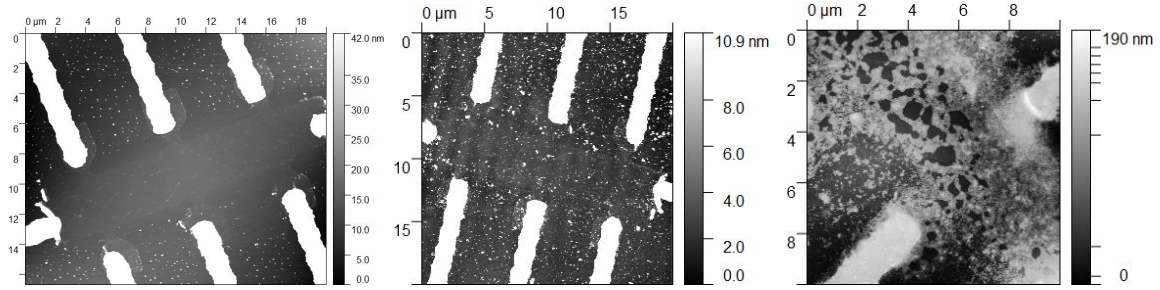

(a) broomed device (b) 1 drop suspension (c) 4 drops and annealed

Figure 5.1: The AFM broomed device (a) immediately after brooming, (b) before measurements but after depositing 1 drop of suspended nanoparticles, and (c) after all measurements have been completed i.e. after 4 drops total of suspended nanoparticles are deposited and the PVDF coating has been annealed.

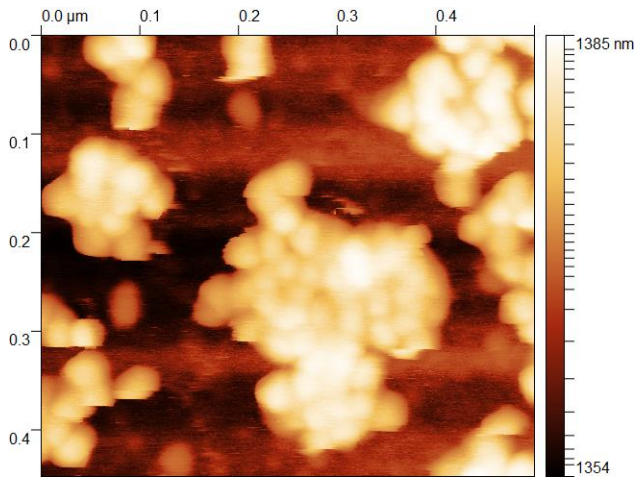

Figure 5.2: A wafer with 4 sequential drops of nanoparticle suspension applied while spinning at 5000 rpm. The density is much higher than 4× that of 1 drop of nanoparticle suspension spun at the same speed. This is likely due to clustering of the nanoparticles causing later drops to not spread the particles as thoroughly as the first drop was spread.

5.3 Results

Interestingly, Bi_2Te_3 nanoparticles before annealing to remove the PVDF have little-to-no effect on the graphene transport. Even with the PVDF coated nanoparticles, the broomed graphene Dirac peak is near zero and narrow. This means the mobility is high, starting around 29,000 cm^2/Vs on the hole side and 36,000 cm^2/Vs on the electron side. After the first anneal, this mobility dropped to around 12,000 cm^2/Vs. Then, after many more particles are added and annealed again, the mobility drops to around 6,000 cm^2/Vs. This is shown in Figure 5.3.

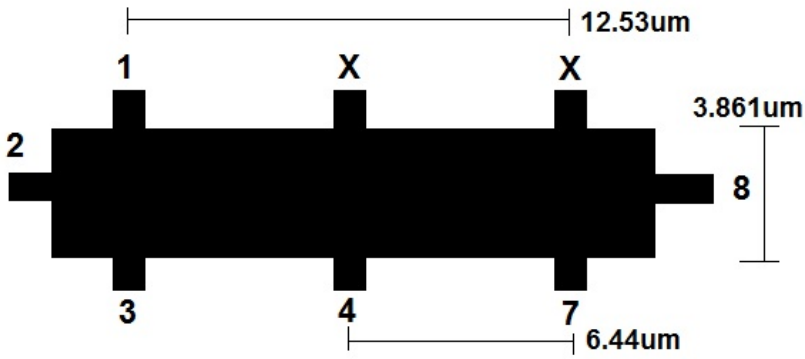

(a) Hall bar configuration

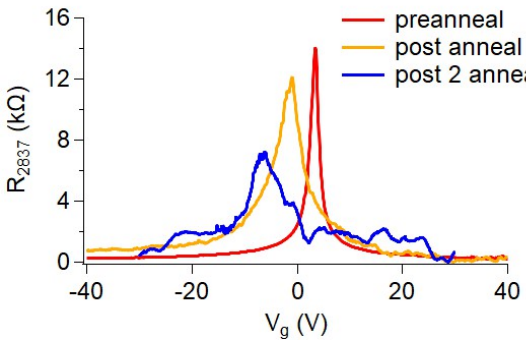

(b) Dirac peak evolution

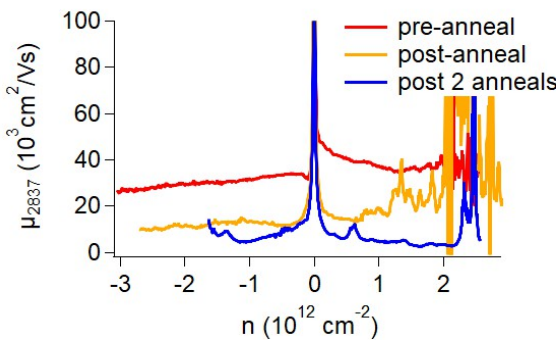

(c) Mobility evolution

Figure 5.3: (a) Bi_2Te_3 nanoparticles electron dope, moving the Dirac peak to the left and (b) do not affect the mobility much until the PVDF has been melted.

For the Hall bar with contacts shown in Figure 5.3(a), sweeps of the Dirac peak were measured for a large variety of 4-contact and 2-contact configurations. A few example sweeps are shown in Figures 5.4 and 5.5 with the expected quantization resistance marked by a horizontal line with color correspondence to the colored traces on the graph. These expected values were calculated via the Landauer-Büttiker formalism [49].

In addition to the contact configurations shown, many more configurations were tested including a large sampling of 2-contact measurements. While a couple of these traces approached the expectation value, such as configuration 3714 of Figure 5.5, we rule out quantum

spin Hall quantization and determine that these resistances are merely coincidental. For example, in Figure 5.5, configuration 3748 and configuration 3847 should be nearly identical for standard transport in a Hall bar device but take on distinctly different quantized resistance in a QSH system. In the pre-anneal device, nanoparticles are present but no spin-orbit coupling should be inherited yet due to the PVDF coating limiting charge carrier hopping between the nanoparticles and the graphene. Thus, transport in the pre-annealed device should follow standard patterns of transport in a graphene Hall bar. And indeed, one can hardly tell that the dark green trace is underneath the dark purple trace. However, even in the post-anneal picture, the data is similarly identical. This indicated that we have not yet induced a spin-orbit coupling such that the graphene becomes a quantum spin Hall system.

Furthermore, after the addition of more nanoparticles and annealing of the PVDF, the many contact configurations were remeasured and checked for evidence of quantum spin Hall quantization. Unfortunately, no evidence that the graphene has become anything more than a standard disordered system was found. For example, in Figure 5.6, a few contact configurations are shown with their expected quantized resistance values. Coincidentally, one of the values approaches a resistance near the quantization expectation, however, we know that it is not truly quantized due to similar reasoning from the previous figure.

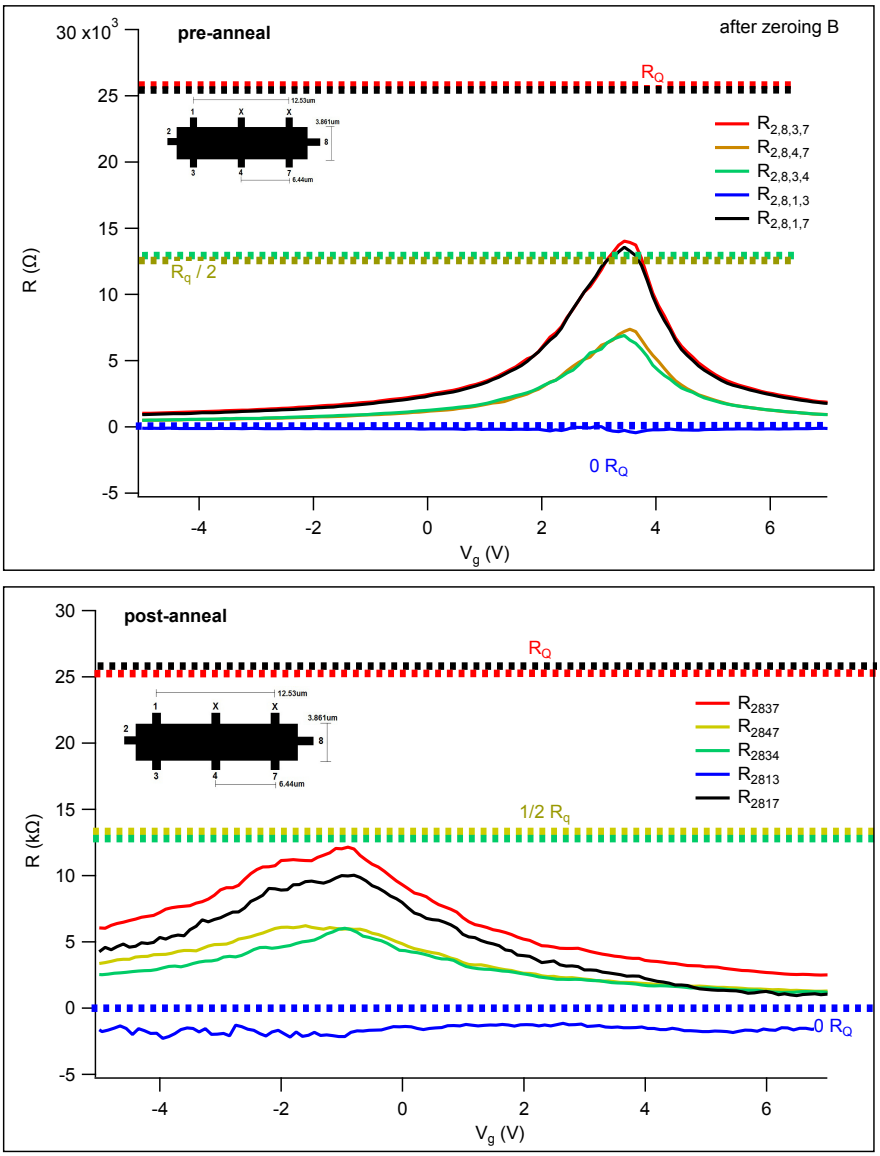

Figure 5.4: A comparison of the pre- and post-anneal gate sweeps for a variety of 4-point contact configurations where the current is run from contact 2 to ground at contact 8. The expected resistances for an induced quantum spin Hall effect are labeled horizontal lines with colors corresponding to the color for each contact configuration. For example, the red dotted line is the expected quantization for the red solid line.

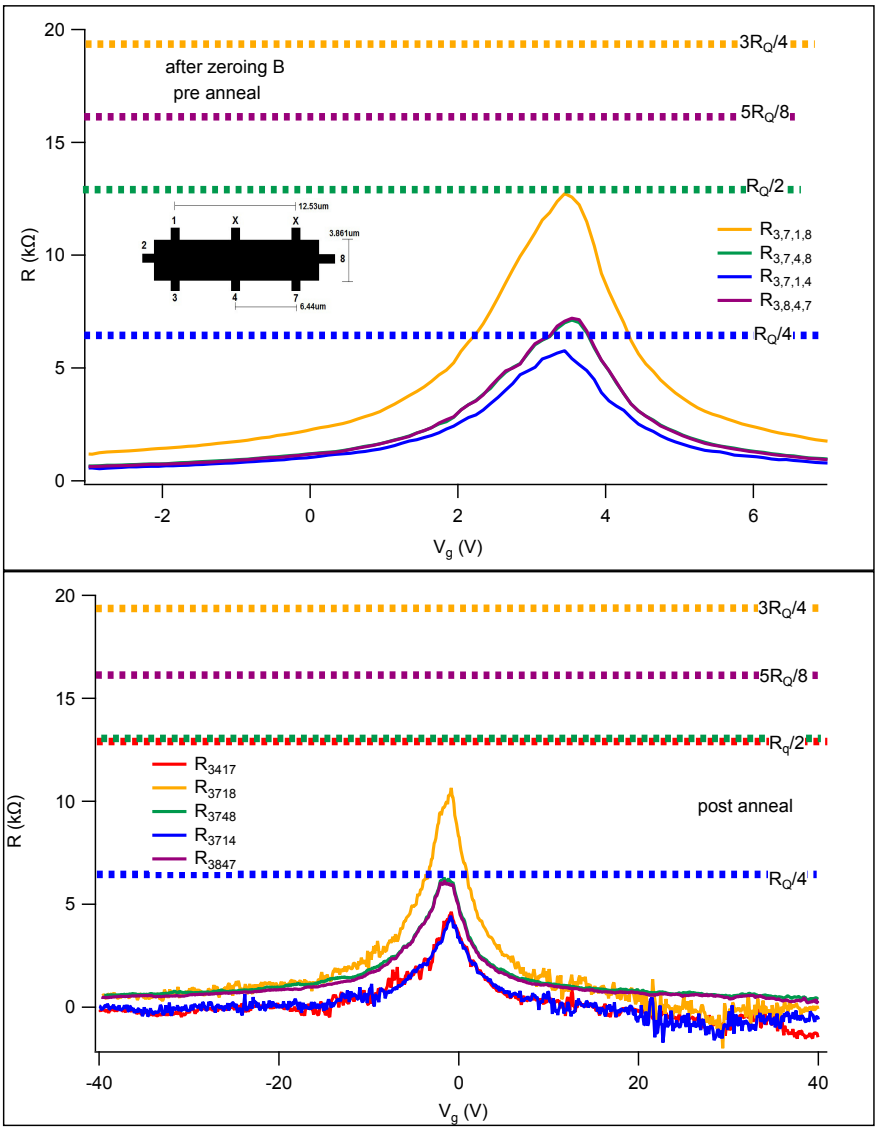

Figure 5.5: A comparison of the pre- and post-anneal gate sweeps for a variety of 4-point contact configurations where the current is run from contact 3 to ground at contact 7. The expected resistances for an induced quantum spin Hall effect are labeled horizontal lines with colors corresponding to the color for each contact configuration. For example, the red dotted line is the expected quantization for the red solid line.

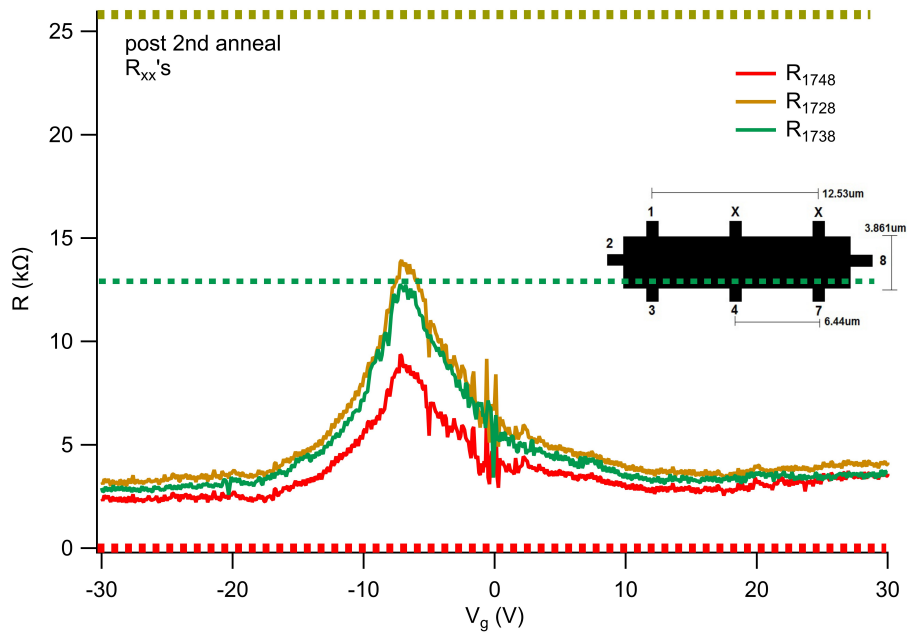

Figure 5.6: After 2 depositions and anneals to remove the PVDF, the graphene transport is still not representative of that expected for a quantum spin Hall system. While the R_{1738} configuration approaches the expectation value, this is likely coincidental considering that R_{1738} is nearly identical to R_{1728} which would not occur for a quantum spin Hall system.

Finally, the quantum Hall effect was measured in the graphene device with pre-annealed Bi_2Te_3 nanoparticles, after the nanoparticle anneal, and after the second deposition and anneal. Nothing surprising came from these measurements. After the first nanoparticles were annealed and after more nanoparticles are added and annealed, the Landau fan shifts leftward and begins to smear out. This is shown in Figure 5.7 and is altogether similar to the results found with tungsten adatoms.

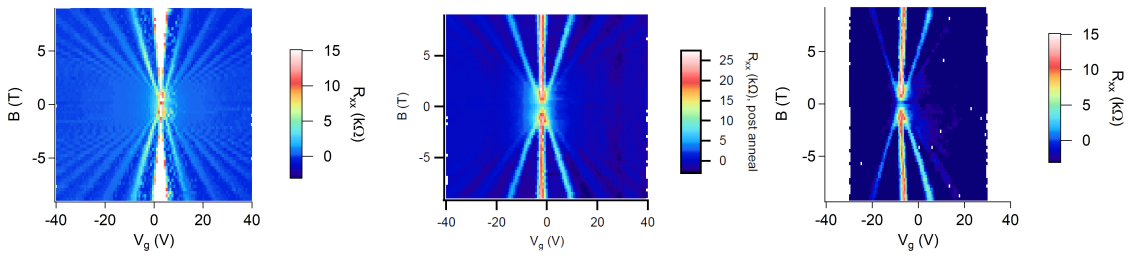

(a) pre-anneal (b) post-anneal (c) post-anneal 2

Figure 5.7: The standard quantum Hall effect Landau fan for graphene with nanoparticles (a) before annealing, (b) after annealing, and (c) after a second deposition and anneal

5.4 Conclusions

In conclusion, Bi_2Te_3 nanoparticles were found to electron dope the graphene, which is unsurprising considering that most adatoms also electron dope graphene with the exception of osmium. In addition, Bi_2Te_3 nanoparticles decreased the mobility of graphene significantly after the PVDF coating was melted. Based on the AFM images of the device, we believe that while the PVDF was melted off the nanoparticles, it seems to have adhered to the graphene surface. Presumably, this is responsible for the negatively affected mobility of the graphene. In order to improve results, a series of tests should be performed to find a more aggressive anneal process that will completely remove the PVDF without damaging either the nanoparticles or the graphene. If this is not chemically viable, then it should also be possible to use a different plastic coating on the particles rather than PVDF.

Unfortunately while these nanoparticles have significant potential for inducing the quantum spin Hall system to graphene, we were unable to reproduce the quantization seen by Hatsuda *et al.*. Obviously, a more thorough investigation would need to be done with devices designed with smaller contact separation distances to further elucidate the nature of the effect of these nanoparticles on monolayer AFM broomed graphene devices.

5.5 Further Acknowledgements

We would like to thank W. Buhro and F. Wang (Chemistry Department) for providing the nanoparticle suspension used in this work as well as A.S. Thind (Institute of Materials Science and Engineering) and R. Mishra (Engineering) for performing the STEM characterizations on the Bi_2Te_3 nanoparticles. We also thank J. Alicea (Caltech) for helpful discussions.

Chapter 6

Conclusions

6.1 Overview

In summary, we have examined the effects of two transition metal adatoms on monolayer graphene devices. Tungsten adatoms were found to electron dope the graphene, each adatom donating an electron to the graphene and leaving behind a charged ion. These ions act as isolated charged scattering centers and the mobility is decreased. Unfortunately, no evidence of inherited spin-orbit coupling has been found. We hypothesize that this ineffectual result is likely due to a polymer impurity layer covering much of the graphene surface due to standard fabrication procedures.

Unlike tungsten adatoms, osmium adatoms hole dope the graphene and decreased the mobility much less than tungsten adatoms even considering that the tungsten effect on graphene was inhibited by a polymer impurity layer. Furthermore, osmium-decorated devices were studied with a variety of fabrication procedures including those that require no polymer resist (shadow-masking) and those where the polymer layer has been thoroughly removed (AFM brooming). Results for all device types decorated with osmium are consistently different than for tungsten decoration. Indeed, all measurements done with tungsten-

decorated devices indicate that tungsten donates an electron and becomes an isolated charge impurity laying about 1 nm above the graphene plane. Not only do osmium adatoms hole dope instead of electron dope, but the simple picture of an isolated charged impurity lying just above the graphene plane also does not suffice. However, osmium adatoms are not behaving as clusters either.

While osmium adatoms behave differently than tungsten adatoms, the inheritance of a spin-orbit coupling from the adatoms has not been clearly proven. These adatoms certainly change the dominant scattering potential of graphene, however, any evidence for the inheritance of a spin-orbit coupling in the measured systems is considered circumstantial at best and more realistically only serves as a *lack* of evidence for the presence of Rashba spin-orbit coupling.

6.2 Future extensions of Work

As mentioned in previous chapters, there are always improvements that could be made to experimental works. While achieved to some degree by AFM brooming, further improvements to the graphene initial mobility and transport behavior could be achieved by using a cleaner substrate than SiO_2. Already, much progress has been made to produce higher quality devices by stacking graphene on hexagonal boron nitride.

Further, in order to conclusively report that tungsten adatoms are unlikely to produce quantized edge channels such as would be found for the quantum spin Hall effect, the measurements made with tungsten adatoms should be repeated with AFM broomed devices. It is possible that the disappointing results from tungsten adatoms are due to the adatoms' inability to closely interact with the surface due to the polymer residue left behind from fabrication. However, this seems unlikely due to the similarity between tungsten adatoms on graphene and indium adatoms on graphene [16, 17].

On the other hand, there are a variety of other promising systems predicted for adatoms on graphene. Indeed, not all the options for obtaining a quantum spin Hall system have been exhausted. Other adatoms such as lanthanum or hafnium could also induce a spin-orbit coupling to graphene. Others such as lithium have been predicted to cause graphene to become superconducting at low temperatures [96, 98]. See Appendix C for preliminary information on lithium adatoms. In addition, magnetic adatoms may be another interesting route of study. Rather than directly probing the quantum spin Hall system with two quantized edge channels, instead the quantum anomalous Hall effect or other magnetic properties may be induced by adatoms with magnetic moments [128].

Furthermore, it may become easier to distinguish spin-orbit coupling behaviors in magnetoresistance if an in-plane magnetic field was present. In order to accomplish this *in situ* two possibilities are presented. First, a small Helmholtz coil could be designed and positioned internal to the adatom dipper and superconducting solenoid such that when turned on, the coil applies an in-plane magnetic field to the graphene. Alternatively, a mechanized stage that rotates within the adatom dipper could be used to translate between an applied field orthogonal to the device wafer and an applied field in the plane of the device wafer. Unfortunately, this would require extensive reworking of the adatom dipper design and wiring.

Another useful adaptation to this work would be to design an independent measurement of the adatom evaporation rate and density. In fact, much work has been done in pursuit of this measurement.

Finally, perhaps the most likely of improvements to the graphene with adatoms system presented here would be an improvement of the deposition system itself. This system is perfectly adequate for the evaporation of tungsten and lithium. In addition, the clever designs have allowed for evaporations of osmium while the graphene device remains below liquid nitrogen temperature. However, because of the method used to produce osmium

coated source wires, larger coverage percentages are more difficult to achieve. Indeed, in an experiment where the deposition density should have tripled due to the thickness of the source material, we have shown that the deposition density is actually less than previous experiments. In addition, it is easy to bring the wire temperatures too high and either break the wires or simultaneously evaporate tungsten. For these reasons, it may be prudent to look toward electron beam evaporation.

Appendix A

Fabrication techniques

A.1 Introduction

Devices used in the adatom and nanoparticle experiments are almost exclusively monolayer graphene on degenerately doped Si/SiO_2 wafers with resistivity around 0.005 Ω/cm. Some devices referenced in this study, however, are monolayer graphene on hBN on Si/SiO_2 wafers; these devices are identified by naming schema with a gbn- prefix or a -flip postfix. We use the scotch-tape exfoliation method via Novoselov *et al.* [2, 129] for early devices and the enhanced productivity of Huang *et al.* with oxygen plasma etching and hot plate warming [130]. Two common techniques for contacting graphene monolayers were employed including electron beam lithography and shadow masking. Various cleaning methods were studied including: acetone soaking, glacial acetic acid soaking, vacuum annealing, gaseous annealing, and AFM brooming. For a comprehensive analysis of these techniques in relation to the adatom project, please see Appendix B.

A.2 Large area exfoliation methods

Weak localization signatures are highly affected by the measurement area of the device. Due to the nature of scattering in graphene, weak localization peaks in devices are balanced with significant noise due to universal conductance fluctuations (UCFs), as discussed in Chapter 2. In order to minimize these UCFs, we increase the width of the hall bar to effectively average out the UCFs. This requires large exfoliated flakes. With standard 3M Scotch tape and Kish graphite flakes, we follow the method of Novoselov *et al.* and Huang *et al.* to produce large area monolayer graphene.

First, the degenerately doped Si/SiO_2 wafers are cut into approximately 1 cm $\times$ 1 cm squares with a diamond-tipped scribe. The wafers are then blown free of dust with dry N2 gas. No appreciable difference was found in devices production or cleanliness when dipping or soaking the wafers in solvents such as acetone and isopropanol before the N_2 dry step.

Next, the graphite tapes must be prepared. Figure A.1 includes step-by-step photographs of this process. A length of tape about 6 in long was cut and held to a lab bench upside-down with other pieces of tape. The tape being held will become one of many source tapes. Several large flat pieces of graphite from the supply vial are chosen and arranged carefully on the tape in a line approximately 1 cm in length. The flakes are placed in such a way as to minimize the space between graphite pieces. A second length of tape is cut and used to copy the line of graphite. To copy, the tape is lined up in such a way that the new line will be wherever desired on the copy tape, brought into contact, and very gently and slowly peeled to separate the tapes. In several steps, the first line of graphite is copied into 2 lines, then the 2 lines are copied into 4 lines, etc, until an about 1 cm $\times$ 1 cm square of graphite pieces is ready on both tapes. This square of graphite is then copied so that there are 2-4 squares on one tape. And finally, that tape is copied to make a handful of copy tapes. Tapes are typically stored in air in slotted containers for further copying or exfoliation later. After a

tape has been unsuccessful in producing usable graphene monolayers more than once, it is disposed of in the standard trash.

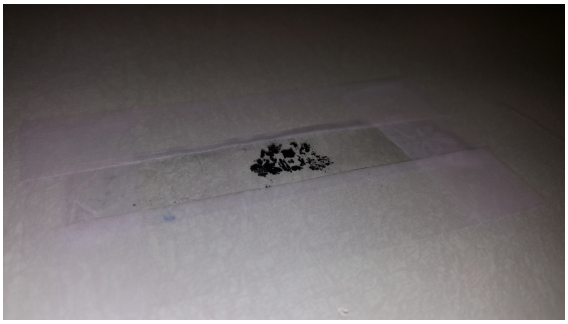

(a) graphite tape

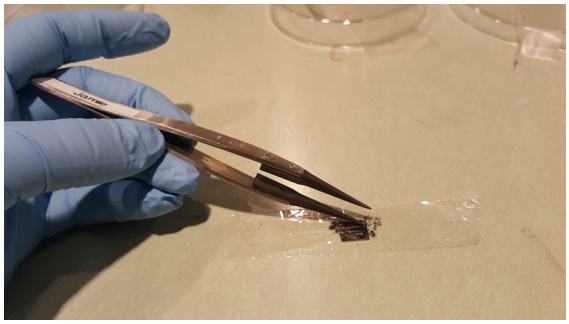

(b) copying the tape

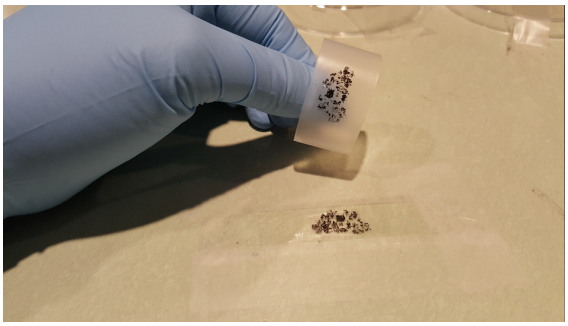

(c) second tape

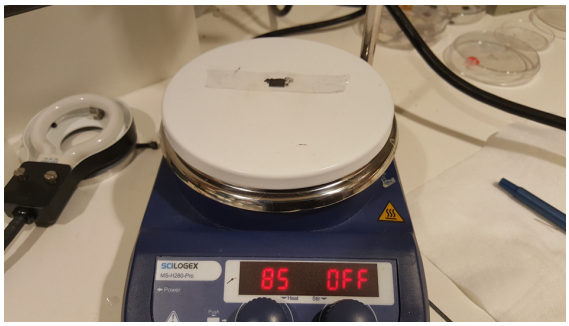

(d) hot plate method

Figure A.1: Step-by-step photo log of the scotch-tape exfoliation process. (a) tape secured to the lab bench with graphite flakes arranged on it,(b)-(c) copying the graphite tape to other tapes, (d) warming on the hotplate for better production rates

Without any further processing, each of these tapes may be applied to the Si/SiO_2 wafers, pressed or scratched with tweezers, markers, or fingers to put the tape into full contact with the wafer, and finally peeled from it to produce a wafer that has tape glue residue, graphite pieces, and thin graphene layers (1-10 layers). Different tape brands and types have been used but the most successful has been 3M Scotch Magic tape. Both 3M Scotch Transparent and Removable will produce graphene flakes but the amount of tape glue residue on the wafer is detrimental to the fabrication processes. With experience, it has been determined that

peeling the tape quickly, indeed aggressively ripping it off the wafer, at nearly 90° produces more viable results than gently and slowly peeling the tape from the wafer. In addition, while others have found that never pressing the tape onto the wafer or pressing lightly with a pair of tweezers has been more successful for their yield, the best yield found in this document occurred when the tape was pushed onto the wafer with incredible force by the pad of a gloved finger.

Two methods of aggressive ripping were found appropriate. In the first, the wafer and tape are stood at a 90° angle on the table with a pair of carbon-fiber tipped tweezers holding it vertically from under the tape. The tweezers are then used to wrench the wafer off the tape. One problem with this method, is that the wafer occasionally snaps back into place on the tape, leaving more tape-glue residue behind, and unfortunately often contaminating the exfoliated pieces. The second, perhaps easier and more common way, is to lay the wafer and tape flat on the table. A small corner of the tape is lifted enough to put the tweezers into vertical contact with the corner of the wafer. A large force is applied to hold the wafer flat while the tape is violently ripped off the table and wafer. Two common problems occur with this method; first is that the tweezers will slip, leaving a scratch or tape-glue smear across the wafer and/or second, the tape will shred from the fast peeling.

To increase the yield of large-area graphene flakes left on the wafers, we employ the technique of Huang [130] *et al.* to clean the wafers and warm the tape. In this procedure, we prepare both the wafers and the source tapes ahead of time. After cutting and dust cleaning, the wafers are plasma cleaned. This can be done with a quick Reactive Ion Etch (RIE) procedure but is equivalently, and perhaps more quickly, done with an oxygen asher. In this document, the Plasma Etch 50 Asher is more often used with a power of 100 W and flow rate of 30 sccm oxygen for 30 seconds. The wafers are removed and immediately put into contact with the source tapes. The tapes may then be peeled for results with minimal tape-glue residue. However, because graphene exfoliation is more often art and luck than

pure scientific process, it occasionally becomes necessary to adopt yet another step in this process. With the detriment of more tape-glue and large graphite flakes also deposited, taking the newly ashed wafers with tape in contact and placing them on a hot-plate at 100° C for 1-2 minutes also usually increases the yield of monolayer graphene deposited.

To identify the now exfoliated large graphene pieces for use in device fabrication, we scan the chips in an optical microscope. For most devices, a Zeiss Axiotron fitted with ×2.5, ×10, ×20, ×50, and ×100 objectives was used. Once the device is mounted onto the microscope stage, a corner is chosen as the start point and the chip is scanned manually at ×10 magnification from the chosen corner to the opposite corner. At every place where a usable flake is seen, photos at each magnification and notes as to the size, number of layers, and location are taken.

After a bit of practice, viewing layers optically at multiple magnifications was sufficient to determine the number of layers. While this could be confirmed via Raman Spectroscpy and AFM step height measurements, this was found unnecessary for the extent of this work. Instead, a database of color contrast at particular optical settings (light voltage 5 V, ZENlite software) was both computerized and mentally diagrammed. See Figure A.2 for a sampling of the optical color contrast database.

A.3 Shadow-mask contacts

Because contact fabrication has been proven to leave behind polymer residues even with the most aggressive solvent soaking and various annealing techniques, we sought methods of producing contacts to the graphene without applying any polymers to the surface. In effect, we would then be able to measure graphene in its most inherent state and applying adatoms or nanoparticles would then be the only variable added to the system.

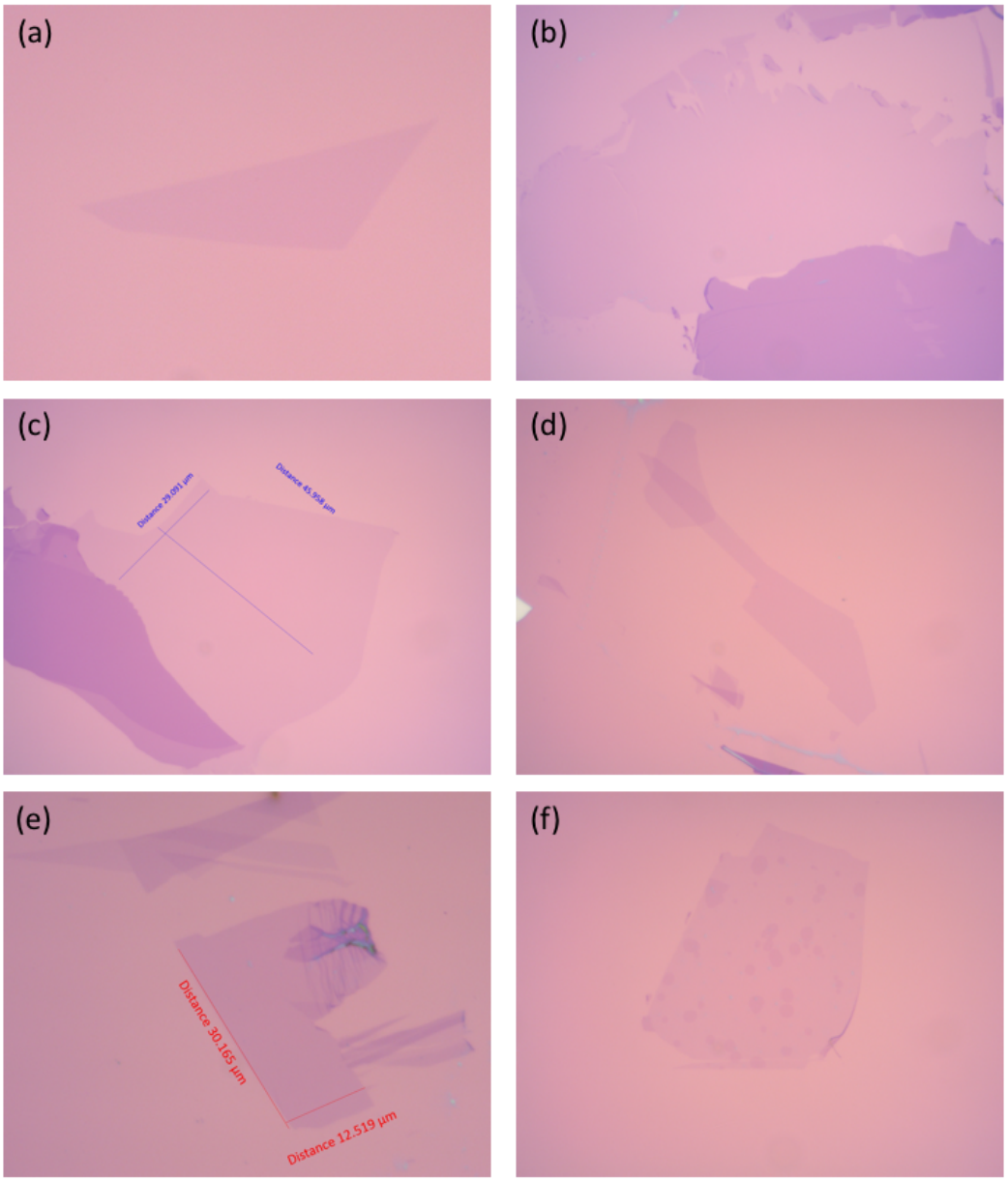

Figure A.2: (a) An isolated monolayer flake, (b)-(d) monolayer graphene pieces with varying sizes of multilayer attached on at least one edge, (e) a bilayer graphene flake identifiable by the nearby monolayer, (f) a monolayer speckled with approximately circular bilayer patches

First attempts at shadow-masking were made by producing a mask from suspended SiN windows. These windows are 3 mm diameter cylinders of SiO_2 with a 1 mm square etched in the center and SiN suspended over the etched square. The SiN windows from Ted Pella, Inc. can be purchased such the suspended nitride layer is between 15 nm and 200 nm. Focused ion beam etching of these windows with a working distance of 10 mm and a beam current of 500 pA into standard contact patterns was unsuccessful. While, at times, a shape or two could be cut into the window without damage to the window or pattern, almost universally the window would eventually rip the pattern causing contact shorts. See Figure A.3 for example masks attempted by this method.

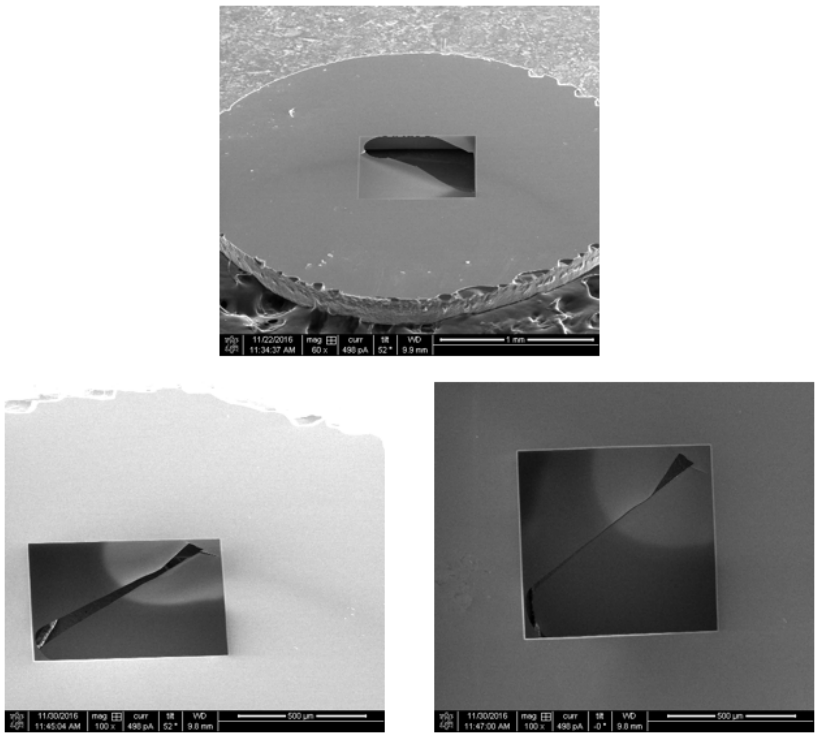

Figure A.3: (a) First attempts to pierce the mask resulted in broken SiN, (b) a triangular contact shape rips SiN across the entire mask, and (c) a less dramatic (narrower) but equally destructive rip from the contact

Second attempt shadow masks were made via polymer lithography and reactive ion etch-

ing of the SiN windows. In this method, each window was spun with PMMA A4 at several-thousand rpm for 45-60 seconds. Because of the extreme sensitivity of the SiN windows to any force, vacuum chuck holding during spin coating was not possible. Arranging the window onto the center of the spin coater chuck without vacuum was arranged via double sided Kapton or carbon tape. Tweezers were a common mode of destruction during this step. The PMMA was then hardened by hot-plate baking for 180 seconds at 150° C. An electron beam lithography pattern was created for 8 contacts in a standard hall-bar-like arrangement. The contacts were rounded at the edges for reduction of strain and breaking force in the SiN window upon etching. The pattern was drawn via standard electron beam lithography then the exposed SiN was etched with a CF_4 plasma for a series of times until the pattern was etched through the window. In Figure A.4, (a) shows the lithographic pattern on the SiN window, (b) is the window after 1 min and 45 sec of CF_4 etching, and (c) is after 2 min and 15 sec of etching. We can tell by color contrast and the piece of dust sitting on the leftmost contact of the shadow mask that in step (b), the SiN has not yet been etched fully through. In (c), however, at 2 min 15 sec, the SiN has been etched through and two of the contacts are shorted across what would be the graphene area. The unfortunate weakness of these suspended windows means that even in mass production, it it unlikely that many successful masks would be produced. However, if these masks were capable of making it through this fabrication process, it is possible that several metal evaporations towards the contacting of graphene or other 2D devices may strengthen the suspended material, making them more robust for further device fabrication.

Third attempts for shadow masks of contact fabrication were much more successful. A window with removed SiN was held by double side tape under a stereoscope while tiny pieces of Kapton or carbon tape were affixed to the face of the SiO_2. A length of 20 μm pure tungsten wire was affixed across the window with the tape on the SiO_2, as in Figure A.5. This window was then ready to use on a large piece of monolayer graphene.

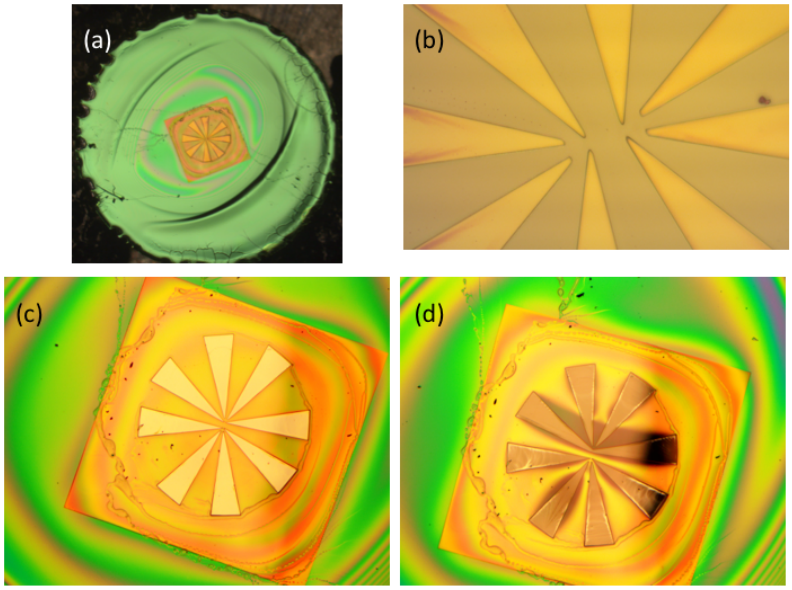

Figure A.4: (a) A polymer coated SiN window with electron beam pattern for 8 contacts, (b) the contacts are in a hall-bar-like shape, (c) after a 1:45 CF_4 etch the uncovered SiN is not completely etched away, and (d) after 2:15, the etch has broken through and shorted 2 contacts.

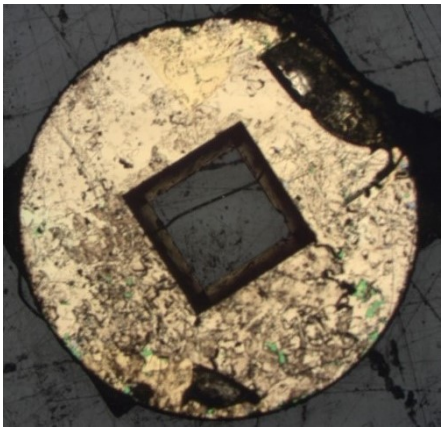

Figure A.5: A 2-contact shadow mask custom-made from a broken SiN window and a 20 μm tungsten wire.

A wafer with a usable graphene flake was affixed to a custom-built aluminum mounting plate with mask-holding spring clamps, shown in Figure A.6. The proper alignment required that the wafer with graphene was placed under the clamp such that the SiN window would be held by the clamp over the graphene. Under the stereoscope, the mask was flipped so the wire was facing the graphene wafer and roughly aligned to the position of the graphene and placed under the clamp.

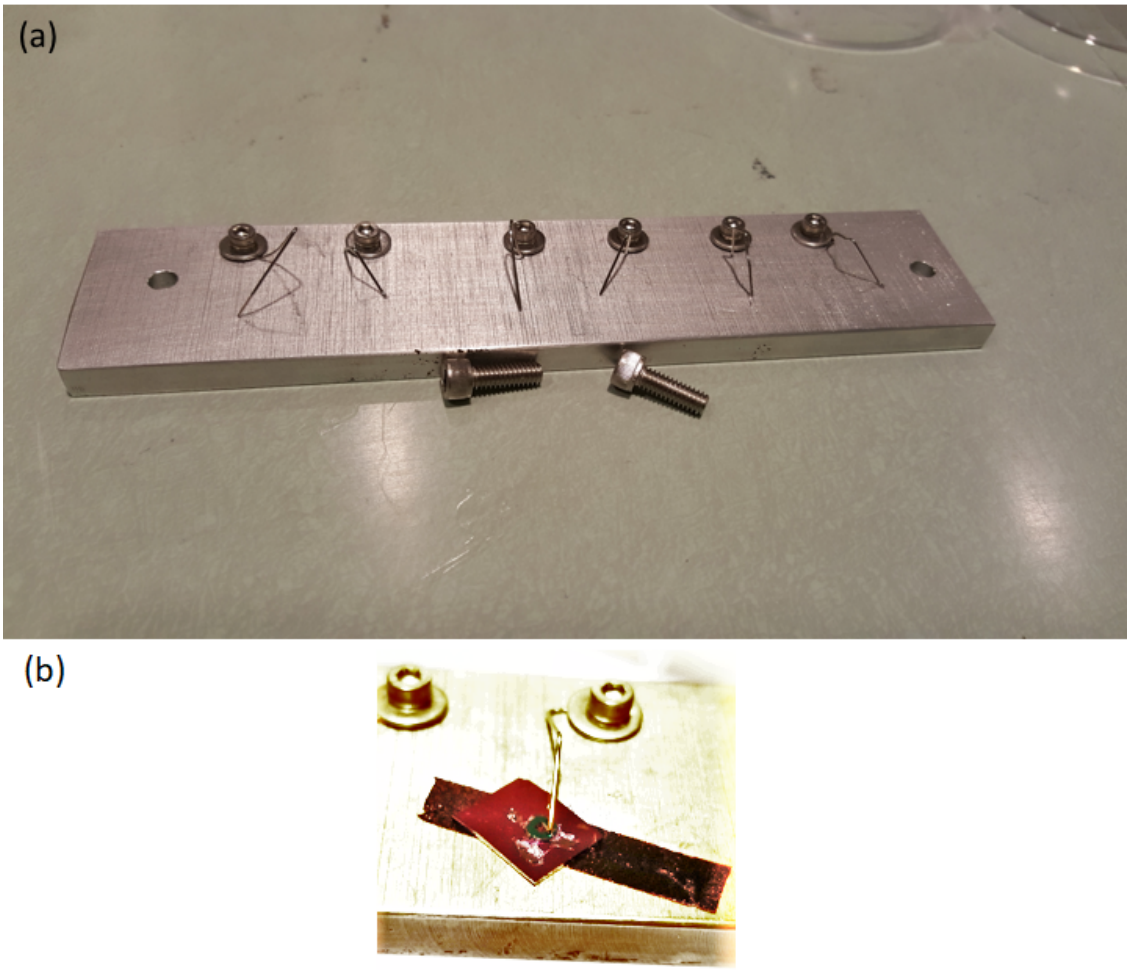

Figure A.6: (a) Custom-built aluminum mounting stage for shadow mask evaporation and (b) a high contrast photo of a wafer aligned under clamped shadow mask, ready for metallic evaporation

Next, the entire mount was then transferred to the higher magnification probe station, shown in Figure A.7. At this point, the process of aligning the shadow mask over the graphene becomes iterative. While looking through the microscope at $\times 25$ magnification, the tweezers are brought into brief contact with the SiO_2 body of the mask. Brief taps along appropriate sides align the wire such that it will cover the center of the graphene and evaporated metal will cover each end of the graphene. These taps and shifts with the tweezers also may need to be balanced by lifting and replacing the clamp to also for equilibration of any tension in the clamp cause by pushing, pulling, or rotating the mask. After many iterations, the mask should be as best aligned as possible. One final step before loading into the evaporator is a flip of the entire stage upside-down. This is to simulate the flipping that will occur to load into the Edwards 306 thermal evaporator.

After flipping, it is appropriate and necessary to examine the alignment in the probe station. With enough iterations of the clamp equilibration, the flipping usually does not cause enough shift in the alignment to warrant further alignment. But in the case of a loose clamp or a clamp not well equilibrated, several micron shifts may occur and need to be fixed.

Figure A.7: Probe station used for fine alignment of shadow masks over the graphene flake.

Some other work at shadow masking involves improvements on the 2-contact method discussed above. Instead of a single wire across the window, two wires are arranged at a 90° angle from each other to form 4 contacts, as shown in Figure A.8. Or, when graphite pieces near the monolayer would short together two or more of the metal contacts, then the angle between the 2 tungsten wires may not have been arranged at 90°. Other angles are also sufficient for masking four metallic contacts into an arrangement suitable for wire bonding. In addition, we briefly tried replacing the 20 μm tungsten wires with variable thickness glass threads. Because of the fragility of glass, this did not work. During the alignment steps, the SiO_2 body of the mask rests on the wire(s) and those wires may shift or roll during the alignment. Because of the tape at the edges of the wires, the graphene is mostly safe from being touched by the wires (we lost maybe one of twenty-five devices this way), but the rolling and shifting easily shattered the glass threads.

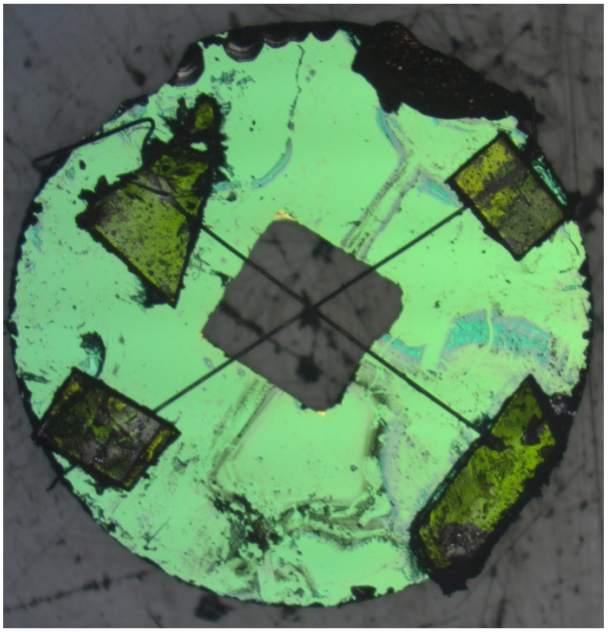

Figure A.8: A 4-contact shadow mask made via two tungsten wires on a broken SiN window.

A final methodology of shadow masking adapted for metallic contacts on graphene is the

TEM grid alignment process used by Tien *et al.* [131]. Similar to the 4-contact tungsten wire mask created above, a 3 mm TEM grid is attached by microscopic pieces of carbon tape to the surface of a broken SiN window. The piece is then mounted onto a piece of polydimethylsiloxane (PDMS) onto the stage of the transfer station. A probe needle typically used for contact checking is carefully inserted into one of the holes near the center of the grid. Once the needle pushes into the PDMS, it is through the grid hole. The PDMS keeps the tip of the needle from being scratched on the brass surface of the probe station stage, also custom built and installed, pictured in Figure A.9. Once the needle is inside the TEM grid hole, a micro-manipulator is used to pull the needle through several holes of the grid, breaking the squares and merging them into a long rectangular contact. The needle is raised and the grid is rotated 180°. The process is repeated for the next TEM grid hole. If this is to be done for a 4-contact mask, then another rotation of 90°, then a rip step, followed by a rotation of 180°, and a final rip step completes the mask. See Figure A.10 for a final mask photo.

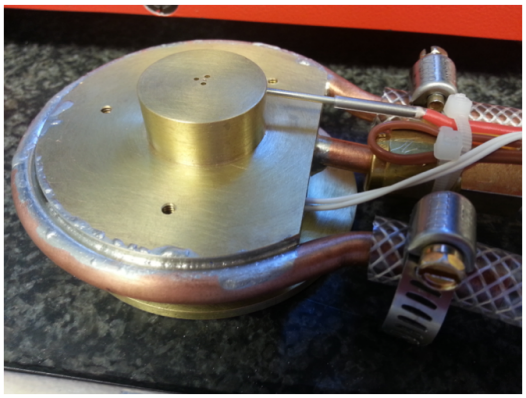

Figure A.9: The custom designed probe station stage includes a plug heater controlled by an Omega PID Controller, a water cooling system via copper tubing, vacuum holes for holding of wafers on the central column, a thermocouple below the vacuum holes, and an adjustable height base.

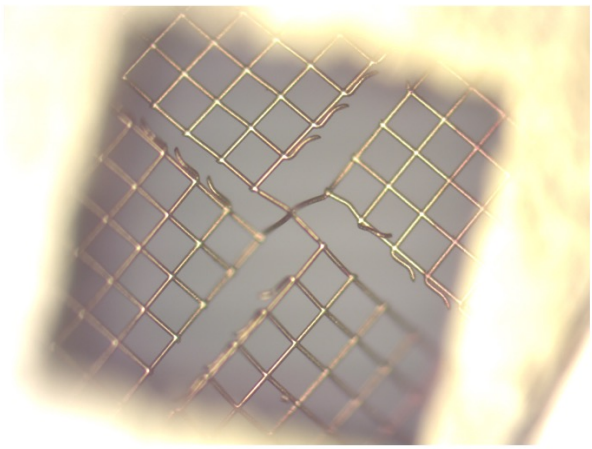

Figure A.10: A final TEM grid shadow mask

After the TEM grid mask is complete, the process for aligning and evaporating onto a graphene flake is the same as it would be for a 2-contact or 4-contact mask designed by suspended tungsten wires. See Figure A.11 for a sampling of devices made by the shadow mask methods described.

While shadow-masking is a useful tool for fabricating devices with minimal contamination due to fabrication residues, it is limited by several factors. First, shadow mask devices are limited by the size of the achievable mask. In the case of suspended tungsten wire mask, the minimum usable graphene flake size is 10 μm $\times$ 30μm for a good 2-contact mask alignment or 40 μm $\times$ 40 μm for a good 4-contact mask alignment. Indeed, commercial wire drawing companies sell wires drawn down to 10 μm in diameter, but that only improves the usable graphene flake size by a factor of two, which is easily achievable by switching to TEM grid masks.

TEM grid shadow masks are less limited by size with the bar widths around 10 μm requiring that graphene dimensions be only greater than 20 μm for a good alignment. However, many large area graphene flakes are approximately rectangular in nature, with 10-20 μm on one side and perhaps a much larger edge along the perpendicular side. As seen in

Figure A.11(d) or (e), this could cause lack of contact in the case of even a small shift in the alignment, whether that shift occurs during transport, loading into the evaporator, or during pump down of the evaporator. Smaller bar widths are available to around 5 μm, but those size changes are balanced by a decrease in hole size as well. This hole size decrease would further complicate the mask creation via probe needle ripping. In fact, at 8-10 μm bar width, the creation of the mask is intricately sensitive, with a high probability of destroying the mask occurring at the second, third, and fourth contact rip steps. Decreasing the bar width could further decrease the structural integrity during these rip steps.

In addition, shadow mask devices created by the suspended wire or TEM grid method are limited in the number of contacts available, which limits the ability to perform certain measurements. For example, the device made for Figure A.11 (a) and (b) could not obtain an R_{xy} measurement.

Finally, the bulk of the adatom and nanoparticle project depends upon observing the Dirac peak behavior of graphene as adatoms or nanoparticles are added to the graphene. These adatoms either electron dope or hole dope the graphene. Because shadow-masked graphene tends to have a Dirac peak far to the hole side of charge neutrality, adatoms that hole dope will more quickly remove the peak from the viewable gate range. For this reason, shadow mask devices are not practical for Os adatoms.

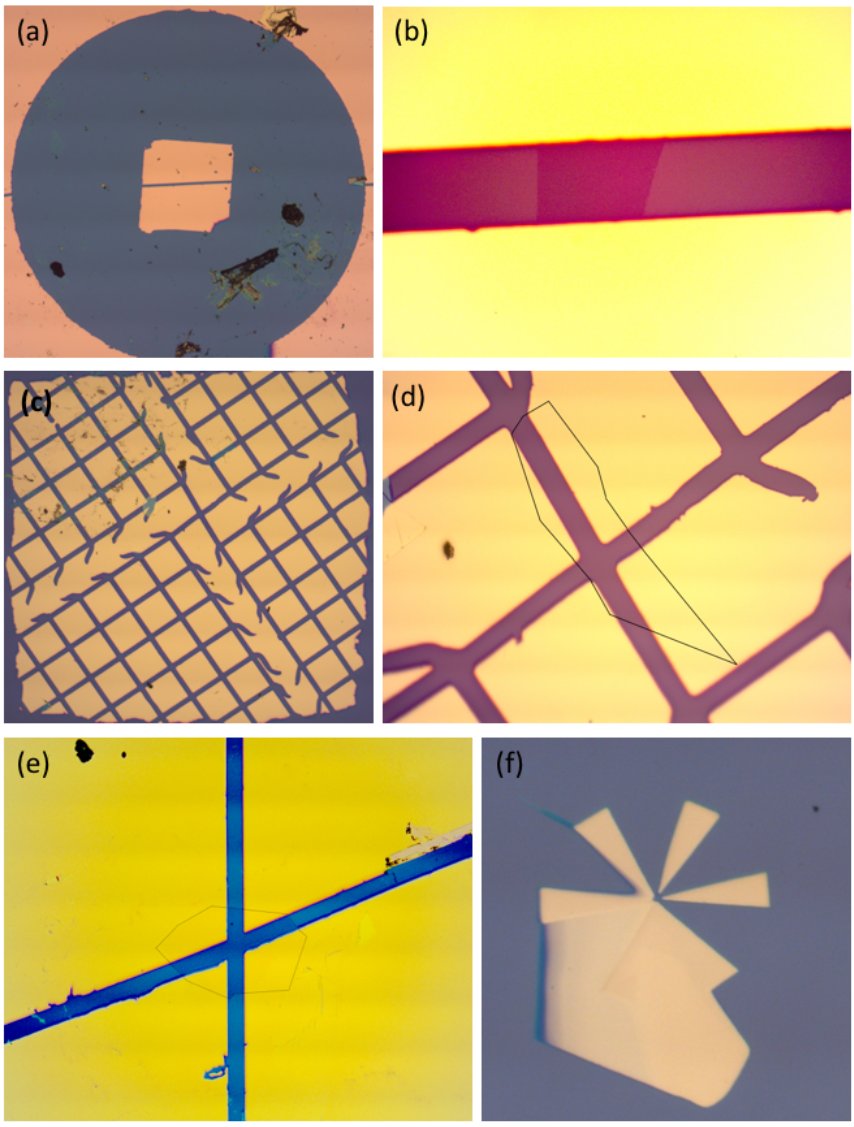

Figure A.11: Fabricated shadow-mask devices: (a)-(b) low and high magnifications of final 2-contact device via suspended tungsten wire and (c)-(d) low and high magnifications of final device contacted via TEM grid shadow mask. (e) A 4-contact device fabricated by a supervised undergraduate with the two-suspended-wire mask and (f) an attempt to evaporate metal through a lithograpy/etched SiN window mask where 4 of the contacts shorted together. The graphene flake is outlined in black in (d)-(e).

A.4 Focused ion beam contacts

Another method of attaching contacts directly to graphene is by using a focused ion beam (FIB) to directly place platinum leads onto the graphene. Unfortunately, this requires a precursor gas that could also contaminate the graphene. Presumably, the amounts of the precursor gas reaching the graphene flake exponentially drop off farther from the platinum lead. So, if the leads are far enough apart, effects due to this cloud of contaminants should be minimized. However, one important measurement for proving the presence of edge channels in graphene with a Kane-Male Hamiltonian, is a non-local voltage. And due to scattering effects, these edge channels tend to only be measurable on the order of 2 μm or less distance between the contacts.

This method was briefly attempted in two devices. In the first, a cloud of contamination was visible around each contact. Furthermore, the contact resistances were extremely large. It is possible that contaminants from the precursor gas cause high resistance contacts in FIB-made platinum leads [132]. While these resistances may improve by annealing after platinum deposition, a second device attempt failed via a malfunction in the software which caused the FIB to open the precursor gas valve unexpectedly and burn contaminants onto the wafer. Both devices are shown in Figure A.12.

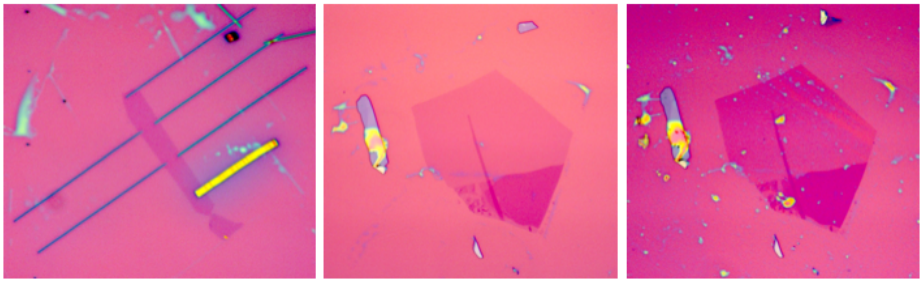

Figure A.12: (a) A device with FIB contacts and visible contamination cloud around the large contact, (b) a graphene device before attempting FIB contacts, and (c) the same graphene device after a software malfunction. All three photos are in false color for enhanced contrast.

A.5 Lithographic contacts

Probably the most commonly used method of applying contacts to a graphene device is some form of lithography. Lithography is significantly less limited by the size of the device; an SEM with NPGS and DesignCAD may have a reasonable writing resolution on the order of 10-50 nm, depending on the particular alignment and focusing achieved. In most cases, lithography is more likely to be limited by the maximum size of the write. For example, it might be more difficult to write large patterns of alignment marks or bond pads around a graphene flake than it would be to write a contact pattern much smaller than a standard shadow mask described previously. The steps to contact graphene by electron beam lithography are as follows:

1. Spin electron beam resist onto flake
2. Measure location of flake
3. Use electron beam to draw alignment marks around the graphene flake
4. Develop the alignment mark pattern
5. Design the pattern of contacts to the flake
6. Use electron beam to write the designed pattern
7. Develop the pattern
8. Evaporate metal
9. Remove the polymer resist.

An optional step to ozone clean the contact areas may occur before the evaporation step and has been shown not to harm the graphene and possibly to decrease contact resistances for cleanings up to 9 minutes.

A.5.1 Spin coating procedures

After an exfoliated flake has been found in an optical microscope and imaged at several magnifications, polymer resist was spun on the device. The graphene wafer was pre-baked at 150° C to 180° C for 3-5 minutes to remove water and adsorbed contaminants. The wafer is aligned to the center of the spin coater and a few drops of Poly(methyl methacrylate) 495 A4, also called PMMA, commercially purchased in 500 mL quantities, are distributed by sterile dropper onto the wafer. The wafer is spun at 4000 rpm with maximum ramp rate which creates a layer of about 200 nm thickness. A postbake at the same temperature and time as the pre-bake is done for hardening of the film. The process is repeated for another layer of PMMA 495 and a final layer of PMMA 950 A4. This bilayer 495, monolayer 950 polymer should give a large undercut due to back-scattering and the lower chemical density of the PMMA 495 than PMMA 950. This will improve metal liftoff after the contact evaporation step. The final postbake also occurs at the same temperature and time as the previous layers. The higher temperature and longer time ranges for this process are a result of some experimentation to find what layers are least susceptible to cracking in the PMMA during development procedures. The standard of 150° C for 3 min was not sufficient for some devices. In addition, slower developments in milder solutions also reduced the likelihood of cracking in the patterned PMMA. Furthermore, rounding the edges of metal contacts on the graphene decreased the likelihood that cracks in the PMMA would short two or more of the contacts together.

A.5.2 Location of flake procedures

After the wafer has been sufficiently coated in electron beam resist, it is necessary to know the precise location of the graphene flake with respect to some known value on the wafer. For devices fabricated for this manuscript, the known value was a corner of the wafer.

The horizontal and vertical distances to this corner are measured on the optical microscope at a magnification of ×2.5 which has the largest field of view.

A.5.3 Electron beam lithography

Lithography can be done with either a positive or negative polymer resist. Both use a beam of electrons aimed at specific locations on the device wafer to break bonds of the polymer resist. For PMMA lithography, the electron beam exposes the regions where the bonds are broken and the PMMA in the exposed regions will be removed by a development process. We used a JEOL scanning electron microscope (SEM) equipped with DesignCAD and Nanometer Pattern Generation System (NPGS). Depending on the details of focusing and alignment, the pattern writing may differ minutely but should occur approximately as follows: first there is a rough alignment of the aperture and a rough focusing step. Then the beam current is measured and adjusted using a Faraday cup. The wafer is viewed with the electron beam far from the graphene flake and fine alignment is done. Fine focusing is done on a piece of dust near but not directly on the graphene. After focusing, the SEM should be moved to the origin of the designed pattern and NPGS allowed to take control over the writing portion. Typical settings for an alignment mark pattern are: 2 mm × 2 mm pattern with rulers and 100 μm separation between marks, working distance 40 mm, magnification ×50, beam current 1000 pA, and exposure 700 μC/cm^2. It is preferable to write alignment marks at lower working distance. Unfortunately, the SEM used for this work was outfitted with a low vacuum aperture that deflected percentages of the beam current and caused bending of patterns at low magnifications which is necessary for large patterns such as these. This is shown in Figure A.13. A large alignment mark pattern must be written at a long working distance in order to avoid the bending of the alignment marks, which later caused shifting in the final location of the written contacts. With shifts up to 2-3 μm and small graphene flakes, this caused misalignment on many devices.

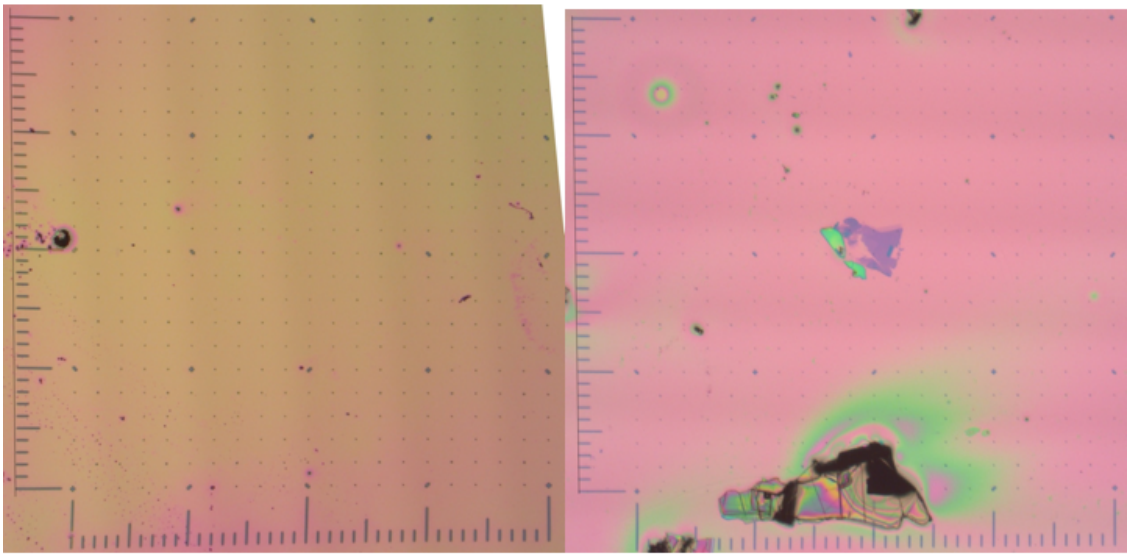

Figure A.13: (a) With a working distance of 25 mm, the alignment mark pattern is skewed near the edges such that alignment will not be perfect even when the procedures are followed carefully. This can be seen in the black line on the leftmost rulers. The line matches the left side of the rulers on the top and the bottom but does not line up with the left side of the rulers near the middle. In (b), written at WD 40 mm, every ruler in the left-hand set is appropriately lined up to the black marking line.

A.5.4 Development

The process of writing an electron-beam pattern exposes known regions to an electron beam and breaking the chemical bonds of the polymer resist at those locations. Developing solution chemically removes only the PMMA with bonds broken by the lithography. To develop the newly written pattern, several variations of the same process may be done. The graphene wafer may be dipped in a room temperature beaker of Methyl isobutyl ketone in isopropanol (MIBK in IPA) 1:3 solution for 30 seconds followed by a quick dip in IPA and dry with N2 gas. This is an aggressive development process and is likely all that is

necessary for most lithography processes. However, in the case of thicker material (such as heterostructures of graphene and boron nitride), a slower process may become more useful. For devices in this manuscript, a 90 second soak in refrigerated IPA:DI water 1:3 solution was sufficient to fully develop patterns and restrict cracking of PMMA to the rarest of cases [133].

A.5.5 Photo editing and pattern designing

Photos from an optical microscope of the graphene with alignment marks are not completely rectangular. While the photo output of the software is rectangular, there is some stretching due to the round nature of the lenses. We use Serif photo editing software to correct the rounded images. First, we load the images as taken by the optical microscope software. Usually, the ×50 magnification image is the most important. This is the image that shows the graphene in best detail while fully including the four alignment marks surrounding the graphene. Next, we rotate the images so they are in the exact orientation of the DesignCAD alignment mark file. Then, we crop the ×50 image so that only the graphene and the 4 closest alignment marks are present. We load an image from DesignCAD of the particular alignment marks around the graphene device. Details may be specific to the version of DesignCAD being used but typically it involves locating the correct marks, zooming in until they take up most of the screen, turning all other layers invisible, and saving an image. Once open in Serif software, the standard alignment mark image must have its background removed; in DesginCAD21 this background is black, as seen in Figure A.14(b). Using Serif's flood eraser tool and quickly clicking on any part of the image that is not an alignment mark quickly deletes the background. Next, that image must be copied as a second layer into the real ×50 image of the device. Selecting only that layer and the resize tool, the standard marks may now be resized to the appropriate dimensions for that photograph. Holding shift retains the aspect ratio. After the size is correct, the real photo

needs to be warped to fit the standard marks. After selecting the layer with the real photo of the device, choose the mesh warp tool, and delete the center point. Now, the 4 edges of the photo maybe be dragged around until the alignment marks in the real photo match the standard set, as in Figure A.14(a). Finally, all layers must be merged and the file saved as an image file that can be read in DesignCAD (such as a .jpeg file).

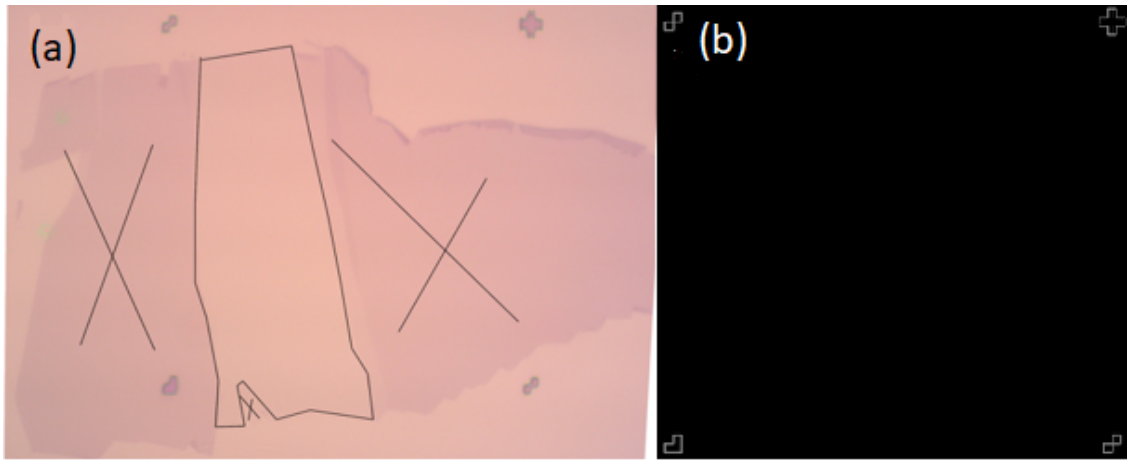

Figure A.14: (a) A meshed image of a graphene flake with four surrounding alignment marks written in PMMA and (b) the standard mark image. The monolayer graphene region is outlined in black and the bilayer regions are crossed out with black X's.

Typically, it is enough to do mesh warping on the ×50 photo. The lower magnification photos ought to be rotated but it is unnecessary to mesh or warp them. In addition, it is often helpful to use the photo editing software to draw an outline around the boundary of the graphene flake. This is because the photos may lose quality when imported into DesignCAD and the graphene is easier to locate when zoomed out if an outline is present.

The ×50 mesh-warped image is loaded using the DesignCAD image load function. It should then be resized and relocated to the correct location of the graphene flake on the alignment mark pattern. The patterns used correspond to a layer of small "inner wires" and larger "outer wires" that connect the inner wires to bond pads. These bond pads are used for

making electrical contact via wire bonding or indium soldering and are typically squares or rectangles about 100-200 μm per side. Inner wires are the smallest width of wire applicable to the device, usually 0.5-2.5 μm. Outer wires overlap the inner wires to correct for shifts of the beam over time and are usually about the size of the inner wire at their connection to the inner wire and widen to 10-30 μm at the bond pad connection. Extra layers of new alignment marks or hall-bar etch patterns may be relevant for particular devices. Every pattern will have alignment window layers which are used for manual alignment of the SEM to the graphene pattern and location. Figure A.15 is a screenshot of an example pattern at low magnification and high magnification.

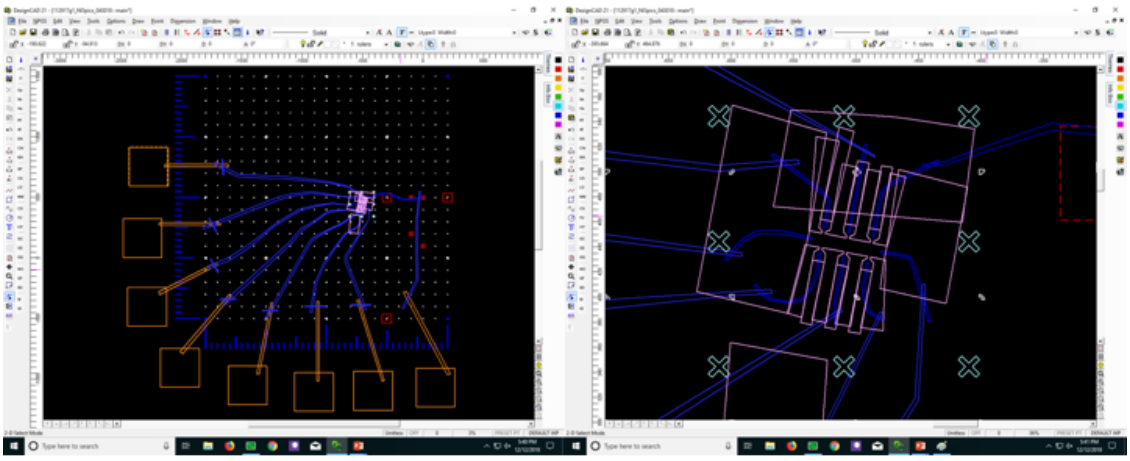

Figure A.15: Screenshots of an example pattern with inner wires, outer wires, bond pads, and an etch-mask at (a) low magnification and (b) high magnification.

A.5.6 Writing contact patterns

Contact patterns vary widely depending on the device but are usually written at working distance 25 mm, with beam currents of 100-300 pA for small features (inner wires) and up to 2800 pA for large features (bond pads). The same alignment and focusing steps as during the alignment mark pattern are necessary. Instead of the graphene flake being the origin

of the pattern, a nearby alignment mark will suffice. The wafer should be rotated so that the alignment mark pattern is correctly oriented according to the design file. The origin alignment mark is the starting point for the manual alignment method of the run file. Each alignment window is aligned over the mark designated in the design file roughly and the user moves a cursor to precisely update the alignment. Several iterations of this process are normal. This process updates the write file in the computer with correct locations for each point that the electron beam will expose or not expose.

A.5.7 Development of contact pattern

The contact pattern development process is identical to the alignment mark development process. This step may be more critical in producing patterns without cracks in the PMMA.

A.5.8 Evaporation of contact metal

Standard metallic contacts on graphene consist of a 3-5 nm sticky layer, typically Ti or Cr, and a thicker conductive layer, usually Al or Au. For the purposes of the adatom project, Cr/Au contacts were almost exclusively used. These contacts can be evaporated in a thermal evaporator with base pressure below 2×10^{-6} mbar.

For Cr/Au contacts made via thermal evaporation, we used the Edwards Auto 306 evaporator system, shown in Figure A.16. The system is kept under vacuum when not in use. When a device or batch of devices is ready for evaporation, the chamber is vented. This function isolates the pumps from the evaporation chamber and purges the chamber with N_2 gas until atmospheric pressure is reached. While the chamber is venting, the sample(s) may be loaded onto the evaporation stage. There are many equivalent ways of doing this including but not limited to: clamping to individual mounting systems or foil wrapping the internal stage and using double-sided vacuum-friendly tape such as Kapton. Lithographic

contacts fabricated for this document were almost exclusively evaporated by clamping the sample wafers to the universal stage mount shown in Figure A.17.

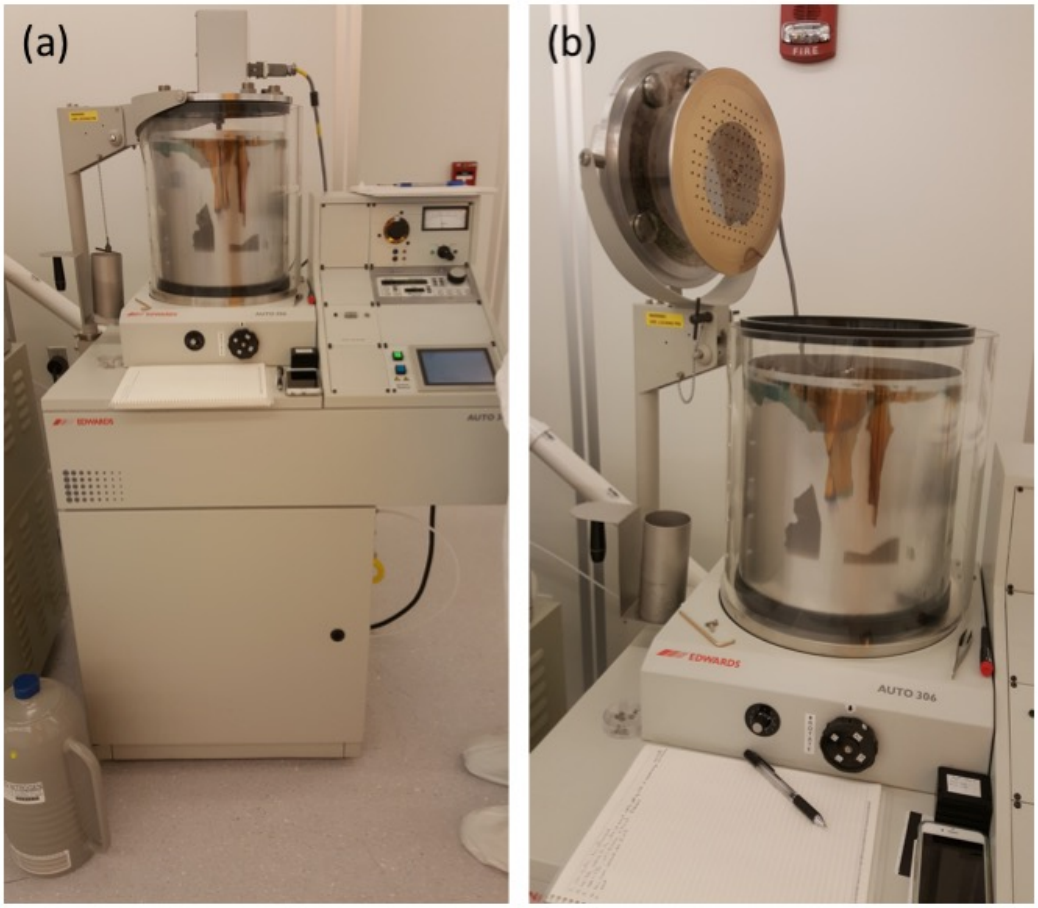

Figure A.16: The Edwards Auto 306 evaporator (a) while under vacuum and (b) opened to air after venting.

Figure A.17: Universal sample mount with large clamps and small washers for holding device wafers

Once the sample wafers are loaded to the mounting stage, the stage must be affixed to the lid of the evaporator. Both the shadow-mask stage and the universal stage mount are equipped with designated screw holes that match tapped holes in the lid of the evaporator. After the devices are ready, the evaporation sources must also be loaded into the chamber. Chromium coated rods are loaded to source location 1, or 1 and 2 if the 1st rod is nearly empty, and tungsten boats filled with gold shot are loaded to source locations 3-4, or 2-4 if thick gold film is required. The 306 evaporator has the ability to store many material property parameters for different metals. The settings used for Cr are: density of 7.20g/cm^3 and z-factor 0.31. And the settings for Au are density 19.28 g/cm^3 with a z-factor of 0.38. To evaporate a metal, the correct source location is rotated into the power supply and the program is chosen. This loads the material properties so the crystal oscillator can correctly measure the thickness of film evaporated. Then a 3 hour pump down is initiated; this will bring the chamber to around 2×10^{-6} mbar. At this point, it is prudent to retrieve a 4 L dewar of liquid nitrogen.

Once the evaporator has reached base pressure, the attached dewar for liquid nitrogen

is filled with liquid nitrogen from the 4 L dewar retrieved during pumpdown. This liquid nitrogen enhances base pressure of the evaporator chamber by cooling and supporting the pumping. Filling of the liquid nitrogen dewar should be done at least directly before the evaporation is done but may also be done at the beginning of a pumpdown to increase pumping efficiency.

When starting an evaporation, it is important to ensure that the shutter is closed, in the position located directly above the source material. This prevents material from being deposited on the sample until the user is ready. For example, new Cr rods are coated in a layer of plastic; it is important to shutter a new Cr rod from the device until the plastic has been evaporated off and the chamber pressure reduced to base again. In addition, Cr and Ti will also decrease the chamber pressure by bonding with oxygen molecules left behind in the chamber. These metals are so-called "getters." The chamber pressure is improved by a Cr or Ti pre-evaporation done with the shutter closed. The pre-evaporation is done by first turning on the power supply and pushing a current from one side of the rod or boat to ground on the other side. This rapidly heats the rod or boat and the evaporation source will begin to melt and eventually evaporate. See Figure A.18.

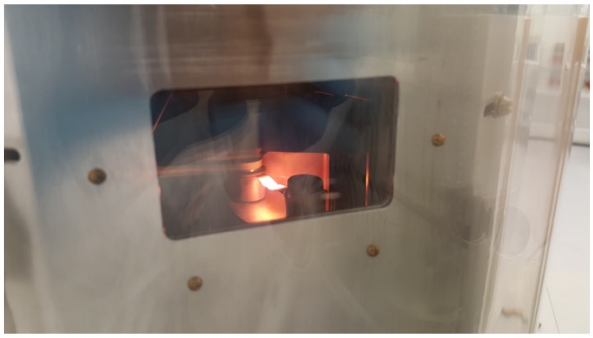

Figure A.18: A glowing tungsten boat with gold source inside

The evaporation of metal becomes obvious not only by the glowing source but also by the evaporation rate reading a non-zero value. During the pre-evaporation, after the base

pressure has lowered to a reasonable value, the sticky-layer evaporation may be done by only opening the shutter until 3-5 nm of Cr or Ti has been evaporated. The current is then turned to 0 A and the source switched to the conductive layer (gold). The program must also be switched in order for the crystal oscillator to correctly track the film thickness. The evaporation process is repeated with no need for pre-evaporation. This time, the shutter may be opened as soon as a rate greater than 0.5 Å/s is reached. Once, the desired thickness has been reached, the current may be zeroed. The chamber is vented and the devices and sources are removed.

A.5.9 Liftoff

To remove polymer resist and excess metal film, the wafer is loaded into a low profile petri dish and covered in acetone. The dish is placed on a hot plate at 50° C for 1 hour with a lid to prevent full evaporation of the acetone. After an hour, much of the metal film will be floating in the acetone and can be carefully removed with tweezers or a toothpick. While still inside the acetone and under a stereoscope or long working-distance microscope, the device should be inspected for areas where the metal film has connected the device contacts or contact pads. If the area that is connected is large and far away from the device, it may be possible to remove the metal film with tweezers or a toothpick. For obvious reasons, this is not ideal. In addition, it may be necessary to sonicate the wafer for 1-3 seconds in the acetone, spray acetone at the wafer, or aggressively stir the acetone with a plastic dropper. None of these methods is particularly good for the device and often leads to broken contacts or graphene that has rolled up. Sonication has perhaps the lowest probability of destroying the graphene and spraying acetone directly at the wafer seems to have the largest probability of rolling the graphene. After all excess metal has been removed from the wafer surface, the wafer is dipped in isopropanol and dried with N_2 gas.

A.5.10 Hall-bar etching

For devices in which an etch step is necessary, either to remove multilayer graphene connected to the monolayer or to shape the device into a Hall bar, another lithography process must be completed. After the contacts have been evaporated and a successful liftoff has occurred, the device is again spun with polymer resist. In this case, a large undercut is neither necessary nor wanted so a single layer of PMMA 950 A4 will suffice. The alignment marks from the contact evaporation are now in metal on the surface and can be reused. An etch pattern is designed in DesignCAD and lithography and development are completed. The wafer may then be loaded into either a Reactive Ion Etch system (as done for devices in this work) or into an oxygen plasma asher. For an RIE system, with both power 100 W, and gas flow rates of 5 sccm oxygen and 50 sccm argon, several layers are removed within 3 seconds. If thicker material is attached to the graphene or connecting contacts, it may be necessary to do a double layer PMMA resist and oxygen etch for longer. Etches up to 10 seconds have been successfully performed under these conditions.

A.5.11 Graphene Cleaning

It may be prudent to clean residual resist off the surface of the graphene device. Some work has been done with both vacuum annealing and AFM brooming. The effectiveness of these procedures are examined in detail in Appendix B.

Vacuum cleaning processes are typically performed as follows: the device wafer is loaded into the vacuum anneal chamber. Clips are installed for better thermal contact but have not been proven to provide any measurable benefit. The chamber is sealed and pumping begins. Once base pressure is reached, a halogen bulb directly above the chamber stage is turned on by a main power switch controlled by a PID controller. The PID holds the bulb on until the stage temperature reaches 350° C. During this process, water cooling flows through channels

near the outside of the chamber and around the o-ring sealing the chamber door. On/off power to the bulb is controlled via the PID controller set to 350° C which runs continually until main power is disabled. After the device has been at 350° C for either a short (15-30 minute) or long (1-3 hour) anneal, the switch controlling main power is disabled and the chamber begins to cool. Once the temperature has lowered by 10%, the cooling water is switched to a channel under the sample stage. After the stage and chamber has fallen below 50° C, the vacuum is turned off and the chamber vented. The device can then be removed from the chamber. A photograph of this custom-built instrument is shown in Figure A.19.

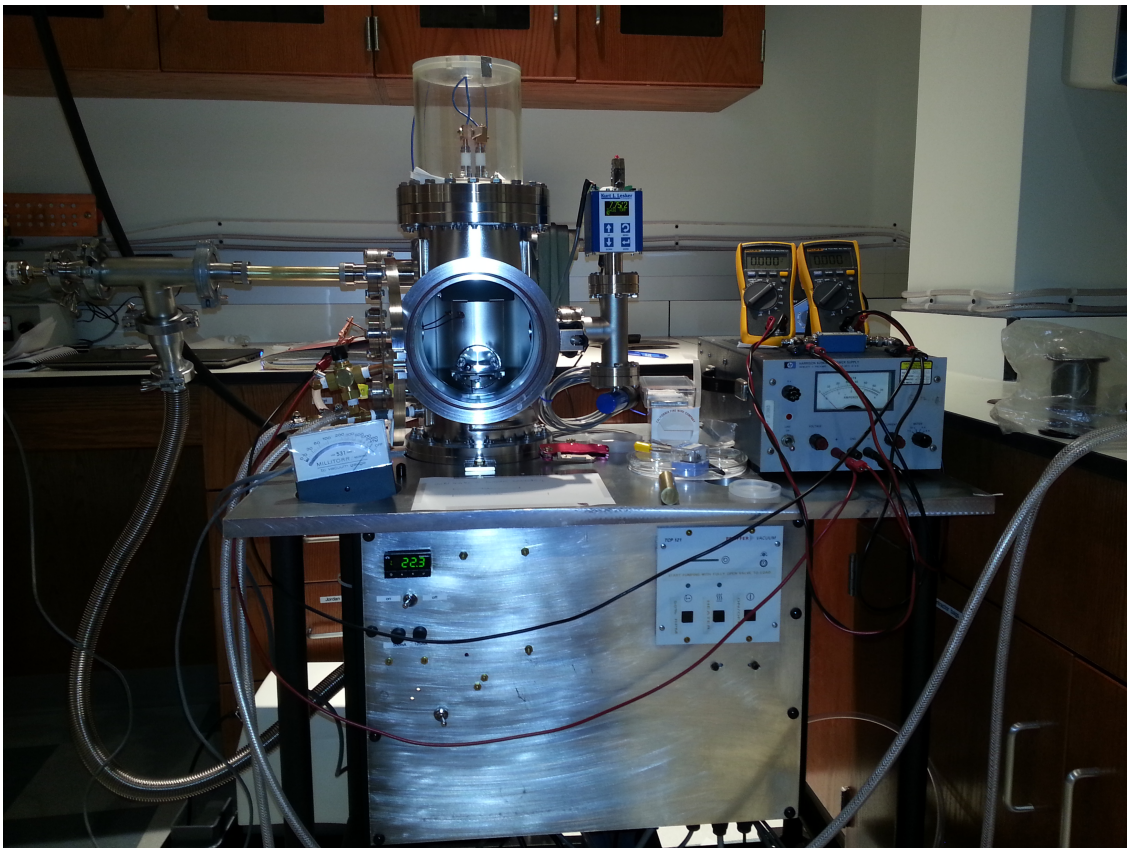

Figure A.19: Front view of the custom-built thermal annealer equipped with rough and turbo pump technologies, PID heat controls, and water cooling.

Another cleaning method used in this work is atomic force microscopy (AFM) brooming.

To properly broom a graphene or other 2D device, one needs an AFM equipped with both tapping and contact mode. The device is first imaged under medium-high resolution (512-1024 lines at 0.5 Hz) in tapping mode. Because of the remnant polymer resist on the surface, the tip is likely to stick in the polymer layer and either cause bad imaging or contaminate the tip. In order to avoid this problem, the tapping tips used need to be of relatively high force constant. We used tips that have a force constant of 19 N/m.

After initial imaging is completed, contact mode AFM tips must be loaded and engaged. Because the tip will now be in contact with the graphene, it is important to have the engagement location as close to the center of the device as possible. The device is rotated to the closest rectangular position and scanned at minimum engage force to identify the brooming region. It has been determined that our devices have large numbers of high resistance (dead) contacts when the tips of the contacts are included in the brooming area. For this reason, we extend the overlap region of the graphene to metal contact and attempt to not broom the contacts as much as possible. After the central location has been chosen and the scan window defined, we increase the force, scan speed, and number of lines. In some AFM software, when scanning a rectangular region, the number of lines may be limited by the number of samples per line and the aspect ratio. In this case, it maybe be necessary to set an excessive number of samples per line in order to achieve the number of lines necessary to properly broom. The optimal parameters for removing PMMA resist from graphene on SiO_2 are 40 nN and 2 Hz with the number of lines being calculated via:

$$n > \frac{w}{d}, \tag{A.1}$$

where n is the number of lines necessary to fully broom the device, w is the width in the direction opposite the scan direction, and d is the minimum diameter of the AFM tip. For example, a rectangular graphene device that is 20 μm in the x-direction and 10 μm in the y-

direction, being scanned along the x-direction with a 2 nm tip would need to be scanned with more than 5000 lines. In a troublesome software, this may require setting the samples per line to be greater than 10,000 samples in order to set the number of lines greater than 5,000. For all devices in this document, AFM brooming was completed with a Bruker Dimension Icon with ScanAsyst, as shown in Figure A.20.

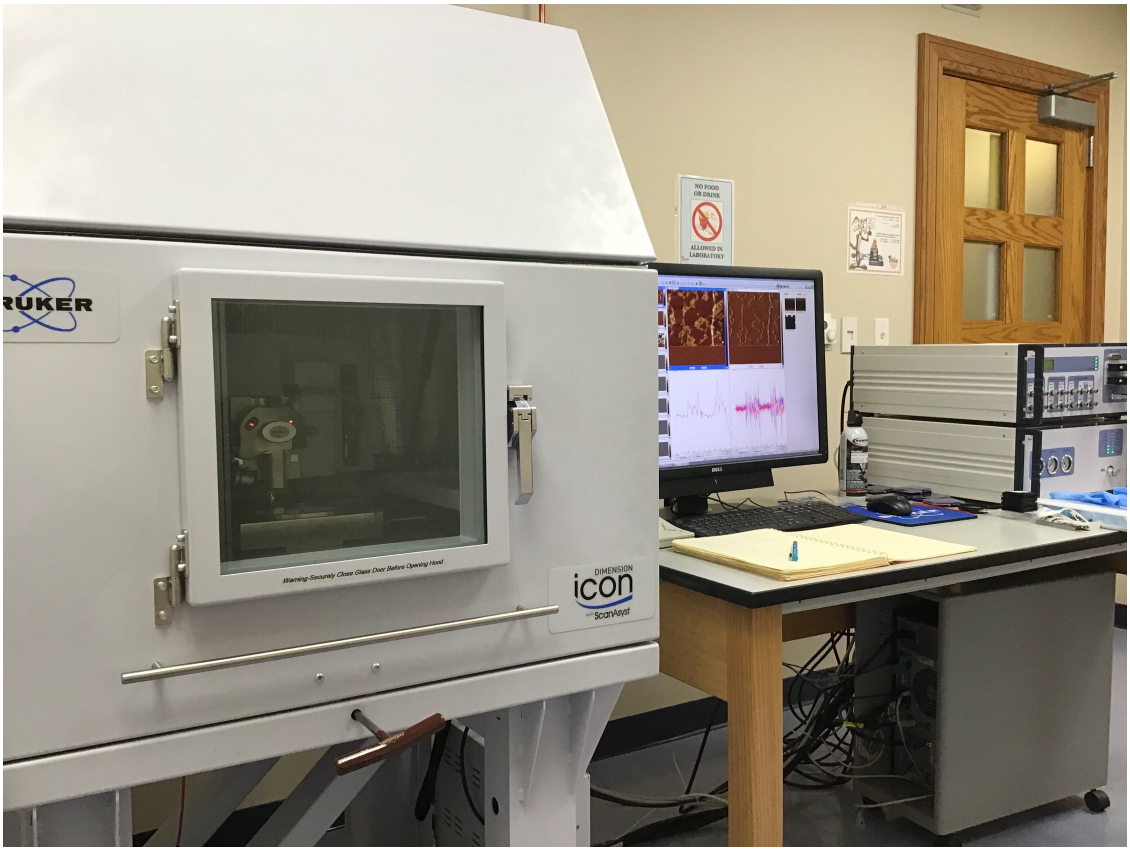

Figure A.20: The Bruker AFM used for the broomed devices in this document was used in collaboration with the Washington University in St. Louis Institute for Materials Science and Engineering.

Appendix B

Graphene cleaning procedures and efficiencies

B.1 Abstract

In this Appendix, we have investigated the effect of multiple cleaning techniques commonly used in standard fabrication of graphene Hall bar devices. Surface roughness measurements were made on graphene flakes before and after standard electron beam lithography for contact deposition and etch masking. While the surface roughnesses measured after AFM brroming are comparable to those measured after vacuum or gas-aided annealing, our results indicate that AFM brooming is a more reliable process for fabricating devices on SiO_2.

B.2 Introduction

There are many ways that have been used to improve graphene surface cleanliness. Cleaning procedures typically include: vacuum annealing [134–139], hydrogen-argon or hydrogen-nitrogen annealing [137, 139, 140], other gas-aided annealing [141], and current-induced

annealing [142, 143]. In addition to cleaning residues off the surface of graphene, annealing has also been shown to decrease (improve) the graphene-metal contact resistance of thin-film contacts [140, 144, 145].

Cleaning methods are necessary because standard fabrication procedures, such as electron beam lithography for contact deposition, leave polymer residues on the surface of the graphene devices. These residues are persistent even through vigorous annealing procedures [123] to the point where the graphene must be damaged in order to remove *almost* all of the residues. Here, we analyze the efficacy of using contact mode atomic force microscopy (AFM) to broom polymer residue off the surface of the device. This technique has been used for high mobility bilayer graphene devices on hexagonal BN [146] as well as for graphene on substrates with high spin-orbit coupling [35] and other 2D measurements where clean surfaces are required [147, 148]. This method has been well-characterized [149, 150]. We use high resolution AFM imaging to measure surface roughnesses after AFM brooming and compare the values to surface roughnesses of exfoliated flakes, flakes where polymer resist PMMA was removed only by acetone soaking, and flakes with PMMA removed by annealing.

B.3 Methods

A Bruker Dimension Icon atomic force microscope (AFM) outfitted with ScanAsyst capabilities was used to measure surface roughnesses of graphene. Due to the inherent stickiness of PMMA residues, it was necessary to use tapping mode with TESPA-V2 tips with force constant 19 N/m to achieve high resolution imaging. The resolution of such tips is about 7 nm. For each AFM image acquired, we used high resolution, scanning graphene devices up to $50\times50\mu$m in area at 0.5 Hz with 1024 lines. For each area measured, we tuned the amplitude such that the highest quality image could be taken.

To analyze the surface roughness of the area scanned, we used Gwyddion to correct

for planar backgrounds, removed anomalies, and zeroed the scale range. Gwyddion surface roughness calculations were taken in a variety of locations but it seemed most reasonable to take the regions that optically *looked* like a usual graphene flake with or without residue. In other words, areas where large cracks, folds, or anomalous dust were seen were ignored during roughness calculations. In addition, we attempted to use self-consistent locations on each flake measured and averaged the results from a few locations per flake.

There are two surface roughness measurements reported in this document: the arithmetical surface roughness and the root mean square (rms) surface roughness. The arithmetical mean height of a surface S_a is defined as the absolute difference between the amplitude of the peaks and valleys compared to the average surface height. The rms height S_q is, on the other hand, the standard deviation of the peak and valley amplitudes. These are shown in the following equations:

$$S_a = \frac{1}{A} \iint_A |Z(x,y)| \, dx \, dy \tag{B.1}$$

$$S_q = \sqrt{\frac{1}{A} \iint_A |Z^2(x,y)| \, dx \, dy}, \tag{B.2}$$

where $Z(x,y)$ is the surface height function.

B.4 Results

In Figure B.1, we present AFM images for as-exfoliated graphene flakes. Clean areas of these flakes have arithmetical mean height roughnesses (S_a) between 135 pm and 170 pm. Further the rms roughness averages (S_q) are between 165 pm and 220 pm. Comparable values were found using Bruker's Nanoscope Analysis software.

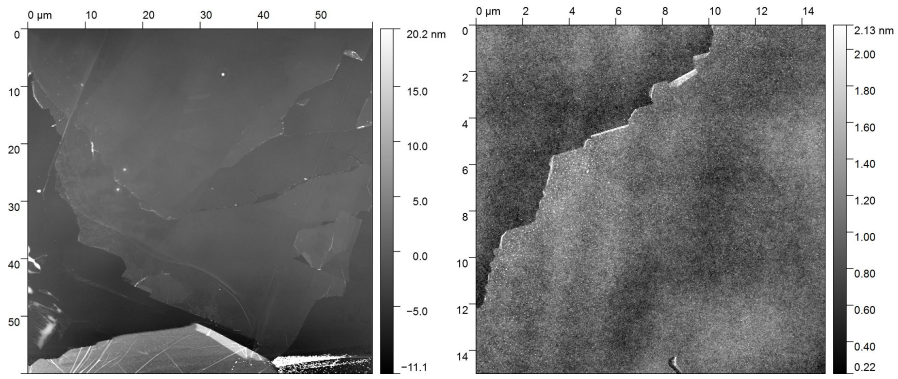

(a) 052918a1

(b) 052918a2

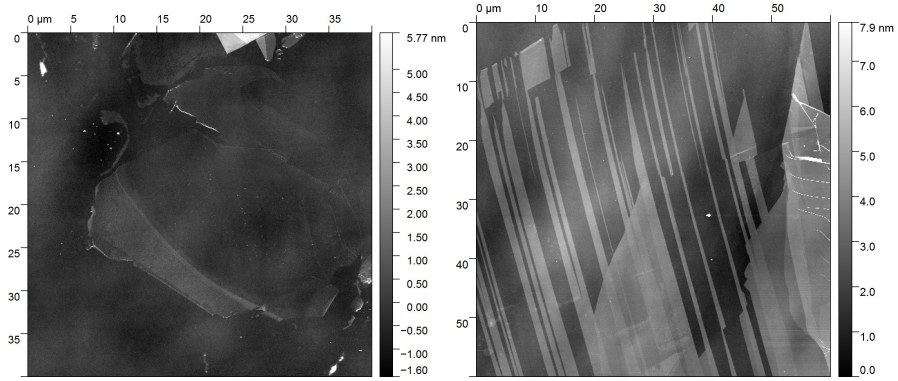

(c) 052918a4

(d) 052918c1

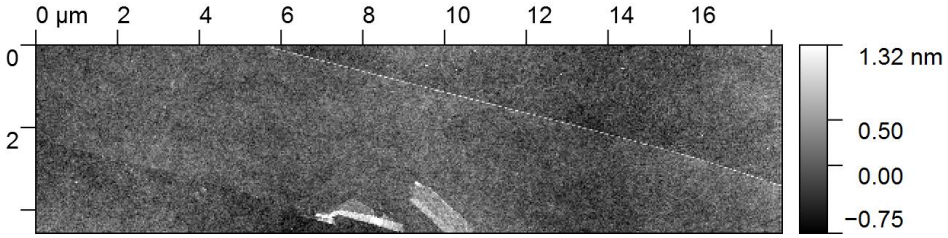

(e) 052918a3

Figure B.1: Examples of processed AFM images of exfoliated graphene flakes named (a) 052918a1, (b) 052918a2, (c) 052918a4, (d) 052918c1, and (e) 052918a3.

Furthermore, one flake with obvious tape residue was recorded and measured. The roughness S_a (S_q) for this flake was around a 114% (108%) increase from the roughness of clean graphene flake 052918a4. This flake is shown in Figure B.2.

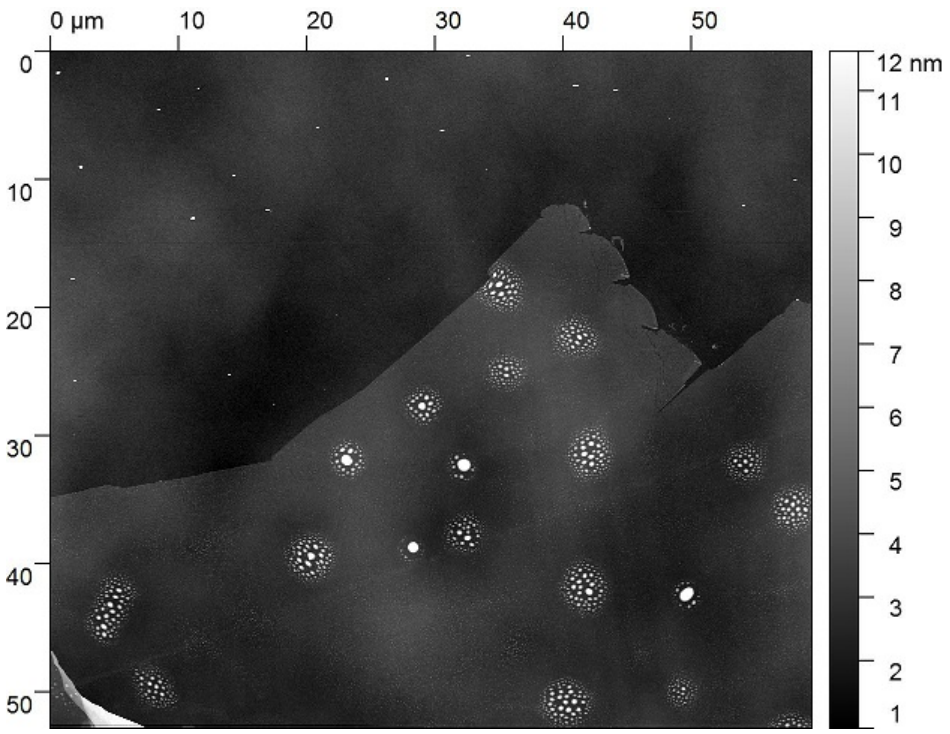

Figure B.2: An exfoliated graphene flake with tape residue confirmed by optical microscopy has higher surface roughness than clean exfoliated graphene.

The first step in cleaning any fabricated graphene device is a liftoff step to remove excess metallic film from the contact evaporation. For PMMA, this process involves a 1 hour soak in acetone. Others have found that chloroform soak instead of acetone improves mobility of graphene devices [135]. We soaked our devices in a low-profile dish of acetone at 50° C for 1 hour or more. AFM images of devices after this processing are shown in Figure B.3. It should be noted that some of these devices were not fully fabricated but instead were spun for lithography and cleaned via acetone without the metal evaporation step.

For devices that had PMMA removed by acetone soaking, the surface roughnesses were as follows: S_a ranged between 450 pm and 1325 pm while S_q ranged between 830 pm and 2200 pm. Obviously, this is a large range, but the images in Figure B.3 show that PMMA forms clusters or islands of varying sizes across the surface of the graphene. In addition, a

fabricated device is included in Figure B.3 for comparison. Clear PMMA islands are also seen on the fabricated device.

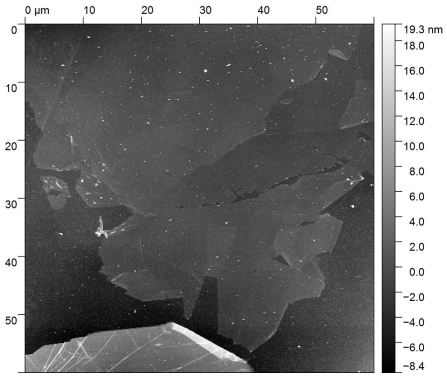

(a) 052918a1

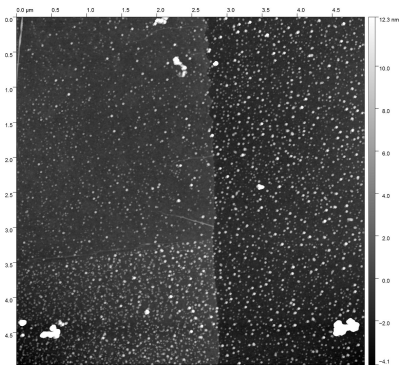

(b) 121517a1

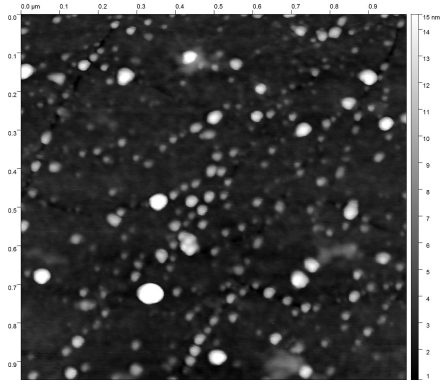

(c) 072117d1

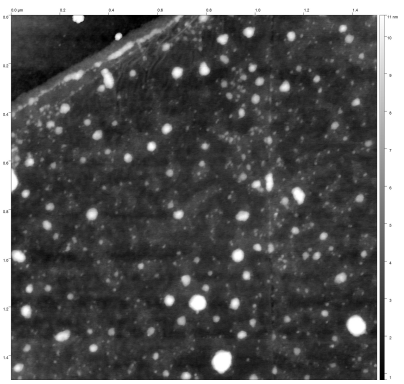

(d) 080417e1

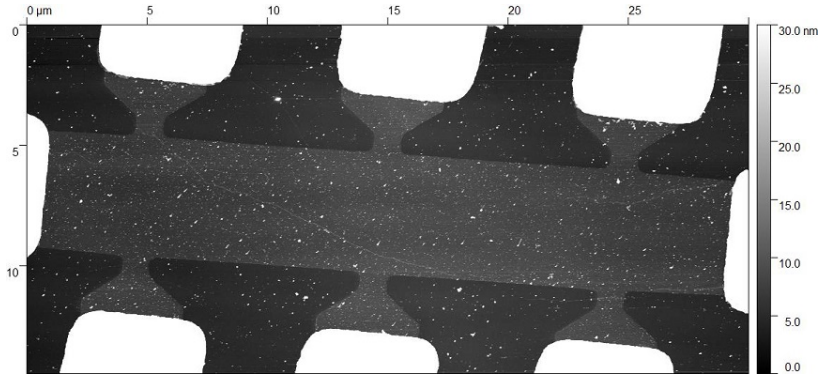

(e) 112917e1

Figure B.3: AFM images of graphene flakes or devices where PMMA was removed via warm acetone soak.

After AFM brooming, the graphene flakes and devices typically look much cleaner in AFM images. Furthermore, there is an obvious boundary where the PMMA piled up at the edges of the broom region. This is shown in Figure B.4. The roughness of well-broomed graphene drop to nearly the original roughness of an exfoliated graphene flake. The roughnesses measured range from 140 pm to 225 pm for arithmetical surface roughness and 185 pm to 300 pm for rms surface roughness. If the flake shows evidence of not being broomed well, such as the flake shown in Figure B.5, the surface roughnesses are higher at around 295 pm for for arithmetical surface roughness and 375 pm for rms surface roughness.

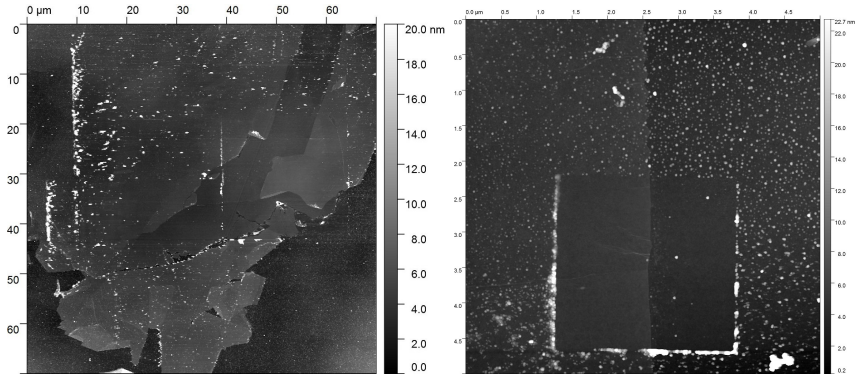

(a) 052918a1 (b) 121517a1

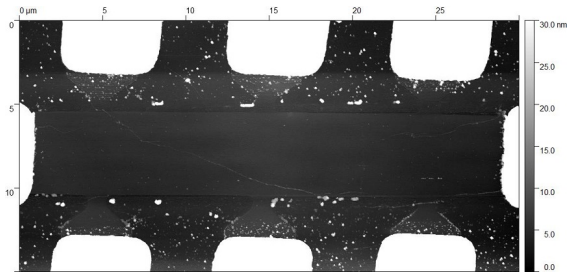

(c) 052918a3

Figure B.4: AFM images of graphene flakes and a graphene device after brooming.

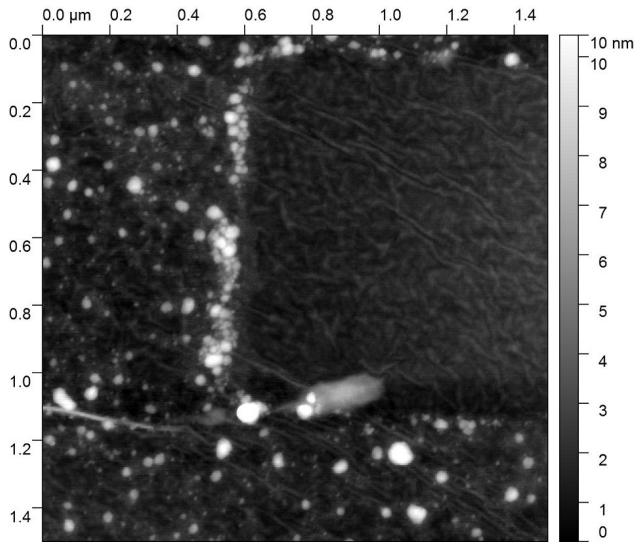

Figure B.5: Occasionally brooming is unsuccessful and the device shows either PMMA islands left behind on the surface, wrinkles or cracks that were previously hidden by the PMMA, or odd smearing effects such as is shown here.

A graphical comparison of the arithmetical surface roughness values is shown in Figure B.6. From this graph, it is obvious that AFM brooming significantly improves the graphene surface. The various markers and names correspond to different samples used in this study.

To compare the efficiency of AFM brooming to other commonly used cleaning methods in graphene, we also studied the surface roughness of graphene after short and long vacuum anneals as well as after gas anneals. For short vacuum anneals, we used the method described in Appendix A.4.11 where a 15 minute anneal was performed in vacuum at 350° C. The surface was then studied via the same AFM tapping mode imaging as was done for other flakes and devices. The surface roughness of devices that underwent short vacuum anneals were low and of similar values to those that were cleaned by AFM brooming. For example, the S_a values for short vacuum annealed devices was between 200 pm and 235 pm.

In order to test methods used by other groups, we also chose to measure the roughness after a few long (>1 hour) vacuum anneals. The surface roughness values for this cleaning

method was similarly low with S_a values from 220 pm to 300 pm. Similarly, other groups have used hydrogen-argon anneal processes to clean graphene devices. We also tried this and measured arithmetical surface roughness values ranging from 150 pm to 210 pm.

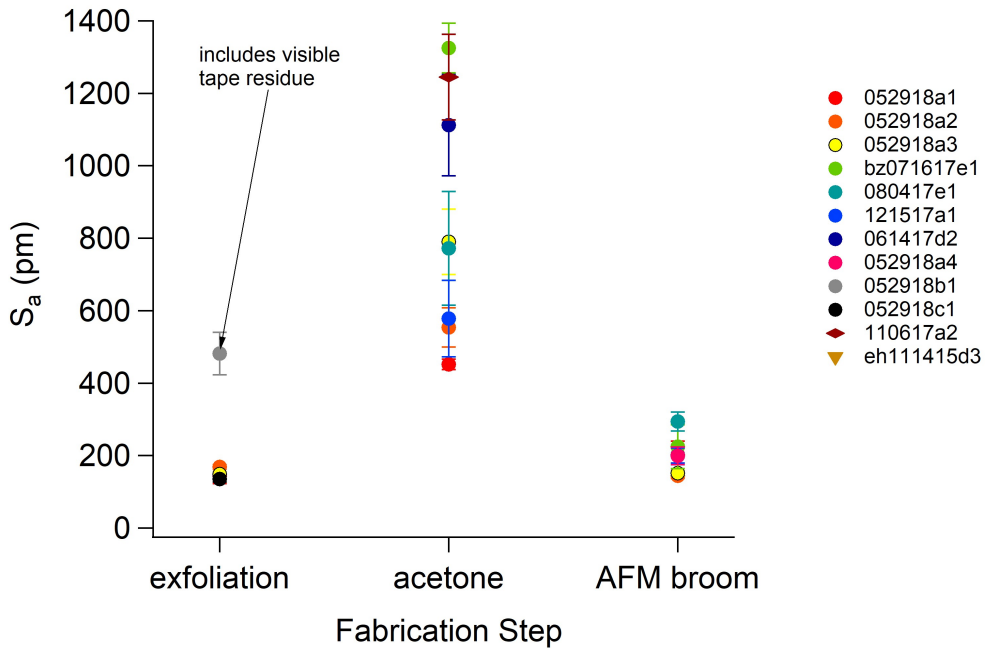

Figure B.6: The arithmetical surface roughness of graphene as-exfoliated, after an acetone soak to remove PMMA, and after AFM brooming.

In similar fashion to Figure B.6, we then present Figure B.7 which chronologically shows device improvement from the acetone step, through an AFM broom step, followed by a 4 hour vacuum anneal. Even the AFM broomed region is no longer obvious after a long vacuum anneal because the thick PMMA boundary has been removed.

However, in all devices that were vacuum annealed, whether for 15 minutes or longer, the graphene mobility has been incredibly low, especially in comparison to other devices fabricated alongside them. For example, in Figure B.8, we see the graphene Dirac peak of a vacuum annealed device. The full width half maximum (FWHM) of the Dirac peak is wide

(more than 40 V as compared to 10 V for standard graphene on SiO_2) and located far from 0 V in gate voltage. This indicates that while the vacuum anneal is removing the PMMA residue from the surface something else is occurring. We propose that regular graphene flakes exfoliated on SiO_2 are loosely bound to the surface of the SiO_2 such that the graphene only partially conforms to the substrate. After high temperature vacuum anneals, it is possible that the graphene more closely conforms to the SiO_2 surface giving a low roughness because of lack of contaminants on both the graphene and SiO_2 *but* a low mobility because of its close coupling to the low mobility oxide.

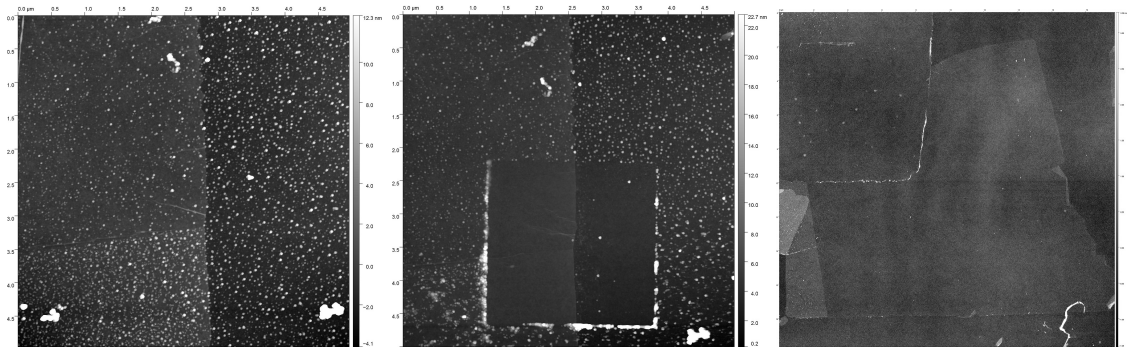

(a) acetone (b) AFM broom (c) vacuum

Figure B.7: AFM images of graphene flakes after an acetone soak, an AFM broom, and a 4-hour vacuum anneal. The broomed window shows obvious improvement comparable to the improvement shown after a long vacuum anneal.

Furthermore, Figure B.9 provides the surface roughness values for devices cleaned by vacuum and hydrogen anneals in comparison to acetone cleaning and AFM brooming. An important note about Figure B.9 is the tagged data point indicating a very high surface roughness (green circle) after a hydrogen anneal. After examining this device in AFM tapping mode, it was obvious that there was some PMMA residue left behind on the graphene that was not fully removed by hydrogen annealing. This device is shown in Figure B.10 before and after annealing and we believe that the reason this PMMA could not be removed was

a hardening process that occurred during RIE plasma etching for the Hall bar shape of the device. Indeed, there is often an optically green residue left behind on much of the wafer when an etching process has been completed. None of the anneal processes tried in this work were capable of removing this layer. Perhaps a longer, more aggressive anneal could remove this layer but subsequent vacuum anneals did not. On the other hand, AFM brooming seems to have fully removed the hardened PMMA on both this device and other test devices.

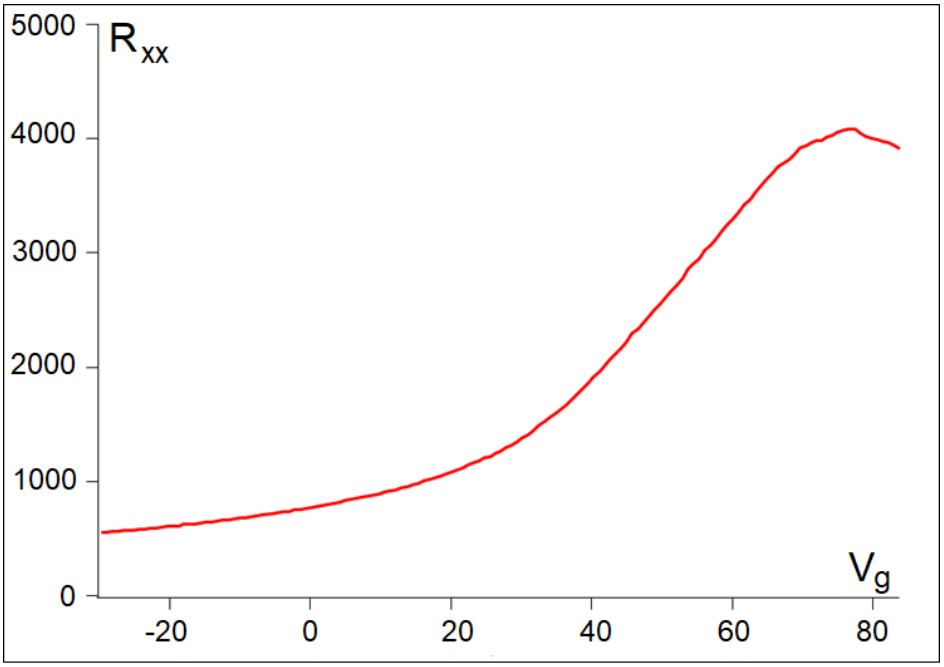

Figure B.8: The graphene resistance versus applied gate voltage of a vacuum anneal graphene device. Because of the broadness of the peak,we know that the mobility is low. In addition, the peak is located far from 0V which made it less useful for the osmium adatom project, in which hole doping moves the Dirac peak to the right.

In addition, hydrogen anneals also seems to cause degradation of the thin-film metal contact layer as shown in Figure B.11.

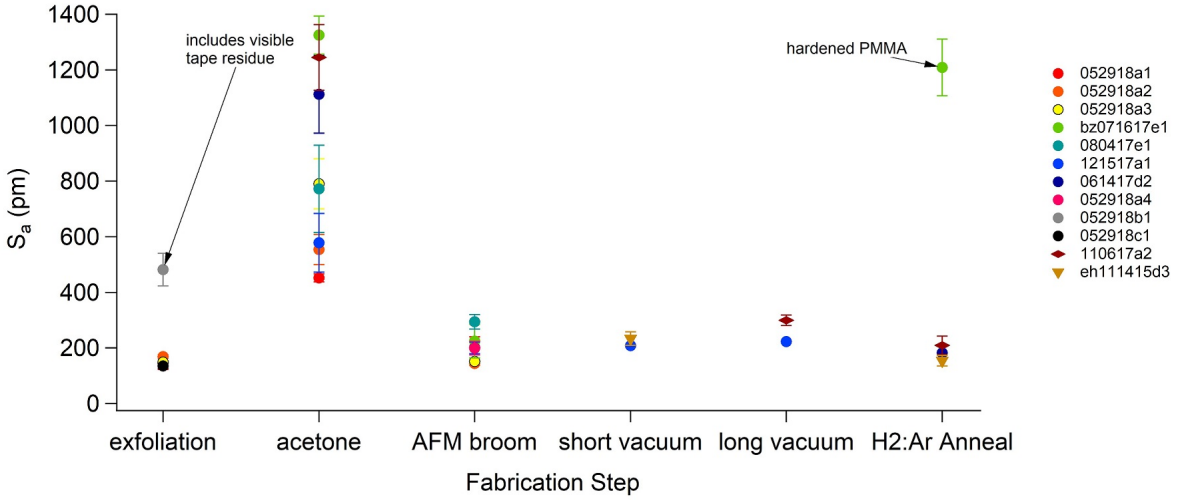

Figure B.9: The arithmetical surface roughness of graphene as-exfoliated, after an acetone soak to remove PMMA, after AFM brooming, and after anneals.

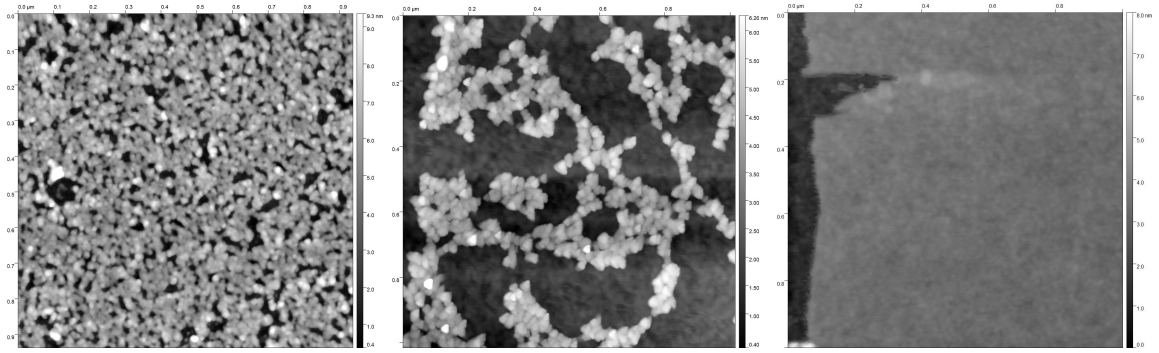

(a) after acetone (b) after anneal (c) after broom

Figure B.10: Under an optical microscope, a green layer of hardened PMMA is visible and this layer is not entirely removed by vacuum or hydrogen annealing. For this device, a hydrogen anneal was used but vacuum annealing was tested on other devices with similar results. AFM brooming easily removes this hardened PMMA layer.

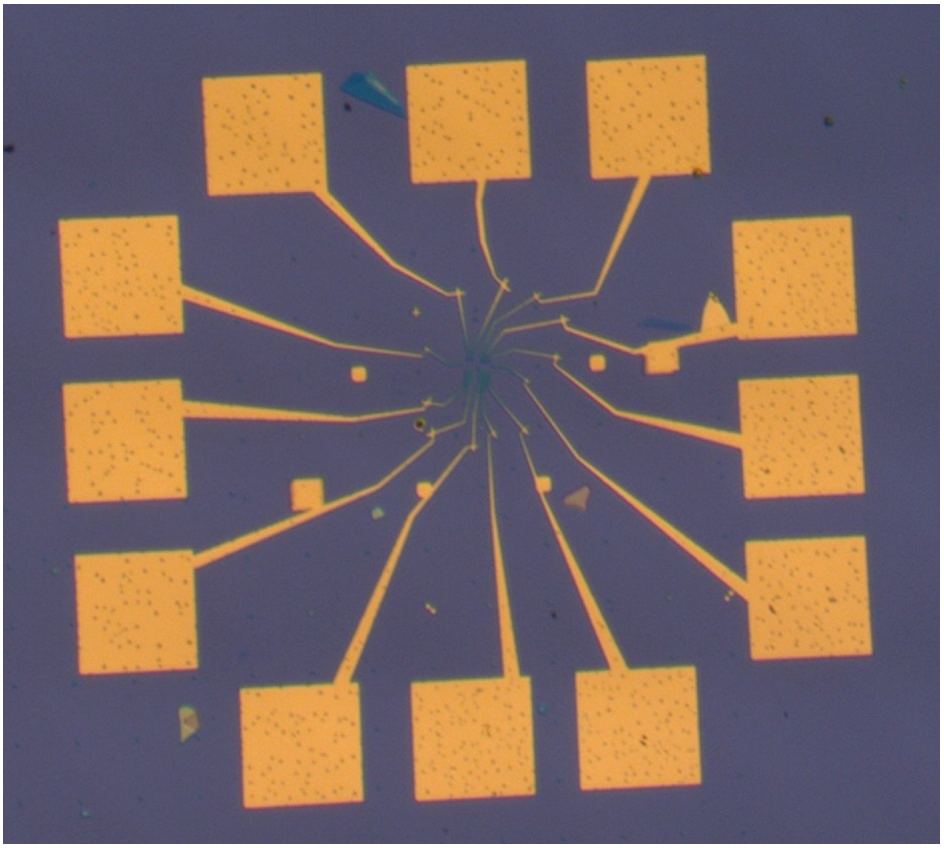

Figure B.11: The metal bond pads and wires attached to graphene are destroyed by hydrogen-argon and oxygen-argon anneals. Longer times at these temperatures causes the holes in the metal film to further degrade in a dendritic structure.

B.5 Conclusions

In conclusion, we have measured the surface roughness of graphene using AFM tapping mode images of high resolution to prove the efficiency of AFM brooming (also called AFM ironing) for cleaning the surface of graphene from polymer resist PMMA 495 and PMMA 950. In all devices measured, the surface roughness was significantly improved by AFM brooming. Indeed, in an optically *well-broomed* region, the surface roughness reverts to nearly the roughness of as-exfoliated graphene flakes.

In addition, we have found that vacuum and gas-aided anneal processes also reduce the surface roughness to nearly the roughness of as-exfoliated flakes and give optically clean samples. However, vacuum annealing negatively affects the mobility of graphene on SiO_2. This could be addressed by placing the graphene flakes on a substrate such as hexagonal boron nitride. In addition, neither vacuum annealing nor hydrogen annealing proved capable of easily removing hardened PMMA residue resultant of oxygen plasma etching. Furthermore, because these devices are open-faced graphene, oxygen annealing is not an option, because the oxygen quickly etches away the graphene. For these reasons, AFM brooming was the most efficient surface cleaning technique found for graphene on SiO_2.

Appendix C

Lithium adatoms on graphene

C.1 Introduction

Lithium adatoms on graphene are predicted to transform graphene into a superconducting state [96]. In conjunction with a collaborative project on lithium intercalation into zirconium telluride, lithium adatoms on graphene have been measured. Unfortunately, no evidence of superconducting states in the graphene were found.

C.2 Methods

For lithium adatoms, the graphene devices were fabricated as discussed in previous chapters and Appendix A. Graphene was exfoliated onto SiO_2 wafers, contacts were made by electron beam lithography and thermal evaporation, and etched into Hall bar shapes by reactive ion etching. Polymer resist from lithography was removed via acetone soak during liftoff and subsequent AFM brooming. Unfortunately, for the device measured, the AFM brooming done was not sufficient to result in a high mobility graphene device. Indeed, the initial mobility of the as-made graphene device was only about 5,000 cm^2/Vs.

For lithium, the methodology of adatom deposition is much like that of tungsten or osmium. Lithium is highly reactive with air (particularly oxygen) and thus must be appropriately handled. However, because lithium has a much lower melting temperature than osmium or tungsten, the lithium source material can be added to the tungsten wire sources without any plasma coating, growth, or evaporation procedures.

Instead, in a high purity argon glove box, a small piece of lithium source material is cut and contained in a custom-built crucible. The crucible is machined such that it resembles a flat-bottomed bowl with a slit extending the width of the bowl and placed on a hotplate at 200° C. The bowl will hold the melted lithium source material and the slit is aligned with the tungsten wire. The wire is then lowered into the lithium source repeatedly until a visible piece of lithium has adhered to the tungsten wire. Lithium is a material that does not lose its shape close to the melting point, so the cut source material may not appear to have changed from its regular solid form. However, after the crucible has been on the hot plate for several minutes, the lithium will be softened considerably and the wire will easily travel through it. For an adequate though rough comparison of this process, imagine cutting softened butter with an electrical wire held by tweezers while wearing oven mitts.

After the lithium source wires have been made, small pieces of colored tape are attached to both ends of the tungsten and they are loaded into small vials. These vials are tightly closed and enclosed in a secondary, also tightly closed, plastic container. This container is removed from the glove box and stored in a continuous-flow nitrogen box. Loading them into the adatom dipper thermal evaporator is the last step before closing and pumping out the dilution fridge. This involves placing the entire dipper, while hanging from its appropriate plate on the fridge, in a bath of argon. When closing the fridge, great care was taken to fill the still shield and magnet core with argon then flow more argon into the still shield while the remaining temperature shields were put in place. The argon flow was only removed near the last step when the entire chamber would soon be pumped out.

During the experiment, these wires were used in the same manner as the osmium-coated tungsten wires with the exception that the current necessary to cause lithium evaporation was much lower than the current used for osmium or tungsten adatoms.

C.3 Results

In Figure C.1, the measured transport after each lithium evaporation and stage warm-up is shown. Because the Dirac peak shifts to the left, lithium adatoms electron dope the graphene, donating an electron which leaves a charged lithium ion on the graphene surface. Furthermore, each of the lithium evaporations also decrease the mobility of graphene. Most stage warm-ups remove some of the lithium from the graphene, causing the Dirac peak to shift rightward again but even after two room temperature (RT) warm-ups, the initial device transport is not recovered. This indicates that not all of the lithium is removed from the graphene during the room temperature warm-ups.

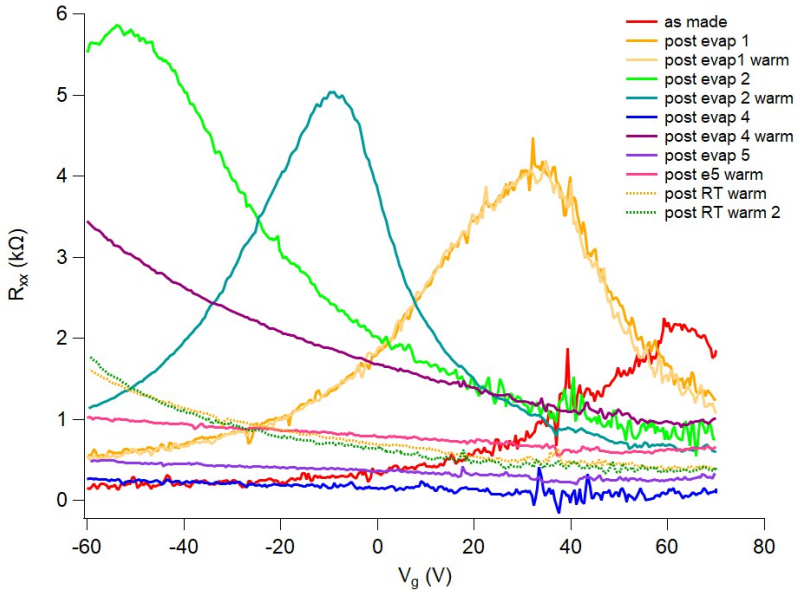

Figure C.1: Dirac peak evolution as lithium is added and the device is warmed.

We also studied the power law relationship of the change in the Dirac peak location to the change in the mobility. This is shown in Figure C.2 where the blue fit line (on a logarithmic plot) includes all of the data points and the red fit line is an approximate fit excluding the leftmost outlier. Based on the fit parameters given being less than 1, we do not believe that the lithium adatoms are clustering on the graphene. Indeed, if we use the red fit line, then the power law exponent b is consistent with point-like charged impurity scatterers. In addition, during most stage warm-ups, the Dirac peak shifts to the right which indicates either that the lithium is being removed from the surface or that it is falling into equilibrium positions. Finally, based on this change in the Dirac point gate voltage, we also calculated the deposition density of the lithium adatoms to be about 25×10^{12} cm^{-2}.

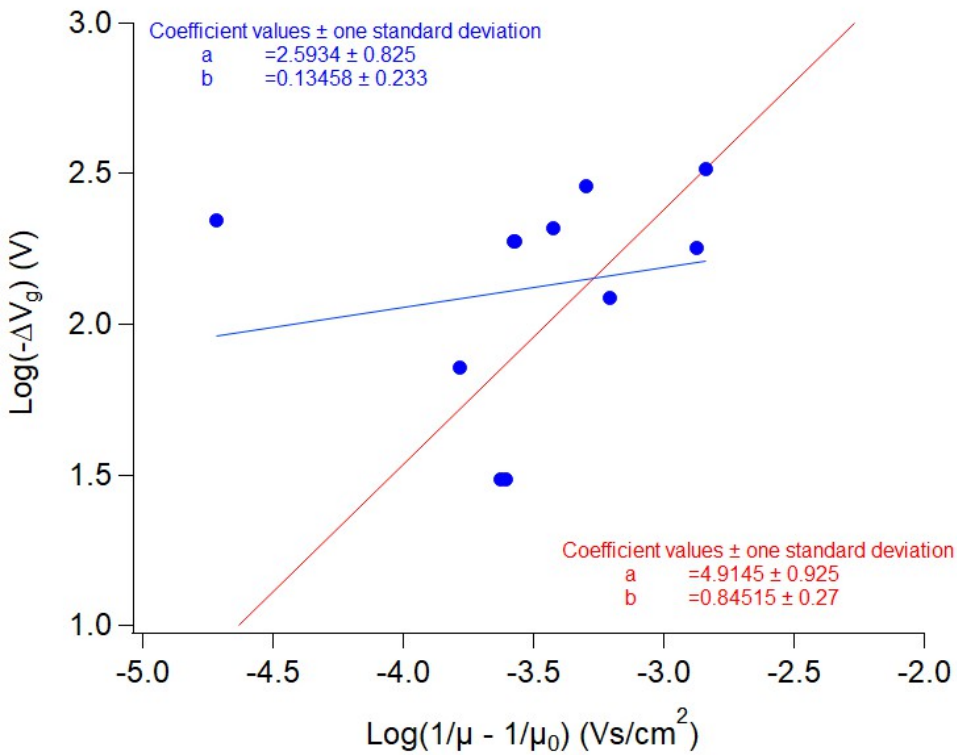

Figure C.2: The change in the Dirac point gate voltage and the change in the inverse mobility for two fitting equations.

C.4 Conclusions

The discussion of graphene undergoing a superconducting transition when decorated with lithium adatoms is an intriguing prediction. While we were unable to see such a transition in the preliminary reported data, there is much room for improvement in further investigations. In particular, this experiment should be extended below 4 K since the superconducting transition for graphene with lithium adatoms as occurs around 1 K. In addition, graphene with a higher initial mobility may be less affected by the initial scattering distribution and thus more affected by proximity to adatoms such as lithium.

Bibliography

[1] P. R. Wallace. "The Band Theory of Graphite". In: *Physical Review* 71 (9 May 1947), pp. 622–634. DOI: 10.1103/PhysRev.71.622. URL: https://link.aps.org/doi/10.1103/PhysRev.71.622.

[2] K. S. Novoselov et al. "Two-dimensional atomic crystals". In: *Proceedings of the National Academy of Sciences* 102.30 (2005), pp. 10451–10453. ISSN: 0027-8424. DOI: 10.1073/pnas.0502848102. eprint: https://www.pnas.org/content/102/30/10451.full.pdf. URL: https://www.pnas.org/content/102/30/10451.

[3] R. Peierls. "Quelques propriétés typiques des corps solides". fre. In: *Annales de l'institut Henri Poincaré* 5.3 (1935), pp. 177–222. URL: http://eudml.org/doc/78996.

[4] L. D. Landau. "Zur Theorie der phasenumwandlungen II". In: *Physikalische Zeitschrift der Sowjetunion* 11 (1937), pp. 26–35.

[5] Jung-Suk Sung and Kim HJ Sung YK. "Emerging Analysis on the Preparation and Application of Graphene by Bibliometry". In: *Journal of Material Science and Engineering* 04 (Jan. 2015). DOI: 10.4172/2169-0022.1000192.

[6] A. J. Frenzel et al. "Semiconducting-to-Metallic Photoconductivity Crossover and Temperature-Dependent Drude Weight in Graphene". In: *Physical Review Letters* 113 (5 July 2014), p. 056602. DOI: 10.1103/PhysRevLett.113.056602. URL: https://link.aps.org/doi/10.1103/PhysRevLett.113.056602.

[7] J-H Chen et al. "Charged-impurity scattering in graphene". In: *Nature Physics* 4.5 (2008), pp. 377–381.

[8] Tsuneya Ando. "Screening Effect and Impurity Scattering in Monolayer Graphene". In: *Journal of the Physical Society of Japan* 75.7 (July 2006), p. 074716.

[9] J. Martin et al. "Observation of electronâ€"hole puddles in graphene using a scanning single-electron transistor". In: *Nature Physics* 4 (Nov. 2007), p. 144. URL: https://doi.org/10.1038/nphys781.

[10] Yuanbo Zhang et al. "Origin of spatial charge inhomogeneity in graphene". In: *Nature Physics* 5 (Aug. 2009), p. 722. URL: https://doi.org/10.1038/nphys1365.

[11] Michael Fuhrer. "Charge transport and inhomogeneity near the minimum conductivity point in graphene". In: *Phys. Rev. B* 77 (Feb. 2008). DOI: 10.1103/PhysRevB.77.081402.

[12] Maxim Trushin et al. "Finite conductivity minimum in bilayer graphene without charge inhomogeneities". In: *Phys. Rev. B* 82 (15 Oct. 2010), p. 155308. DOI: 10.1103/PhysRevB.82.155308. URL: https://link.aps.org/doi/10.1103/PhysRevB.82.155308.

[13] Yow-Jon Lin and Jian-Jhou Zeng. "Tuning the work function of graphene by ultraviolet irradiation". In: *Applied Physics Letters* 102.18 (2013), p. 183120. DOI: 10.1063/1.4804289. eprint: https://doi.org/10.1063/1.4804289. URL: https://doi.org/10.1063/1.4804289.

[14] Mark B. Lundeberg et al. "Tuning quantum nonlocal effects in graphene plasmonics". In: *Science* 357.6347 (2017), pp. 187–191. ISSN: 0036-8075. DOI: 10.1126/science.aan2735. URL: http://science.sciencemag.org/content/357/6347/187.

[15] Matthew Yankowitz et al. "Dynamic band-structure tuning of graphene moiré superlattices with pressure". In: *Nature* 557.7705 (May 2018), pp. 404–408. ISSN: 1476-4687. DOI: 10.1038/s41586-018-0107-1. URL: https://doi.org/10.1038/s41586-018-0107-1.

[16] Zhenzhao Jia et al. "Transport study of graphene adsorbed with indium adatoms". In: *Physical Review B* 91.8 (Feb. 2015), p. 085411.

[17] U Chandni, Erik A Henriksen, and J P Eisenstein. "Transport in indium-decorated graphene". In: *Physical Review B* 91.24 (June 2015), p. 245402.

[18] Jyoti Katoch and Masa Ishigami. "Impact of calcium on transport property of graphene". In: *Solid State Communications* 152.2 (2012), pp. 60–63. ISSN: 0038-1098. DOI: https://doi.org/10.1016/j.ssc.2011.11.003. URL: http://www.sciencedirect.com/science/article/pii/S0038109811005990.

[19] S. Woo et al. "Temperature-dependent transport properties of graphene decorated by alkali metal adatoms (Li, K)". In: *Applied Physics Letters* 111.26 (2017), p. 263502. DOI: 10.1063/1.5001080. eprint: https://doi.org/10.1063/1.5001080. URL: https://doi.org/10.1063/1.5001080.

[20] Ali Khademi et al. "Alkali doping of graphene: The crucial role of high-temperature annealing". In: *Physical Review B* 94.20 (2016), p. 201405.

[21] K Pi et al. "Electronic doping and scattering by transition metals on graphene". In: *Physical Review B* 80.7 (Aug. 2009), p. 075406.

[22] Yilin Wang et al. "Electronic transport properties of Ir-decorated graphene". In: *Scientific Reports* 5 (Oct. 2015), p. 15764.

[23] Jun Yan and Michael S Fuhrer. "Correlated charged impurity scattering in graphene". In: *Physical Review Letters* 107.20 (2011), p. 206601.

[24] K M McCreary et al. "Effect of cluster formation on graphene mobility". In: *Physical Review B* 81.11 (Mar. 2010), p. 115453.

[25] Yilin Wang et al. "Neutral-current Hall effects in disordered graphene". In: *Physical Review B* 92 (16 Oct. 2015), p. 161411. DOI: 10.1103/PhysRevB.92.161411. URL: https://link.aps.org/doi/10.1103/PhysRevB.92.161411.

[26] Jayakumar Balakrishnan et al. "Giant spin Hall effect in graphene grown by chemical vapour deposition". In: *Nature Communications* 5 (Aug. 2014), pp. 1–7.

[27] A. Avsar et al. "Spin–orbit proximity effect in graphene". In: *Nature Communications* 5 (Sept. 2014), p. 4875. URL: https://doi.org/10.1038/ncomms5875.

[28] Zhe Wang et al. "Strong interface-induced spin–orbit interaction in graphene on WS2". In: *Nature Communications* 6 (Sept. 2015), p. 8339. URL: https://doi.org/10.1038/ncomms9339.

[29] Bowen Yang et al. "Tunable spin–orbit coupling and symmetry-protected edge states in graphene/WS2". In: *2D Materials* 3.3 (Sept. 2016), p. 031012. DOI: 10.1088/2053-1583/3/3/031012.

[30] T. Wakamura et al. "Strong Anisotropic Spin-Orbit Interaction Induced in Graphene by Monolayer WS_2". In: *Physical Review Letters* 120 (10 Mar. 2018), p. 106802. DOI: 10.1103/PhysRevLett.120.106802. URL: https://link.aps.org/doi/10.1103/PhysRevLett.120.106802.

[31] Bowen Yang et al. "Strong electron-hole symmetric Rashba spin-orbit coupling in graphene/monolayer transition metal dichalcogenide heterostructures". In: *Physical Review B* 96 (4 July 2017), p. 041409. DOI: 10.1103/PhysRevB.96.041409. URL: https://link.aps.org/doi/10.1103/PhysRevB.96.041409.

[32] Simon Zihlmann et al. "Large spin relaxation anisotropy and valley-Zeeman spin-orbit coupling in WSe 2/graphene/h-BN heterostructures". In: *Physical Review B* 97.7 (2018), p. 075434.

[33] JO Island et al. "Spin-orbit driven band inversion in bilayer graphene by van der Waals proximity effect". In: *arXiv preprint arXiv:1901.01332* (2019).

[34] Martin Gmitra and Jaroslav Fabian. "Graphene on transition-metal dichalcogenides: A platform for proximity spin-orbit physics and optospintronics". In: *Physical Review B* 92 (15 Oct. 2015), p. 155403. DOI: 10.1103/PhysRevB.92.155403. URL: https://link.aps.org/doi/10.1103/PhysRevB.92.155403.

[35] Zhe Wang et al. "Origin and Magnitude of 'Designer' Spin-Orbit Interaction in Graphene on Semiconducting Transition Metal Dichalcogenides". In: *Physical Review X* 6 (4 Oct. 2016), p. 041020. DOI: 10.1103/PhysRevX.6.041020. URL: https://link.aps.org/doi/10.1103/PhysRevX.6.041020.

[36] Gina Peschel. *Carbon-Carbon bonds: Hybridization*. English. May 2011. URL: https://www.physik.fu-berlin.de/einrichtungen/ag/ag-reich/lehre/Archiv/ss2011/docs/Gina_Peschel-Handout.pdf.

[37] Samuel David Littlejohn. *Electrical Properties of Graphite Nanoparticles in Silicone: Flexible Oscillators and Electromechanical Sensing*. English. 1st ed. Springer International Publishing, 2014. ISBN: 978-3-319-00740-3.

[38] Anthony J Leggett and Bill Coish. *Lecture 5: Graphene: Electronic band structure and Dirac fermions*. English. Lecture. 2010. URL: https://uwaterloo.ca/institute-for-quantum-computing/sites/ca.institute-for-quantum-computing/files/uploads/files/lecture-5.pdf.

[39] C. Kittel. *Introduction to Solid State Physics*. 7th ed. Wiley, 2004. ISBN: 978-0-471-41526-8.

[40] A. H. Castro Neto et al. "The electronic properties of graphene". In: *Reviews of Modern Physics* 81 (1 Jan. 2009), pp. 109–162. DOI: 10.1103/RevModPhys.81.109. URL: https://link.aps.org/doi/10.1103/RevModPhys.81.109.

[41] Dodd Joseph Gray, Adam Nykoruk McCaughan, and Bhaskar Mookerji. "Crystal Structure of Graphite, Graphene and Silicon". In: 2009.

[42] Ali Khademi. "Tuning Graphene's Electronic and Transport Properties via Adatom Deposition". English. PhD thesis. Vancouver: The University of British Columbia, Aug. 2017. URL: https://open.library.ubc.ca/cIRcle/collections/ubctheses/24/items/1.0354245.

[43] Jean-Noel Fuchs and Mark Oliver Goerbig. *Introduction to the Physical Properties of Graphene: Lecture Notes*. 2008. URL: http://web.physics.ucsb.edu/~phys123B/w2015/pdf_CoursGraphene2008.pdf.

[44] S. Reich et al. "Tight-binding description of graphene". In: *Physical Review B* 66 (3 July 2002), p. 035412. DOI: 10.1103/PhysRevB.66.035412. URL: https://link.aps.org/doi/10.1103/PhysRevB.66.035412.

[45] R. S. Deacon et al. "Cyclotron resonance study of the electron and hole velocity in graphene monolayers". In: *Physical Review B* 76 (8 Aug. 2007), p. 081406. DOI: 10.1103/PhysRevB.76.081406. URL: https://link.aps.org/doi/10.1103/PhysRevB.76.081406.

[46] Peter T. Gallagher. *Lectures 7-8: Fine and hyperfine structure*. English. Trinity College Dublin. URL: https://www.tcd.ie/Physics/people/Peter.Gallagher/lectures/js_atomic/.

[47] C. L. Kane and E. J. Mele. "Z_2 Topological Order and the Quantum Spin Hall Effect". In: *Physical Review Letters* 95.14 (Oct. 2005), p. 146802. URL: http://link.aps.org/doi/10.1103/PhysRevLett.95.146802.

[48] C. L. Kane and E. J. Mele. "Quantum Spin Hall Effect in Graphene". In: *Physical Review Letters* 95.22 (Nov. 2005), p. 226801. URL: http://link.aps.org/doi/10.1103/PhysRevLett.95.226801.

[49] M. Büttiker. "Absence of backscattering in the quantum Hall effect in multiprobe conductors". In: *Physical Review B* 38 (14 Nov. 1988), pp. 9375–9389. DOI: 10.1103/PhysRevB.38.9375. URL: https://link.aps.org/doi/10.1103/PhysRevB.38.9375.

[50] Conan Weeks et al. "Engineering a Robust Quantum Spin Hall State in Graphene via Adatom Deposition". In: *Physical Review X* 1 (Apr. 2011). DOI: 10.1103/PhysRevX.1.021001.

[51] Jun Hu et al. "Giant Topological Insulator Gap in Graphene with $5d$ Adatoms". In: *Physical Review Letters* 109.26 (Dec. 2012), p. 266801. URL: https://link.aps.org/doi/10.1103/PhysRevLett.109.266801.

[52] Hongbin Zhang et al. "Electrically Tunable Quantum Anomalous Hall Effect in Graphene Decorated by 5*d* Transition-Metal Adatoms". In: *Physical Review Letters* 108 (5 Feb. 2012), p. 056802. DOI: 10.1103/PhysRevLett.108.056802. URL: https://link.aps.org/doi/10.1103/PhysRevLett.108.056802.

[53] Tobias Frank et al. "Copper adatoms on graphene: Theory of orbital and spin-orbital effects". In: *Physical Review B* 95 (3 Jan. 2017), p. 035402. DOI: 10.1103/PhysRevB.95.035402. URL: https://link.aps.org/doi/10.1103/PhysRevB.95.035402.

[54] Yuliang Mao, Jianmei Yuan, and Jianxin Zhong. "Density functional calculation of transition metal adatom adsorption on graphene". In: *Journal of physics. Condensed matter : an Institute of Physics journal* 20 (Mar. 2008), p. 115209. DOI: 10.1088/0953-8984/20/11/115209.

[55] Jukka-Pekka Jalkanen et al. "A Computational Study of the Adsorption of Small Ag and Au Nanoclusters on Graphite". In: *The Journal of Physical Chemistry A* 111.49 (Dec. 2007), pp. 12317–12326. ISSN: 1089-5639. DOI: 10.1021/jp074969m. URL: https://doi.org/10.1021/jp074969m.

[56] N.W. Ashcroft and N.D. Mermin. *Solid State Physics*. Philadelphia: Saunders College Publishing, 1976.

[57] Supriyo Datta. *Electronic Transport in Mesoscopic Systems*. Vol. 1st pbk. ed. (with corrections). Cambridge Studies in Semiconductor Physics and Microelectronic Engineering Vol. 3. Cambridge University Press, 1997. ISBN: 9780521416047. URL: http://libproxy.wustl.edu/login?url=http://search.ebscohost.com/login.aspx?direct=true&db=e000xna&AN=510988&site=ehost-live&scope=site.

[58] Klaus von Klitzing. "The quantized Hall effect". In: *Rev. Mod. Phys.* 58 (3 July 1986), pp. 519–531. DOI: 10.1103/RevModPhys.58.519. URL: https://link.aps.org/doi/10.1103/RevModPhys.58.519.

[59] Likai Li et al. "Quantum Hall effect in black phosphorus two-dimensional electron system". In: *Nature Nanotechnology* 11 (Mar. 2016), p. 593. URL: https://doi.org/10.1038/nnano.2016.42.

[60] Yuanbo Zhang et al. "Experimental observation of the quantum Hall effect and Berry's phase in graphene". In: *Nature* 438.7065 (Nov. 2005), pp. 201–204. ISSN: 0028-0836. DOI: 10.1038/nature04235. URL: http://dx.doi.org/10.1038/nature04235.

[61] Y. Zhang et al. "Landau-Level Splitting in Graphene in High Magnetic Fields". In: *Physical Review Letters* 96 (13 Apr. 2006), p. 136806. DOI: 10.1103/PhysRevLett.96.136806. URL: https://link.aps.org/doi/10.1103/PhysRevLett.96.136806.

[62] Daniel G.Flynn. *The Quantum Hall Effect in Graphene*. Oct. 2010. URL: http://www.physics.drexel.edu/~bob/TermPapers/Flynn_QuantumPaper.pdf.

[63] D. C. Tsui, H. L. Stormer, and A. C. Gossard. "Two-Dimensional Magnetotransport in the Extreme Quantum Limit". In: *Physical Review Letters* 48 (22 May 1982), pp. 1559–1562. DOI: 10.1103/PhysRevLett.48.1559. URL: https://link.aps.org/doi/10.1103/PhysRevLett.48.1559.

[64] R. B. Laughlin. "Anomalous Quantum Hall Effect: An Incompressible Quantum Fluid with Fractionally Charged Excitations". In: *Physical Review Letters* 50 (18 May 1983), pp. 1395–1398. DOI: 10.1103/PhysRevLett.50.1395. URL: https://link.aps.org/doi/10.1103/PhysRevLett.50.1395.

[65] De Broglie, Louis. "Recherches sur la théorie des Quanta". In: *Annales de Physique* 10.3 (1925), pp. 22–128. DOI: 10.1051/anphys/192510030022. URL: https://doi.org/10.1051/anphys/192510030022.

[66] Edward MacKinnon. "De Broglie's thesis: A critical retrospective". In: *American Journal of Physics* 44.11 (1976), pp. 1047–1055. DOI: 10.1119/1.10583. eprint: https://doi.org/10.1119/1.10583. URL: https://doi.org/10.1119/1.10583.

[67] Gerd Bergmann. "Weak localization in thin films: a time-of-flight experiment with conduction electrons". In: *Physics Reports* 107.1 (). ISSN: 0370-1573. DOI: 10.1016/0370-1573(84)90103-0. URL: http://www.sciencedirect.com/science/article/pii/0370157384901030.

[68] Michael Hilke et al. "Weak localization in graphene: theory, simulations, and experiments". In: *The Scientific World Journal* 2014 (June 2014). DOI: http://dx.doi.org/10.1155/2014/737296.

[69] E. McCann et al. "Weak-Localization Magnetoresistance and Valley Symmetry in Graphene". In: *Physical Review Letters* 97 (14 Oct. 2006), p. 146805. DOI: 10.1103/PhysRevLett.97.146805. URL: https://link.aps.org/doi/10.1103/PhysRevLett.97.146805.

[70] Vladimir I Fal'ko et al. "Weak localization in graphene". In: *Solid State Communications* 143.1-2 (2007), pp. 33–38.

[71] F. V. Tikhonenko et al. "Weak Localization in Graphene Flakes". In: *Physical Review Letters* 100 (5 Feb. 2008), p. 056802. DOI: 10.1103/PhysRevLett.100.056802. URL: https://link.aps.org/doi/10.1103/PhysRevLett.100.056802.

[72] Edward McCann and Vladimir I Fal'ko. "z->-z Symmetry of Spin-Orbit Coupling and Weak Localization in Graphene". In: *Physical Review Letters* 108.16 (Apr. 2012), p. 166606.

[73] C Jang et al. "Tuning the Effective Fine Structure Constant in Graphene: Opposing Effects of Dielectric Screening on Short- and Long-Range Potential Scattering". In: *Physical Review Letters* 101.14 (Oct. 2008), p. 146805.

[74] F Schedin et al. "Detection of individual gas molecules adsorbed on graphene". In: *Nature Materials* 6.9 (2007), pp. 652–655.

[75] Ruitao Lv et al. "Ultrasensitive gas detection of large-area boron-doped graphene". In: *Proceedings of the National Academy of Sciences* 112.47 (2015), pp. 14527–14532. URL: https://www.pnas.org/content/112/47/14527.

[76] Kwanpyo Kim et al. "Selective metal deposition at graphene line defects by atomic layer deposition". In: *Nature Communications* 5 (Sept. 2014), p. 4781. URL: https://doi.org/10.1038/ncomms5781.

[77] Rinaldo Raccichini et al. "The role of graphene for electrochemical energy storage". In: *Nature Materials* 14 (Dec. 2014), p. 271. URL: https://doi.org/10.1038/nmat4170.

[78] Zhong-Shuai Wu et al. "Graphene/metal oxide composite electrode materials for energy storage". In: *Nano Energy* 1.1 (2012), pp. 107–131. ISSN: 2211-2855. DOI: https://doi.org/10.1016/j.nanoen.2011.11.001. URL: http://www.sciencedirect.com/science/article/pii/S2211285511000176.

[79] Maher F. El-Kady and Richard B. Kaner. "Scalable fabrication of high-power graphene micro-supercapacitors for flexible and on-chip energy storage". In: *Nature Communications* 4 (Feb. 2013), p. 1475. URL: https://doi.org/10.1038/ncomms2446.

[80] Sheng Han et al. "Porous Graphene Materials for Advanced Electrochemical Energy Storage and Conversion Devices". In: *Advanced Materials* 26.6 (2014), pp. 849–864. DOI: 10.1002/adma.201303115. eprint: https://onlinelibrary.wiley.com/doi/pdf/10.1002/adma.201303115. URL: https://onlinelibrary.wiley.com/doi/abs/10.1002/adma.201303115.

[81] Dale A.C. Brownson, Dimitrios K. Kampouris, and Craig E. Banks. "An overview of graphene in energy production and storage applications". In: *Journal of Power Sources* 196.11 (2011), pp. 4873–4885. ISSN: 0378-7753. DOI: https://doi.org/10.1016/j.jpowsour.2011.02.022. URL: http://www.sciencedirect.com/science/article/pii/S0378775311003764.

[82] A H Castro Neto and Francisco Guinea. "Impurity-Induced Spin-Orbit Coupling in Graphene". In: *Physical Review Letters* 103.2 (July 2009), p. 026804.

[83] K H Ding, Z G Zhu, and Jamal Berakdar. "Charge and spin Hall effect in graphene with magnetic impurities". In: *Europhysics Letters* 88.5 (Dec. 2009), p. 58001.

[84] Zhenhua Qiao et al. "Quantum anomalous Hall effect in graphene from Rashba and exchange effects". In: *Physical Review B* 82.16 (Oct. 2010), p. 161414.

[85] Samir Abdelouahed et al. "Spin-split electronic states in graphene: Effects due to lattice deformation, Rashba effect, and adatoms by first principles". In: *Physical Review B* 82.12 (Sept. 2010), p. 125424.

[86] Jun Ding et al. "Engineering quantum anomalous/valley Hall states in graphene via metal-atom adsorption: An ab-initio study". In: *Physical Review B* 84.19 (Nov. 2011), p. 195444.

[87] Hua Jiang et al. "Stabilizing Topological Phases in Graphene via Random Adsorption". In: *Physical Review Letters* 109.11 (Sept. 2012), p. 116803.

[88] Oleksii Shevtsov et al. "Tunable thermopower in a graphene-based topological insulator". In: *Physical Review B* 85.24 (June 2012), p. 245441.

[89] Dongwei Ma, Zhongyao Li, and Zhongqin Yang. "Strong spin–orbit splitting in graphene with adsorbed Au atoms". In: *Carbon* 50.1 (Jan. 2012), pp. 297–305.

[90] Po-Hao Chang et al. "Giant Thermoelectric Effect in Graphene-Based Topological Insulators with Heavy Adatoms and Nanopores". In: *Nano Letters* 14.7 (July 2014), pp. 3779–3784.

[91] Jun Hu, Zhenyue Zhu, and Ruqian Wu. "Chern Half Metals: A New Class of Topological Materials to Realize the Quantum Anomalous Hall Effect". In: *Nano Letters* 15.3 (Mar. 2015), pp. 2074–2078.

[92] H Sevinçli et al. "Electronic and magnetic properties of 3d transition-metal atom adsorbed graphene and graphene nanoribbons". In: *Physical Review B* 77.19 (May 2008), p. 195434.

[93] T Eelbo et al. "Adatoms and Clusters of 3*d* Transition Metals on Graphene: Electronic and Magnetic Configurations". In: *Physical Review Letters* 110.13 (Mar. 2013), p. 136804.

[94] Maria Losurdo et al. "Demonstrating the Capability of the High-Performance Plasmonic Gallium–Graphene Couple". In: *ACS Nano* 8.3 (2014). PMID: 24575951, pp. 3031–3041. DOI: 10.1021/nn500472r. eprint: https://doi.org/10.1021/nn500472r. URL: https://doi.org/10.1021/nn500472r.

[95] Congwen Yi et al. "Evidence of Plasmonic Coupling in Gallium Nanoparticles/Graphene/SiC". In: *Small* 8.17 (2012), pp. 2721–2730. DOI: 10.1002/smll.201200694. eprint: https://onlinelibrary.wiley.com/doi/pdf/10.1002/smll.201200694. URL: https://onlinelibrary.wiley.com/doi/abs/10.1002/smll.201200694.

[96] Gianni Profeta, Matteo Calandra, and Francesco Mauri. "Phonon-mediated superconductivity in graphene by lithium deposition". In: *Nature Physics* 8.2 (Jan. 2012), pp. 131–134.

[97] B M Ludbrook et al. "Evidence for superconductivity in Li-decorated monolayer graphene". In: *Proceedings of the National Academy of Sciences* 112.38 (Sept. 2015), pp. 11795–11799.

[98] Dominik Szczęśniak and Radosław Szczęśniak. "Revisiting the nature of superconducting phase in lithium-decorated graphene". In: *arXiv preprint arXiv:1810.07980* (2018).

[99] Irving Langmuir. "The Vapor Pressure of Metallic Tungsten". In: *Physical Review* 2.5 (Nov. 1913), pp. 329–342.

[100] Morton B. Panish and Liane Reif. "Vaporization of Ruthenium and Osmium". In: *The Journal of Chemical Physics* 37.1 (1962), pp. 128–131. DOI: 10.1063/1.1732934. eprint: https://doi.org/10.1063/1.1732934. URL: https://doi.org/10.1063/1.1732934.

[101] Marcello Carlà. "Stefan–Boltzmann law for the tungsten filament of a light bulb: Revisiting the experiment". In: *American Journal of Physics* 81.7 (2013), p. 512.

[102] Kentaro Nomura and Allan H MacDonald. "Quantum Hall Ferromagnetism in Graphene". In: *Physical Review Letters* 96.25 (June 2006), p. 256602.

[103] Shaffique Adam et al. "A self-consistent theory for graphene transport". In: *Proceedings of the National Academy of Sciences* 104.47 (2007), pp. 18392–18397.

[104] K Nakada and A Ishii. "Migration of adatom adsorption on graphene using DFT calculation". In: *Solid State Communications* 151.1 (Jan. 2011), pp. 13–16.

[105] K Nakada and A Ishii. "DFT Calculation for Adatom Adsorption on Graphene". In: *Graphene Simulation*. Ed. by Jian Ru Gong. InTechOpen, Aug. 2011, pp. 1–20.

[106] Montserrat Manadé, Francesc Viñes, and Francesc Illas. "Transition metal adatoms on graphene: A systematic density functional study". In: *Carbon* 95.C (Dec. 2015), pp. 525–534.

[107] Tsuneya Ando, T Nakanishi, and R Saito. "Berry's phase and absence of back scattering in carbon nanotubes". In: *Journal of the Physical Society of Japan* 67.8 (1998), pp. 2857–2862.

[108] Sankar Das Sarma and F Stern. "Single-particle relaxation time versus scattering time in an impure electron gas". In: *Physical Review B* 32.12 (1985), pp. 8442–8444.

[109] E H Hwang and Sankar Das Sarma. "Single-particle relaxation time versus transport scattering time in a two-dimensional graphene layer". In: *Physical Review B* 77.19 (May 2008), p. 195412.

[110] X Hong, K Zou, and J Zhu. "Quantum scattering time and its implications on scattering sources in graphene". In: *Physical Review B* 80.24 (Dec. 2009), p. 241415.

[111] M I Katsnelson, Francisco Guinea, and A K Geim. "Scattering of electrons in graphene by clusters of impurities". In: *Physical Review B* 79.19 (May 2009), p. 195426.

[112] V P Gusynin and S G Sharapov. "Magnetic oscillations in planar systems with the Dirac-like spectrum of quasiparticle excitations. II. Transport properties". In: *Physical Review B* 71.12 (Mar. 2005), p. 125124.

[113] PT Coleridge. "Small-angle scattering in two-dimensional electron gases". In: *Physical Review B* 44.8 (1991), p. 3793.

[114] Hugo E Romero et al. "n-Type Behavior of Graphene Supported on Si/SiO_2 Substrates". In: *ACS Nano* 2.10 (Oct. 2008), pp. 2037–2044.

[115] Nuno J G Couto et al. "Random Strain Fluctuations as Dominant Disorder Source for High-Quality On-Substrate Graphene Devices". In: *Physical Review X* 4.4 (Oct. 2014), p. 041019.

[116] P A Lee and T V Ramakrishnan. "Disordered electronic systems". In: *Reviews of Modern Physics* 57.2 (1985), p. 287.

[117] Boris L Altshuler, Arkadi G Aronov, and D E Khmelnitsky. "Effects of electron-electron collisions with small energy transfers on quantum localisation". In: *Journal of Physics C: Solid State Physics* 15.36 (1982), p. 7367.

[118] Gerd Bergmann. "Influence of Spin-Orbit Coupling on Weak Localization". In: *Physical Review Letters* 48.1 (Apr. 1982), pp. 1046–1049.

[119] Martin Prutton, Mohamed M. El Gomati, and J.A.D. Matthew. *Scanning Auger Electron Microscopy*. John Wiley & Sons Ltd, 2006.

[120] Oxford Instruments NanoAnalysis. "An Introduction to Energy-Dispersive and Wavelength-Dispersive X-ray Microanalysis". In: *X-ray Microanalysis*. Microscopy and Analysis X-ray Supplement (July 2006), S5–S8. URL: https://microscopy-analysis.com/sites/default/files/magazine_pdfs/mag%5C%20705_2006_July_Oxford_1.pdf.

[121] Andrew Zangwill. *Physics at Surfaces*. Cambridge University Press, 1988.

[122] Yung-Chang Lin et al. "Clean Transfer of Graphene for Isolation and Suspension". In: *ACS Nano* 5.3 (Mar. 2011), pp. 2362–2368.

[123] Yung-Chang Lin et al. "Graphene Annealing: How Clean Can It Be?" In: *Nano Letters* 12.1 (Jan. 2012), pp. 414–419.

[124] P. A. Lee and A. Douglas Stone. "Universal Conductance Fluctuations in Metals". In: *Phys. Rev. Lett.* 55 (15 Oct. 1985), pp. 1622–1625. DOI: 10.1103/PhysRevLett.55.1622. URL: https://link.aps.org/doi/10.1103/PhysRevLett.55.1622.

[125] Paul McConville and Norman O Birge. "Weak localization, universal conductance fluctuations, and 1/f noise in Ag". In: *Physical Review B* 47.24 (1993), p. 16667.

[126] C. Flynn et al. "An Ultra-High Vacuum Probe Station for 2D Material Transport and in situ Functionalization". In: *APS Meeting Abstracts*. 2018, Y37.009.

[127] K. Hatsuda et al. "Evidence for a quantum spin Hall phase in graphene decorated with Bi2Te3 nanoparticles". In: *Science Advances* 4.11 (2018). DOI: 10.1126/sciadv.aau6915. eprint: http://advances.sciencemag.org/content/4/11/eaau6915.full.pdf. URL: http://advances.sciencemag.org/content/4/11/eaau6915.

[128] C. D. Porter and D. Stroud. "Clustering and magnetic anisotropy of Fe adatoms on graphene". In: *Physical Review B* 85 (23 June 2012), p. 235452. DOI: 10.1103/PhysRevB.85.235452. URL: https://link.aps.org/doi/10.1103/PhysRevB.85.235452.

[129] K. S. Novoselov et al. "Electric Field Effect in Atomically Thin Carbon Films". In: *Science* 306.5696 (2004), pp. 666–669. ISSN: 0036-8075. DOI: 10.1126/science.1102896. eprint: http://science.sciencemag.org/content/306/5696/666.full.pdf. URL: http://science.sciencemag.org/content/306/5696/666.

[130] Yuan Huang et al. "Reliable Exfoliation of Large-Area High-Quality Flakes of Graphene and Other Two-Dimensional Materials". In: *ACS Nano* 9.11 (Nov. 2015), pp. 10612–10620. ISSN: 1936-0851. DOI: 10.1021/acsnano.5b04258. URL: https://doi.org/10.1021/acsnano.5b04258.

[131] Dung Hoang Tien et al. "Characterization of Graphene-based FET Fabricated using a Shadow Mask". In: *Scientific Reports* 6 (May 2016), p. 25050. URL: https://doi.org/10.1038/srep25050.

[132] Mahmood Aliofkhazraei et al. *Graphene Science Handbook: Fabrication Methods*. May 2016.

[133] M Rooks et al. "Low stress development of poly (methylmethacrylate) for high aspect ratio structures". In: *Journal of Vacuum Science & Technology B: Microelectronics and Nanometer Structures* 20 (Nov. 2002). DOI: 10.1116/1.1524971.

[134] Zhen Hua Ni et al. "The effect of vacuum annealing on graphene". In: *Journal of Raman Spectroscopy* 41.5 (2010), pp. 479–483. DOI: 10.1002/jrs.2485. eprint:

https://onlinelibrary.wiley.com/doi/pdf/10.1002/jrs.2485. URL: https://onlinelibrary.wiley.com/doi/abs/10.1002/jrs.2485.

[135] Zengguang Cheng et al. "Toward Intrinsic Graphene Surfaces: A Systematic Study on Thermal Annealing and Wet-Chemical Treatment of SiO2-Supported Graphene Devices". In: *Nano Letters* 11.2 (2011). PMID: 21218829, pp. 767–771. DOI: 10.1021/nl103977d. eprint: https://doi.org/10.1021/nl103977d. URL: https://doi.org/10.1021/nl103977d.

[136] A. Pirkle et al. "The effect of chemical residues on the physical and electrical properties of chemical vapor deposited graphene transferred to SiO2". In: *Applied Physics Letters* 99.12 (2011), p. 122108. DOI: 10.1063/1.3643444. eprint: https://doi.org/10.1063/1.3643444. URL: https://doi.org/10.1063/1.3643444.

[137] Kitu Kumar, Youn-Su Kim, and Eui-Hyeok Yang. "The influence of thermal annealing to remove polymeric residue on the electronic doping and morphological characteristics of graphene". In: *Carbon* 65 (2013), pp. 35–45. ISSN: 0008-6223. DOI: https://doi.org/10.1016/j.carbon.2013.07.088. URL: http://www.sciencedirect.com/science/article/pii/S0008622313007227.

[138] Yingying Wang et al. "Surface enhanced Raman scattering of aged graphene: Effects of annealing in vacuum". In: *Applied Physics Letters* 99.23 (2011), p. 233103. DOI: 10.1063/1.3665624. eprint: https://doi.org/10.1063/1.3665624. URL: https://doi.org/10.1063/1.3665624.

[139] Jinpyo Hong et al. "Origin of New Broad Raman D and G Peaks in Annealed Graphene". In: *Scientific Reports* 3 (Sept. 2013), p. 2700. URL: https://doi.org/10.1038/srep02700.

[140] Wei Sun Leong, Chang Tai Nai, and John T. L. Thong. "What Does Annealing Do to Metalâ€"Graphene Contacts?" In: *Nano Letters* 14.7 (2014). PMID: 24912079, pp. 3840–3847. DOI: 10.1021/nl500999r. eprint: https://doi.org/10.1021/nl500999r. URL: https://doi.org/10.1021/nl500999r.

[141] Chan Wook Jang et al. "Rapid-thermal-annealing surface treatment for restoring the intrinsic properties of graphene field-effect transistors". In: *Nanotechnology* 24.40 (Sept. 2013), p. 405301. DOI: 10.1088/0957-4484/24/40/405301. URL: https://doi.org/10.1088%5C%2F0957-4484%5C%2F24%5C%2F40%5C%2F405301.

[142] J. Moser, A. Barreiro, and A. Bachtold. "Current-induced cleaning of graphene". In: *Applied Physics Letters* 91.16 (2007), p. 163513. DOI: 10.1063/1.2789673. eprint: https://doi.org/10.1063/1.2789673. URL: https://doi.org/10.1063/1.2789673.

[143] S. Hertel et al. "Current annealing and electrical breakdown of epitaxial graphene". In: *Applied Physics Letters* 98.21 (2011), p. 212109. DOI: 10.1063/1.3592841. eprint: https://doi.org/10.1063/1.3592841. URL: https://doi.org/10.1063/1.3592841.

[144] Harihara Ramamoorthy and Ratchanok Somphonsane. "In-situ current annealing of graphene-metal contacts". In: *Journal of Physics: Conference Series* 1144 (Dec. 2018), p. 012186. DOI: 10.1088/1742-6596/1144/1/012186. URL: https://doi.org/10.1088%5C%2F1742-6596%5C%2F1144%5C%2F1%5C%2F012186.

[145] T. Yu et al. "Bilayer Graphene System: Current-Induced Reliability Limit". In: *IEEE Electron Device Letters* 31.10 (Oct. 2010), pp. 1155–1157. ISSN: 0741-3106. DOI: 10.1109/LED.2010.2058994.

[146] A. M. Goossens et al. "Mechanical cleaning of graphene". In: *Applied Physics Letters* 100.7 (2012), p. 073110. DOI: 10.1063/1.3685504. eprint: https://doi.org/10.1063/1.3685504. URL: https://doi.org/10.1063/1.3685504.

[147] Jun Yong Khoo. "Introducing Spin-Orbit Interaction in Graphene". English. PhD thesis. Massachusetts Institute of Technology, Aug. 2018. URL: file:///C:/Users/abnormalalien/Downloads/1079895546-MIT.pdf.

[148] Jose Martinez-Castro et al. "Scanning Tunneling Microscopy of an Air Sensitive Dichalcogenide Through an Encapsulating Layer". In: *Nano Letters* 18.11 (). ISSN: 1530-6984. DOI: 10.1021/acs.nanolett.8b01978. URL: https://doi.org/10.1021/acs.nanolett.8b01978.

[149] Niclas Lindvall, Alexey Kalabukhov, and August Yurgens. "Cleaning graphene using atomic force microscope". In: *Journal of Applied Physics* 111.6 (2012), p. 064904. DOI: 10.1063/1.3695451. eprint: https://doi.org/10.1063/1.3695451. URL: https://doi.org/10.1063/1.3695451.

[150] Woosuk Choi et al. "Influence of removing PMMA residues on surface of CVD graphene using a contact-mode atomic force microscope". In: *RSC Advances* 7.12 (2017), pp. 6943–6949. DOI: 10.1039/C6RA27436F. URL: http://dx.doi.org/10.1039/C6RA27436F.